



Politecnico
di Torino

ScuDo

Scuola di Dottorato ~ Doctoral School
WHAT YOU ARE, TAKES YOU FAR

Doctoral Dissertation

Doctoral Program in Civil and Environmental Engineering (*XXXIVth* cycle)

Hydrodynamic Techniques for Fouling Control in Membrane Systems

By

Roberto Bert

Supervisor(s):

Prof. Costantino Manes, Supervisor
Prof. Alberto Tiraferri, Co-Supervisor

Doctoral Examination Committee:

Prof. Fulvio Boano, Politecnico di Torino, Italy
Prof. Luca Fortunato, Refree, King Abdullah University of Science and Technol-
ogy, Saudi Arabia
Prof. Andrea Marion, Refree, Università degli studi di Padova, Italy
Prof. Maurizio Righetti, Libera Univeristà di Bolzano, Italy
Prof. Tiziana Tosco, Politecnico di Torino, Italy

Politecnico di Torino

2022

Declaration

I hereby declare that, the contents and organization of this dissertation constitute my own original work and does not compromise in any way the rights of third parties, including those relating to the security of personal data.

Roberto Bert
2022

* This dissertation is presented in partial fulfillment of the requirements for **Ph.D. degree** in the Graduate School of Politecnico di Torino (ScuDo).

To my lovely grandmother who used to say:

- Roberto studia!

And to that irresponsible child who can now say:

-Tranquilla nonna so gestirmi.

Acknowledgements

21/09/2022

Il primo doveroso e sentito ringraziamento va al Proff. Costantino Manes. Tutor sin dalla tesi magistrale ha creduto in me spronandomi nell'intraprendere una delle più belle ed importanti esperienze della mia vita, guidandomi in questo percorso di ricerca e crescita con dedizione. Il tuo essere professore e amico e la tua sensibilità e presenza nel farmi da guida hanno rivelato una persona gentile capace di esprimere oltre le tue qualità professionali un affetto e un supporto di cui ti sarò sempre grato. Un sentito ringraziamento va anche al Proff. Alberto Tirafferri, co-tutor capace di affiancarmi in ogni momento con competenza, presenza e partecipazione, al Proff. Davide Poggi per le sue consulenze e il suo essere per me persona importante e al direttore il Proff. Francesco Laio, in rappresentanza del mio affetto e della mia riconoscenza verso tutto il dipartimento che in questi anni insieme è stato per me casa e rifugio, un posto che mi porterò sempre nel cuore.

Uno speciale ringraziamento va ai miei amici ancor più che colleghi con cui ho condiviso parte di questi anni e con i quali ho costruito rapporti indelebili. Al fantastico BAD 3 di Carla, Edo, Silvia, Roberto e Roberta, luogo di sorrisi, quotidianità, risate, parole, casino e felicità. A Cate, Gigi, Carla, Benny, Zac, Franca, Marta e Matti, l'ineguagliabile gruppo del "minchia quanto disagio... non ce ne' uno dritto... se non facessimo gruppo saremmo già tutti morti" con i quali si condivide molto di più di birruzze e di un semplice affetto. Ognuno di voi, a suo modo, ha contribuito a rendere questi anni indimenticabili, pieni di amore e gioia, mostrandomi un affetto smisurato ed una presenza costante, condividendo difficoltà, risate tempo ed emozioni, suscitando delle sensazioni ed un calore che

mi porterò sempre dentro. I ricordi condivisi con voi e la vostra amicizia sono i più bei regali di questo percorso.

A Cosimo che mi ha spronato ad iniziare, a Beppe che mi ha fatto dono della sua esperienza, a Cagni per l'aiuto e soprattutto a Roberto per essere stato il miglior compagno di avventura che potessi desiderare nell'essere la persona più gentile e brillante che conosco. Al Vecio Davide, al giovane Elia e al buon Piteruzzo ai quali mi sono affezionato molto nello scoprire persone affini, interessanti e divertenti, ai colleghi del 34° ciclo Elisa, Luca, Benedetta, Matteo, Melissa, Hamed ed Ahmed con i quali si sono condivise difficoltà e aiuto, e a tutti quelli che anche se non menzionati sono stati parte di questo magico viaggio nella speranza che ognuno di voi continui a far parte di me.

Un ringraziamento a TUTTI gli amici di una Vita con particolare attenzione a Eli, Percy, Paul, Max, Gabry, Nicu e Miky che sin dagli albori della nostra conoscenza continuano ad accompagnarmi con costanza, particolare affetto e presenza. Il vostro essere capaci di starmi vicino in ogni momento di felicità e spensieratezza e soprattutto nei momenti difficili, i viaggi e le esperienze condivise, le risate e ricordi costruiti insieme sono i doni preziosi che mi porterò sempre nel cuore e per i quali non vi ringrazierò mai abbastanza.

Ringrazio sentitamente il mio fratellino Dario e il mio Cugi per essere parte della famiglia ed amici sinceri, persone fondamentali e grandi punti di riferimento sui quali poter contare. Un ringraziamento va a Lolla per aver portato serenità ed equilibrio e per essere stata compagna per gran parte di questo percorso e soprattutto a Gloria per essere diventata in così poco tempo la persona per me insostituibile e più importante. Con la tua sensibilità, la tua dolcezza, le tue attenzioni, il tuo amore, il tuo sostegno e il tuo essere persona meravigliosa hai saputo starmi vicino ogni giorno nel periodo più complesso di questo percorso portando all'interno della mia vita felicità, emozioni inaspettate e tanto amore. Nel ringraziarti per essere il mio presente e il mio punto fisso, la mia scelta consapevole e il mio sorriso mi auguro che impegno e rispetto siano le basi che ci consentano

di accrescere il nostro legame continuando a costruire insieme un futuro felice ed una famiglia, coltivando con pazienza e attenzione questo nostro amore.

Infine ringrazio calorosamente tutta la mia famiglia che negli anni mi ha sempre sostenuto nel mio percorso di crescita professionale e soprattutto personale, insegnandomi il valore delle cose e trasmettendomi i principi di correttezza e onestà. A Mamma, persona riservata e forte che con la sua rigosità e dolcezza mi ha reso una persona più diligente e attenta, a Papà che con la sua simpatia e giocosità ha contribuito a modellare il mio carattere solare e a Nonna che con la sua saggezza e semplicità resta per me uno dei più grandi esempi. Il sorriso che mi contraddistingue ed i traguardi raggiunti hanno molto di voi.

Roby

Abstract

Fouling due to particle deposition either on the membrane surface or within the porous structure is the most adverse phenomenon in membrane-based separation systems. It causes an increase in both the hydraulic resistance and osmotic pressure at the feed-membrane interface leading to flux and selectivity reduction over time. Since this phenomenon is unavoidable, control approaches that minimise process complexity and operational costs are required to mitigate its effects. To this end, pulsed-hydrodynamics methods have proved to be cost-effective and easily implementable solutions that can improve the membrane's performance and durability. However, to fully understand and hence appropriately exploit such effects, it is necessary to understand the underpinning flow processes. Towards this end, in this work, we propose and validate a new module-scale laboratory facility to investigate, at very well-controlled flow conditions, both steady and pulsating flow behaviours.

A series of filtration experiments and flow measurements through laser diagnostic techniques (Particle Image Velocimetry (PIV) and Laser Doppler Anemometry(LDA)) were performed under flow-dynamics conditions typically encountered in membrane processes to shed light on the following aspects: (1) assess the effects of permeate flux (i.e. in fluid dynamics jargon "wall suction") on the velocity statistics and turbulent structure of turbulent (low Reynolds number) channel flows; (2) explore the extent to which pulsating flows can mitigate fouling over a range of wave amplitudes and frequencies of the pulsation; (3) explain the effects related to fouling mitigation and enhancement of permeate flux using non-dimensional quantities to provide results of general validity.

As far as point 1 is concerned, results indicate that one-point velocity statistics in channel flows with suction collapse very well when scaled with the maximum velocity and channel half height. The comparison of the main velocity statistics for the benchmark smooth-wall condition and those obtained for different wall-suction flows indicate that suction tends to suppress turbulence independently of the suction rate. Such a suppression is consistent with an observed reduction in turbulent kinetic energy production while dissipation remain unaltered by suction. Interestingly (but strangely), despite this turbulence suppression, wall suction imposed rather weak variations in the turbulence structure as detected by means of quadrant analysis and two-point cross-correlation functions.

With regards to point 2 and 3, it was observed that the amplitude of the imposed wave has little effect on fouling mitigation, whereas frequency significantly controls both the increase in permeate and, consequently, in clogging reduction. It was speculated that this behaviour is controlled by a non-dimensional formulation of the pulsating frequency, which, according to the relevant literature, corresponds to conditions whereby the turbulence induced by the enhanced shear of the high-velocity phase of the pulsation, has the time to develop and propagate throughout the channel height. It is herein hypothesized that such enhanced turbulence helps particles escape from the near-wall flow region where they would be otherwise trapped or attracted by the suction flow.

Contents

List of Figures	xii
List of Tables	xxi
Nomenclature	xxiii
1 Introduction	1
1.1 Problems related to membrane fouling	2
1.2 Aims and objectives	4
1.3 Thesis contents	5
2 New Facility for Membrane Fouling Investigations under Customizable Hydrodynamics: Validation and Preliminary Experiments with Pulsating Cross-Flow	6
2.1 Abstract	7
2.2 Introduction	8
2.3 Experimental Methods	10
2.3.1 Overall Description of the Facility	10
2.3.2 Description of the Test Section	12
2.3.3 Description of the Flow-Conditioning Unit and Pulsating Flow System	14

2.4	Experimental Procedure and Measuring Equipment	17
2.4.1	Fluid Dynamic Tests	17
2.4.2	Filtration Tests	19
2.5	Results	21
2.5.1	Fluid Dynamic Tests	21
2.5.2	Filtration Tests	23
2.6	Concluding Remarks	29
References		30
3	Suction effects on turbulence in channel flows at low Reynolds numbers	34
3.1	Abstract	35
3.2	Introduction	36
3.3	Experimental Methods	40
3.4	Experimental Procedure and Measuring Equipment	44
3.4.1	PIV Measurements	44
3.4.2	LDA Measurements	45
3.4.3	Data validation	47
3.4.4	Assessment of non-uniformity in the filtration tests . . .	52
3.5	Results	54
3.5.1	One-point statistics	54
3.5.2	Turbulent structure	60
3.6	Conclusion	68
References		70

4	Fouling mitigation: An investigation by means of pulsed-flow	74
4.1	Abstract	75
4.2	Introduction	76
4.3	Experimental Methods	79
4.4	Experimental Procedure and Measuring Equipment	81
4.5	Results	84
4.6	Concluding Remarks	91
	References	93
5	Conclusions	98
	Appendix A New Facility for Membrane Fouling Investigations under Customizable Hydrodynamics: Validation and Preliminary Experiments with Pulsating Cross-Flow	102
	Appendix B Design drawings of the experimental fluid-dynamic apparatus for fouling reduction studies in membrane systems	107

List of Figures

2.1	Overview of the proposed setup: (a) Rendering of the entire hydraulic facility. (b) Sketch of test section used for the fluid-dynamic validation of the system. (c) Sketch of the test section used for membrane tests. (d) Representation of the system used to generate the pulsating flow, where ω is the rotation speed and k is the distance of the rod in respect to the elbow. The outflow area (red) varies during each cycle as a function of the angle of the truncated rod (in this setup set at 45°). Panel (b) also shows the reference system used in the present study; the origin is chosen at the right-bottom entrance of the test section and x, y, z coordinates correspond to streamwise, wall-normal and spanwise directions, respectively.	11
2.2	(a) Geometry of the convergent section and (b) result of a CFD simulation performed inside the fluid-dynamic convergent, connection and test section.	15

2.3 Velocity statistics obtained from PIV measurements in the lower half of the test section for three different streamwise positions; h is the channel semi-height, $u^+ = \bar{u} / u^*$ is the normalized velocity; $y^+ = y u^* / \nu$ is the normalized distance from the wall, Um is the maximum speed, $\sigma_v^+ = \sqrt{v'^2} / u^*$ and $\sigma_u^+ = \sqrt{u'^2} / u^*$ are the non-dimensional root squares of the variance for wall-normal and longitudinal velocity fluctuations, respectively, and $\sigma_{uv}^+ = \sqrt{v' u'} / u^*$ is the non-dimensional root square of the covariance. (a) Flow field and contour plot for test F-1; (b) total shear stress for all tests; (c) non-dimensional mean-velocity profiles (outer scaling); (d) non-dimensional mean-velocity profiles (inner scaling), the dashed line represent the linear law $u^+ = y^+$, characterizing wall flows for $y^+ \lesssim 5$; (e,f) non-dimensional profiles of velocity variances. Symbols and experimental conditions for all the tests are reported in Table 2.1, with the exception for \diamond that refers to the data from the DNS by Tsukara [29]. 22

2.4 Results of S-4_1.5 filtration test with a feed pressure of 1.5 bar; (a) fill levels of the three filtrate collection tanks vs. time; (b) total water flux and flux measured from the individual portions. In both panels, light blu, lavender and pink lines/symbols refer to, up, mid and down collection tanks, respectively (see Figure 3.3). Azure squares in panel (b) refer to the cumulative flux. 24

2.5 Data related to colloidal fouling of the membrane. (a) Photographs from the overhead camera taken over the entire span of the test section and at different times, t (test S-4_1.5); (b) percentage variation of the membrane color (yellow band) measured at different longitudinal positions along the membrane surface (i.e., in each of the red boxes highlighted in panel (a) as a function of time). 26

2.6 Dimensional (panel (a) and non-dimensional (panel (b) filtrate fluxes vs. time for all experimental conditions (symbols as indicated in Table 2.2). In Panel (b), filtrate fluxes are normalized by their initial value. 27

3.1	Suction rates: All the points are calculated as $\Gamma = V/U_\infty$ (where V is the mean vertical velocity through the porous media and U_∞ is the free stream velocity) except for the present in which is calculated as $\Gamma = V/U_m$ (where U_m is the maximum velocity in the centre of the channel). Green dots come from membrane experiments, light blue dots refer to perforated plate experiments, and orange dots refer to DNS and LEN studies. The black dotted line indicate the value beyond which relaminarisation occur [7].	37
3.2	Cross-flow scheme in a membrane module.	39
3.3	Overview of the proposed setup: (a) Rendering of the entire hydraulic facility; (b) Sketch of test section; (c) Sketch of the test section used for filtration tests where a thin flat sheet membrane leans on top of a high permeability stainless steel porous medium used simply as mechanical support. Panel (b) also shows the reference system used in the present study, the origin is chosen at the right-bottom entrance of the test section and x, y, z coordinates correspond to streamwise, wall-normal and spanwise directions, respectively.	40
3.4	Velocity statistics obtained from PIV measurements in the lower half of the test section at the streamwise position $x = 82.5, z=5$ cm (red stars) where h is the channel semi-height, $u^+ = \bar{u}/u^*$ is the normalised velocity, $y^+ = yu^*/\nu$ is the normalised distance from the wall; $\sigma_v^+ = \sqrt{\overline{v'^2}}/u^*$ and $\sigma_u^+ = \sqrt{\overline{u'^2}}/u^*$ are the non-dimensional standard deviations of the wall-normal and longitudinal velocity, respectively and $\overline{u'v'}$ is the Reynold shear stress.(a) non-dimensional mean-velocity profile (inner scaling), the dashed line represents the linear law $u^+ = y^+$, characterising wall flows for $y^+ \lesssim 5$ (see e.g., Pope [19]); (b) vertical profiles of σ_u^+ and σ_v^+ (outer scaling); (c) vertical profiles of σ_u^+ and σ_v^+ (inner scaling)and (d) non-dimensional Reynolds shear stress. Black diamonds indicate data from Tsukara [18], red stars indicate data from the benchmark test.	50

3.5 Results of the uncertainty analysis of the PIV data at different distances from the wall (h is the channel semi-height) normalised with the local mean streamwise velocity \bar{u} and reported in percentage form. Symbols and experimental conditions for all the tests are reported in Table 3.1. 51

3.6 Cross-flow scheme in a membrane module: Geometry of the test section (top) and representation of filtration process (bottom) where Q_{in} represent the feed flow, Q_{out} represent the residue of the process and Q_{ex} represent the permeate through the membrane. 52

3.7 Non-dimensional velocity profiles. h is the channel semi-height; \bar{u} is the local mean streamwise velocity and U_m is the maximum velocity at the centre of the channel. Symbols and experimental conditions for all the tests are reported in Table 3.1. 55

3.8 Non-dimensional shear stress; h is the channel semi-height and U_m is the maximum velocity at the centre of the channel. Symbols and experimental conditions for all the tests are reported in Table 3.1. 56

3.9 Non-dimensional profiles of the velocity variances for the stream-wise $\sigma_u^m = \sqrt{u'^2}/U_m$ and wall-normal $\sigma_v^2 = \sqrt{v'^2}/U_m$ directions; h is the channel semi-height and U_m is the maximum velocity at the centre of the channel. Symbols and experimental conditions for all the tests are reported in Table 3.1 56

3.10 Non-dimensional Reynolds stress; h is the channel semi-height and U_m is the maximum velocity at the centre of the channel and u' av' the velocity fluctuations in the streamwise and wall-normal direction, respectively. Symbols and experimental conditions for all the tests are reported in Table 3.1. 57

3.11 TKE production P and dissipation ε . Black diamonds indicate data from Tsukara [18], red stars indicate data from the benchmark test. 59

- 3.12 Production term $P = \overline{u'v'}(\partial\bar{u}/\partial y)$ and dissipation term $D = \varepsilon = 15\nu\overline{(\partial\bar{u}/\partial x)^2}$ of the Turbulent Kinetic Energy (TKE) balance in non-dimensional form. Gain and Loss are multiplied by h/U_m^3 ; h is the channel semi-height and U_m is the maximum velocity at the centre of the channel. Symbols and experimental conditions for all the tests are reported in Table 3.1. 60
- 3.13 Intensity ratio $Ir_{(ej)\vee(sw)} = \Sigma(u'v')_{(ej)\vee(sw)} / \Sigma(u'v')_{(tot)}$ and Occurrence ratio $Or_{(ej)\vee(sw)} = n_{(ej)\vee(sw)} / n_{(tot)}$ obtained from quadrant analysis at different y/h . "Ej" and "Sw" stand for Ejection and Sweep, respectively; u' and v' are the velocity fluctuations in the streamwise and wall-normal directions and n stands for the number of events. (a) Intensities of the Ejections; (b) Intensities of the Sweeps; (c) Occurrence of the Ejections and (d) Occurrence of the Sweeps. Symbols and experimental conditions for all the tests are reported in Table 3.1. 61
- 3.14 Non-dimensional autocorrelation coefficient $R = (\langle\overline{u'v'}\rangle) / (\langle\sqrt{u'^2}\rangle\langle\sqrt{v'^2}\rangle)$; h is the channel semi-height and u' and v' the velocity fluctuations in the streamwise and wall-normal direction, respectively. Symbols and experimental conditions for all the tests are reported in Table 3.1. 63
- 3.15 Large turbulence structures inclination angle: (a) Contour plot of the turbulent structure obtained from the two-point correlation $R_{uu}(X, Y) = \overline{u'(X, Y)u'(X + \Delta X, Y + \Delta Y)} / \sigma_{u(X, Y)}\sigma_{u(X + \Delta X, Y + \Delta Y)}$ for the impermeable wall condition. Coordinates of the point used for the calculation are $X = 7$ mm and $Y = 1.2$ mm, which corresponds to a ratio $Y/H_c = 0.24$ (this contour plot refers to the red star in panel b); (b) Inclination angle γ vs. suction rate $\Gamma = V/U$ (where V is the mean vertical velocity through the porous media and U the mean velocity of the feed flow) at the position $x = 7$ mm for three different distances from the wall $Y/H_c = 0.17$, $Y/H_c = 0.24$ and $Y/H_c = 0.32$. Symbols and experimental conditions for all the tests are reported in Table 3.1. 64

3.16 Power spectra analysis and non-dimensional velocity signals where k_x is the wave number $k_x = 2\pi f/\bar{u}$, $k_x E_{(uu)}$ is the spectral density of the longitudinal velocity component $k_x E_{uu} = (\bar{u}/2\pi)E_{(f)}$, \bar{u} is the mean velocity calculated from the time series of the eddy-convective velocity and time t is expressed in seconds. (a) Pre-multiplied power density spectra for smooth-wall impermeable condition and Reynolds number between 3000 and 12000; (b) Comparison of the pre-multiplied power density spectra at Reynolds number 4000 for the smooth-wall impermeable condition and BN flat-sheet membrane; (c) Non-dimensional velocity signal at $Re = 3000$; (d) Non-dimensional velocity signal at $Re = 4000$; (e) Non-dimensional velocity signal at $Re = 5000$; (f) Non-dimensional velocity signal at $Re = 6000$; (g) Non-dimensional velocity signal at $Re = 8400$; (h) Non-dimensional velocity signal at $Re = 12000$. Panel (a) also show the line for $k_x = 1000$ corresponding to the length of near-wall streaks. Symbols and experimental conditions for all the tests are reported in Table 3.2 66

4.1 Rendering of the hydraulic facility. 79

4.2 Total water flux and measured from the individual portions: (a) Test S-4_1.5; (b) Test P-4_1.5_2.5_LA. In both panels, light blu, lavender and pink squares refer to up, mid and down collection tanks respectively and azure squares refer to cumulative flux. . . 84

4.3 Photo of the entire membrane taken with the overhead camera (Panel (a)) and percentage variation of the membrane color (yellow band) measured at different longitudinal positions along the membrane surface as a function of time for steady ((b) Test S-4_1.5) and pulsed flow conditions ((c) Test P-4_1.5_2.5_LA). . . 85

4.4	Dimensional filtrate flux vs. time: (a) Steady vs. low amplitude pulsating flow for different adimensional frequencies; (b) Steady vs. low and high amplitude pulsating flow at the same adimensional frequency. Symbols and experimental conditions for all the tests are reported in Table 4.1.	88
4.5	Non-dimensional filtrate flux vs. time: (a) Steady vs. low amplitude pulsating flow for different adimensional frequencies; (b) Steady vs. low and high amplitude pulsating flow at the same adimensional frequency. Symbols and experimental conditions for all the tests are reported in Table 4.1.	90
A.1	Pipes and instrumentation diagram (i.e. <i>P&ID</i> Diagram) of the overall facility.	104
A.2	Time series of (a) the longitudinal u' and (b) wall-normal v' velocity fluctuations deduced by PIV measurement at the position F-2 and coordinates $x = 17$ mm and $y = 2.5$	105
A.3	Contour plot of (a) the longitudinal u' and (b) wall-normal v' velocity fluctuations deduced by PIV measurement at the position F-2 at fixed time $T = 4.8$ s.	105
A.4	Results of filtration test S - 4.1: (a) Total water flux measured from the individual portions (where light blu, lavender and pink symbols refer to up, mid and down collection tanks respectively and azure squares refer to the cumulative flux) and (b) percentage variation of the membrane colour (yellow band) measured at different longitudinal positions along the membrane surface. . .	106
B.1	Main tank.	108
B.2	Supports of the main tank.	109
B.3	Flexible connection pipes.	110
B.4	Upper and lower part of the connection between the fluid-dynamic convergent and the test section.	111

B.5	Side part of the connection between the fluid-dynamic convergent and the test section.	112
B.6	Circular flange for connection with the fluid dynamic convergent.	113
B.7	Rectangular flange for connection with the test section.	114
B.8	Assembly of the connection.	115
B.9	Upper part of the test section.	116
B.10	Lateral upper part of the test section.	117
B.11	Upper and lower* flange of the test section. *Filtration tests. . .	118
B.12	Assembly of the upper part of the test section.	119
B.13	Lower part of the test section for smooth-wall impermeable tests.	120
B.14	Lower flange of the test section for smooth-wall impermeable tests.	121
B.15	Assembly of the lower part of the test section for smooth-wall impermeable tests.	122
B.16	Lateral lower part of the test section.	123
B.17	Lower part of the test section for filtration tests.	124
B.18	Update of the lower part of the test section for filtration tests. . .	125
B.19	Internal dividers of the lower part of the test section.	126
B.20	Assembly of the lower part of the test section for filtration tests.	127
B.21	Rectangular flange for connection with the post test section. . .	128
B.22	Flow-dynamics convergent pipe.	129
B.23	Flange for the flow-dynamics convergent pipe.	130
B.24	Assembly for the flow-dynamics convergent pipe.. . . .	131
B.25	Straight pipe DN 250.	132
B.26	DN 250 tube with 90° bend.	133
B.27	Hand made divergent.	134

B.28	Assembly of the hand made divergent.	135
B.29	Pipe 1 of the main line DN 32.	136
B.30	Pipe 2 of the main line DN 32.	137
B.31	Pipe 3 of the main line DN 32.	138
B.32	Pipe 4 of the main line DN 32.	139
B.33	Pipe 5 of the main line DN 32.	140
B.34	Pipe 6 of the main line DN 32 to DN 25.	141
B.35	Pipe 7 of the main line and by-pass line DN 25.	142
B.36	Pipe 8 of the main line DN 25.	143
B.37	Pipe 9 of the main line DN 25 to DN 32.	144
B.38	Pipe 10 of the main line DN 32.	145
B.39	Pipe 11 of the main line DN 32.	146
B.40	Pipe 12 of the main line DN 32.	147
B.41	Pipe 13 of the main line DN 32.	148
B.42	Pipe 1 of the by-pass line DN 25 to DN 32.	149
B.43	Pipe 2 of the by-pass line DN 32.	150
B.44	Post test section.	151
B.45	Welding of the post test section.	152
B.46	Supports of the main flow-dynamic convergent, Straight pipe DN 250 and DN 250 tube with 90° bend.	154
B.47	Supports of the hand made divergent	155
B.48	Supports of the electric engine	156

List of Tables

2.1 Summary of the chosen hydraulic conditions to perform the flow-dynamic tests. The columns indicates: the Reynolds number, $Re = Uh/\nu$, the viscous Reynolds number, $Re^* = u^*h/\nu$, the maximum speed, U_m and the friction velocity, $u^* = \sqrt{\tau_0/\rho}$. For all tests, 2000 image pairs (window size 34.5 mm \times 5 mm) were analyzed with a grid step size of 16 \times 16 pixels and a spatial accuracy of 0.19 \times 0.19 mm. 18

2.2 Provides a summary of all experimental conditions for filtration tests. The columns indicate: the Reynolds number, $Re = Uh/\nu$, the pressure, p , the suction coefficient, $\Gamma = V/U$ and the non-dimensional frequency, $\omega^+ = 2\pi f\nu/u^{*2}$ 20

3.1 Summary of the experimental conditions for benchmark and filtration tests. U is the bulk velocity in the channel; U_m is maximum velocity as obtained from PIV measurements; $Re = Uh/\nu$ is the Reynolds number where ν is the kinematic viscosity of water at the mean measured temperature T ; p is the gauge pressure measured within the test section; J is the amount of permeate observed for each experiments during velocity measurements; $\Gamma = V/U$ is the suction rate with V being a vertical velocity estimated as the flux divided by the membrane surface area; $\Delta_{x,y}$ is the pixel size in the images grabbed using the PIV system described in Section 3.4.1 and "Grid" identify the size (in pixels) of the interrogation area employed for the analysis of PIV images. 42

3.2	Summary of the experimental conditions for LDA measurements. The columns indicate: the distance at which LDA measurements are taken (centre of the channel); the eddy-convection velocity that correspond to the local mean streamwise velocity U ; the Reynolds number $Re = Uh/\nu$; the mean temperature T ; the mean pressure p ; the amount of flux through the membrane; the suction rate $\Gamma = V/U$ and the number of samples acquired.	48
4.1	Summary of all experimental conditions for filtration tests. The columns indicate: the flow regime, the mean Reynolds number, $Re = Uh/\nu$, the mean pressure, p , the suction coefficient, $\Gamma = V/U$, the dimensional frequency, f , the non-dimensional frequency, $\omega^+ = 2\pi f\nu/u_*^2$ or $ls^+ = \sqrt{2/\omega^+}$, the dimensionless propagation length, $T^* = T_w u_*/h$ and the ratio between the velocity oscillation and the average velocity in the mid heigh of the channel, Ac . The limts of each flow regime are written in blue .	82
A.1	Geometries and properties of the main hydraulic components. .	103

Nomenclature

Roman Symbols

\overline{E}_u	Mean streamwise measurement error [m]
$\overline{u'v'}$	Covariance [m^2s^{-2}]
\bar{u}	Streamwise mean velocity [ms^{-1}]
Ac	Non dimensional wave amplitude [$-$]
b	Test section width [m]
$D = \varepsilon$	Dissipation term of the Turbulent kinetic Energy [J/kg]
D_{50}	Characteristic particle diameter [μm]
E_{uu}	1-D wavenumber spectrum of the streamwise coordinates [m^3s^{-2}]
H	Hole parameter [$-$]
h	Semi-height of the channel [m]
H_c	Cross-correlation semi-height of the channel [m]
Ir	Intensity ratio [%]
J	Flux rate [$lm^{-2}h^{-1}bar^{-1}$]
J_{cum}	Cumulate flux rate [$lm^{-2}bar^{-1}$]
k	Distance between the rod and the elbow [cm]

k_x	Wavenumber [m^{-1}]
L	Test section length [m]
M	Magnification factor $[-]$
Or	Occurrence ratio [%]
P	Production term of the Turbulent kinetic Energy [J/kg]
p	Pressure [bar]
Q_{ex}	Permeate flow rate [lh^{-1}]
Q_{in}	Feed flow rate [lh^{-1}]
Q_{out}	Residue flow rate [lh^{-1}]
R	Correlation coefficient $[-]$
R_{uu}	Cross-correlation of longitudinal velocity $[-]$
Re	Reynolds number $[-]$
Re_τ	Friction Reynolds number $[-]$
rs	Rotation speed [RPM]
T	Temperature [$^{\circ}C$]
t	Time [h]
T^*	Dimensionless propagation length $[-]$
T_w	Wave period [s]
U	Bulk velocity [ms^{-1}]
u	Streamwise instantaneous velocity [ms^{-1}]
u'	Streamwise velocity fluctuation [ms^{-1}]
u^+	Normalised velocity $[-]$

u^*	Friction velocity [ms^{-1}]
U_m	Maximum velocity [ms^{-1}]
U_∞	Free stream velocity [ms^{-1}]
V	Permeate velocity [ms^{-1}]
v	Wall-normal instantaneous velocity [ms^{-1}]
v'	Wall-normal velocity fluctuation [ms^{-1}]
X	Cross-correlation longitudinal coordinate [m]
x	Longitudinal coordinate [m]
Y	Cross-correlation wall-normal coordinate [m]
y	Vertical coordinate [m]
y^+	Normalised wall-distance [—]
z	Spanwise coordinate [m]

Greek Symbols

Δ	Spatial distance [m]
δ	Boundary layer thickness [m]
Δ_t	Time interval [s]
$\Delta_{x,y}$	Pixel size [mm]
Γ	Suction rate [—]
γ	Structure inclination angle [deg]
Γ_{SST}	Critical suction rate [—]
ν	Kinematic viscosity [m^2s^{-1}]
ω^+	Dimensionless frequency [—]

ρ	Fluid density [Kgm^{-3}]
τ	Total shear stress [Nm^{-2}]
τ_0	Wall shear stress [Nm^{-2}]
τ_t	Turbulent shear stress [Nm^{-2}]
τ_v	Viscous shear stress [Nm^{-2}]
σ_u	Standard deviation of the spanwise velocity [—]
σ_u^+	Standard deviation of the streamwise velocity normalised with u^* [—]
σ_u^m	Standard deviation of the streamwise velocity normalised with U_m [—]
σ_v	Standard deviation of the wall-normal velocity [—]
σ_v^+	Standard deviation of the wall-normal velocity normalised with u^* [—]
σ_v^m	Standard deviation of the wall-normal velocity normalised with U_m [—]
σ_{uv}^+	Covariance normalised with u^* [—]
l_s^+	Nondimensional frequency [—]

Acronyms / Abbreviations

$1 - D$	One-Dimensional
$2 - D$	Two-Dimensional
BN	Flat-sheet membrane type
DNS	Direct Numerical Simulations
Ej	Ejection
HA	Hight wave amplitude
HA	Low wave amplitude
LDA	Laser Doppler Anemometry

LES Large Eddy Simulations

LY Flat-sheet membrane type

PES Molecular weight cut-off

PES Polyethersulfone

PIV Particle Image Velocimetry

QA Quadrant analysis

Sw Sweep

TASBLs Turbulent asymptotic suction boundary layers

TKE Turbulent Kinetic Energy

TTS Total suspended solids

VLSM Very Large Scale Motions

Chapter 1

Introduction

This chapter is subdivided into an initial section (Section 1.1) containing a brief general overview of the problem under study, followed by a section (Section 1.2) dedicated to explaining the aim and objectives of this work and a concluding section (Section 1.3) providing the contents of the thesis.

1.1 Problems related to membrane fouling

Membrane systems suffer from two main operational problems: concentration polarisation and fouling. While the former, due to the semi-permeability and selectivity of the membrane, results in a reversible accumulation of rejected solutes at the feed-membrane interface, the latter can lead to an irreversible loss of permeability and damage to the membrane as the matter in the feed solution leaves the liquid phase to form a deposit on either the membrane surface or inside its porous structure.

The increase of the osmotic pressure and hydraulic resistance induced across the membrane requires a higher driving force and periodic cleaning methods to maintain a constant flux rate, which results in additional energy and operational costs. These effects correlated to separation mechanisms that involve an increase in the concentration of solutes in the feed stream are physically unavoidable, and mitigation techniques, as much effective as possible and easily implementable, are therefore required. In this sense, literature provides experience related to different methods ranging from surface treatment and cleaning with chemical agents, intermittent backflushing, dynamics and flow-dynamic techniques.

In this panorama, pulsed hydrodynamic methods have proven to respond to the previous requirements and help to improve the permeate flux in all types of membrane applications relative to the steady-state. However, despite the widespread investigation into this matter, only a poor knowledge of the physics underlying the improvement in the system's performance is available since most of the studies in the field refer to dimensional quantities rather than flow behaviour. To bridge this knowledge gap, a physical approach to the problem is needed in order to understand how the turbulent properties of the flow are altered in the presence of

suction flows with respect to the canonical channel flow condition (under the same condition of the imposed flow) and how the main parameters of the unsteady flow (i.e. amplitude and frequency of the imposed instability) acts to and modify the mass transport mechanisms responsible for mixing and particle removal.

In the work herein presented, both aspects are treated with particular attention under well-controlled flow conditions representative of membrane systems (i.e. low Reynolds numbers and uniformly distributed porosity over the entire wall) in order to get further information on suction effects induced by lower suction rates than those previously investigated (i.e. below flow relaminarisation) and to grab evidence of instability effects through the use of non-dimensional quantities.

1.2 Aims and objectives

This PhD project aims at experimentally investigating fluid dynamics and mass transfer processes associated with membrane systems, with a view to explore to what extent pulsating flow techniques can contribute to mitigate fouling. In order to fulfill this aim, the following objectives are set:

1. Design, build and validate an ad hoc facility devoted to investigating the clogging phenomenon related to membranes separation process in well-controlled flow dynamics conditions.
2. To evaluate the effects of suction in channel flow turbulence as a means to explore how flow characteristics in membrane systems are affected when permeate fluxes are changed.
3. To explore the effects of pulsating flow conditions on particle deposition during filtration experiments in membrane systems.

1.3 Thesis contents

In this thesis, each chapter is stand alone and composed of (i) an introductory section explaining the relevance of the problem under investigation and the relevant literature review (ii) a thorough description of experimental method; (iii) results and (iv) conclusions. A brief outline of the contents of each chapter is given below::

Chapter 2: describes the facility used for all the experiments reported in the thesis and points out the design criteria used for its construction. In addition, preliminary results are presented from both fluid-dynamic measurements and filtration tests, performed under stationary and pulsed flow conditions, which were used to validate the system.

Chapter 3: is dedicated to the characterisation of the main velocity statistics and turbulence structure under steady flow conditions over a smooth-impermeable wall and for porous membranes of different permeability. The main effects induced by the suction for a wide range of pressures applied to the feed flow are presented and discussed.

Chapter 4: assess fouling mitigation through the use of pulsed-flow conditions. The effects related to the variation of the surface deposition rates and the amount of permeate are discussed in relation to the physics of the observed fluid-dynamic behaviour.

Chapter 5: summarise the key outcomes in this study.

In addition, two Appendix are provided; *Appendix 1* summarises some additional information regarding system validation, and *Appendix 2* collects all the design drawings of the experimental fluid-dynamic apparatus whose design and construction have required a year and a half of the PhD program.

Chapter 2

New Facility for Membrane Fouling Investigations under Customizable Hydrodynamics: Validation and Preliminary Experiments with Pulsating Cross-Flow

2.1 Abstract

Flux reduction induced by fouling is arguably the most adverse phenomenon in membrane-based separation systems. In this respect, many laboratory-scale filtration studies have shown that an appropriate use of hydrodynamic perturbations can improve both performance and durability of the membrane; however, to fully understand and hence appropriately exploit such effects, it is necessary to understand the underpinning flow processes. Towards this end, in this work we propose and validate a new module-scale laboratory facility with the aim of investigating, at very well-controlled flow conditions, how hydrodynamics affects mass transport phenomena at the feed/membrane interface. The proposed facility was designed to obtain a fully developed and uniform flow inside the test section and to impose both steady and pulsating flow conditions. The walls of the facility were made transparent to grant optical accessibility to the flow. In this paper, we discuss data coming from Particle Image Velocimetry (PIV) measurements and preliminary ultrafiltration tests both under steady and pulsating flow conditions. PIV data indicate that the proposed facility allows for excellent flow control from a purely hydrodynamic standpoint. Results from filtration tests provide promising results pointing towards pulsating flows as a viable technique to reduce fouling in membrane systems.

2.2 Introduction

Water management is a highly topical issue and will be even more so in the near future. According to the United Nations Water Resources Report 2021, the use of freshwater has increased six-fold in the last 100 years and demand continues to grow by 1% per year [1]. In this perspective, desalination plants offer an economically viable solution for the production of drinking water. Starting from 326 m³/day produced worldwide in 1945, the use of this technology based on membrane systems has increased exponentially to over 80 million m³/day in 2013 [2, 3] and even more today. Moreover, thanks to their versatility, membranes have also found increasing use in other processes related to the food, medical and chemical sectors and more generally in the treatment of wastewater from industrial plants [4–6]. In relation to the importance acquired, due to the vastness of the possible uses, there has also been a natural expansion of the research-related sector with a strong increase in the number of studies and publications [7] relating to process optimization and new applications.

Although technological development [8, 9] and process intensification efforts have improved membrane separation processes significantly, fouling still represents a major issue, as it causes a decrease in productivity resulting from the accumulation of particles, microorganisms and macromolecules on the membrane surface with consequent negative outcomes in terms of permeate quality and increased energy consumption. Mitigating such fouling effects essentially means finding ways to minimize deposition at the fluid–membrane interface while granting a reasonable amount of filtrate flux. This may be achieved by maximizing mixing in the feed while minimizing energy expenditure to generate it. Towards this end, the so called “hydrodynamic methods” offer an interesting opportunity. In a recent review paper, Jaffrin [10] (and references therein) provides an appraisal of all such methods and highlights that an appropriate use of hydrodynamic perturbations can improve the performance of membrane filtration at low energetic costs quite significantly. For example, in addition to the classical retro-filtration approach, applications of helicoidal flows, vibrating and rotating systems and pulsating flows are reported and deemed to be promising.

While the potential of these techniques is not in doubt, the physics underpinning the processes leading to the observed reduction in fouling is not well understood and results provided by the literature are often presented in dimensional form [11–14], which makes them have no general validity and only a (weak) support for an empirical, and hence unreliable, design of anti-fouling hydrodynamic techniques.

The aim of the present paper is to propose, test and validate a novel experimental facility designed and built with the intention of providing data that will help bridge this knowledge gap. The proposed facility was designed considering similarity principles and allowing for state-of-the-art laser diagnostics techniques to measure flow velocities and mass transfer process occurring at the membrane-feed interface. Aside from steady flows, the current version of the experimental set-up allows for the generation of pulsating flows, which are identified by the authors as a hydrodynamic method that combines a good potential for fouling reduction with ease of implementation and installation in industrial applications. Some preliminary results are presented in support of this hypothesis.

The paper is organized as follows: Section 2.3 is devoted to the accurate description of the facility as well as its design rationale. Section 2.4 describes the equipment and experimental procedures adopted in the tests. Section 2.5 presents results with a view to demonstrate that: (i) the facility was well-designed from a fluid-dynamics stand-point and allows for the generation of nicely controllable canonical channel flows that can be investigated by means of laser diagnostic techniques; (ii) filtration tests are responsive to changes in flow conditions and provide repeatable and encouraging results especially for what concerns pulsating flow conditions. Section 2.6 presents overall conclusions from the present study.

2.3 Experimental Methods

2.3.1 Overall Description of the Facility

The hydraulic plant shown in Figure 3.3a, mainly made in stainless steel 316L to ensure durability, is a recirculating facility whereby the feed is drawn from a 1 m³ (constant-head) main tank by a pumping system consisting of two in-parallel multistage pumps, with a maximum total flow rate of 2.4 l/s. The two pumps are mounted on two separated pipe-branches equipped with in-line ball valves for sectioning the circuit and imposing a wide range of flow rates to cover laminar, transitional and turbulent flow regimes in the test section. Just further downstream, the system splits into a main pipeline and a by-pass line that returns a selected fraction of the feed directly to the reservoir. Along the former, after a few meters, a divergent allows for connection to a flow conditioning system made of a settling chamber and a contraction that minimizes incoming turbulence and allows for the undisturbed development of boundary layers within the test section (the flow conditioning section is described in detail below). At the downstream end of this test section, a sensor records hydraulic pressure in real-time and a short stretch of pipe closes the hydraulic circuit. Where possible, small diameters have been used, partly to reduce the total volume and partly to better control the flow rate in the main line. Details about pipe diameters, tanks capacity (i.e., both the main tank and the collecting tanks), test section and pump types with three points of the flow vs. pressure curve are provided in Table A.1 in the Appendix A.

The desired conditions in terms of pressure and flow rate are achieved through the combined regulation of pump frequency and control devices. A computer-programmable inverter allows us to fix the rotational speed of the pump shaft. The two globe valves on the delivery line are used to set the amount of water in each branch and one valve on the return line, downstream of the test section, acts as a back-pressure valve. Two self-closing air release valves are then installed at the highest elevations of the pressurized part of the circuit to allow for air removal. Right below the test section, three small trays collect the filtrate.

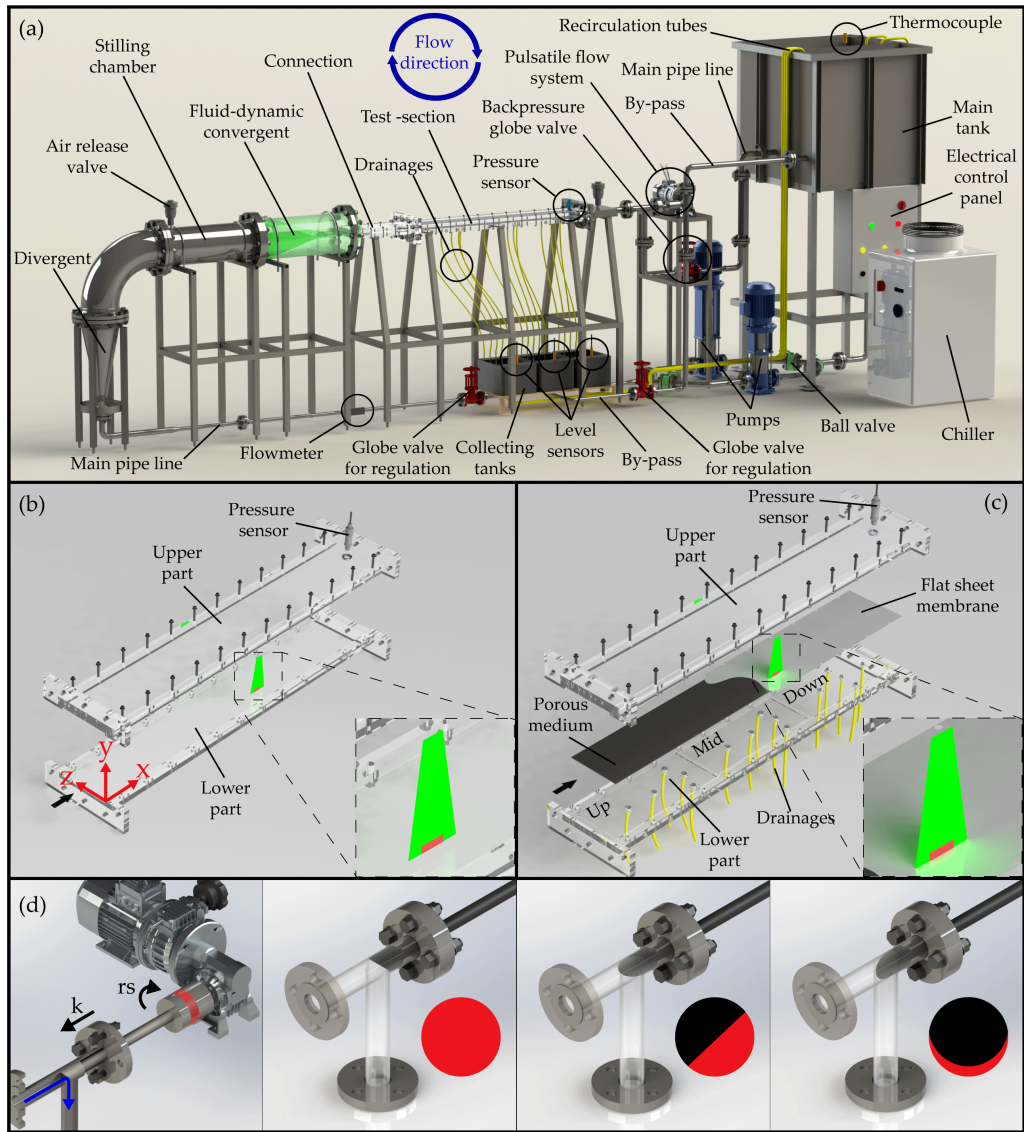


Fig. 2.1 Overview of the proposed setup: (a) Rendering of the entire hydraulic facility. (b) Sketch of test section used for the fluid-dynamic validation of the system. (c) Sketch of the test section used for membrane tests. (d) Representation of the system used to generate the pulsating flow, where rs is the rotation speed and k is the distance of the rod in respect to the elbow. The outflow area (red) varies during each cycle as a function of the angle of the truncated rod (in this setup set at 45°). Panel (b) also shows the reference system used in the present study; the origin is chosen at the right-bottom entrance of the test section and x , y , z coordinates correspond to streamwise, wall-normal and spanwise directions, respectively.

Their emptying is regulated automatically by ultrasonic level sensors that control the on/off sequences of the bilge pumps. The filtrate then returns, via recirculation tubes, to the main tank to maintain a constant water volume in the whole system. The overhead tank is equipped with a thermocouple that allows for the monitoring of water temperature. An ultrasonic flow meter is mounted on the main line and a pressure sensor at the end of the test section. These were chosen with an appropriate level of accuracy, namely, 2% for $u > 0.3$ m/s for the AcquaTrans™ AT600 flow meter manufactured by Panametrics, and 0.008 bar for the Wika P-30 pressure sensor. Flow rate and pressure data, acquired at whatever desired frequency, are transmitted with a 4–20 mA signal to a National Instruments data acquisition card by means of a Labview program. To avoid changes in water density and in membrane hydraulic conductivity, temperature is kept constant by means of a 5 kW chiller. For a better and more detailed understanding of the overall system operation, reference should be made to the "Piping and instrumentation diagram" (P&ID) available in Figure A.1 of the Appendix A.

2.3.2 Description of the Test Section

The main part of the system is the test section (test section is often used as fluid dynamicists' jargon, while the community pertaining to membrane science often refers to it as housing cell or simply cell; all these names are herein used interchangeably), which houses the flat-sheet membrane. The section consists of a rectangular channel (1.45 m long, 0.2 m wide and 0.01 m high) made entirely of transparent plexiglass, which allows for optical access to cameras and lasers, hence assessment of membrane surface alteration and velocity measurements at any location (e.g., for measurements by means of particle image velocimetry, PIV, as presented herein).

Figure 3.3b shows the configuration of the housing cell hosting an impermeable smooth surface that was used for checking flow development under canonical channel flow conditions and as a benchmark for comparison with flows developing over porous membranes. Figure 3.3c provides details of the cells when equipped with the flat-sheet membrane. The upper wall of the housing is the same as in

Figure 3.3b. The lower part is made of a rigid stainless steel porous medium (3.175 mm thick, 316LSS porous medium with uniformly distributed 10 μm pores providing support for different types of flat-sheet membrane. The medium leans over a plexiglass bed that was subdivided into three separate compartments to collect the filtrate from different locations along the direction of the flow and hence to check for spatial uniformity of filtration rates during an experiment. Towards this end, the bed of each compartment has five bottom holes connected to drainage pipes that convey water to the underlying trays where level meters allow for the monitoring of filtrated water volumes over time and hence of filtrate flow rates as sought.

The design of the test section was carried out to accommodate the following requirements:

- (i) The development of a so-called “canonical” channel flow (i.e., a rectangular channel flow as largely investigated within the remit of the literature pertaining to fluid dynamics) allowing for full control and extensive validation of flow properties. Following the recommendations from the literature, the channel was designed with a large aspect ratio (i.e., ratio between width and depth) of 20, which allows flow properties in the mid cross section to be independent of lateral walls and hence comparable to theoretical predictions as well as measured or numerically modeled data [15];
- (ii) The length, L , of the channel had to be minimized to avoid working with very large volumes of water while allowing for fully developed and self-similar flows (i.e., flows whose velocity statistics, once appropriately scaled, are independent of the longitudinal coordinate) to form. This put constraints on the height $2h$ of the channel, because the higher the $2h$ the longer is the required L to obtain fully developed flows [16].

Requirements (i) and (ii) were nicely met with the test section having the following geometry: $L = 1.45$ m, $2h = 0.01$ m and width $b = 0.2$ m. It is worth mentioning that the proposed facility was designed to investigate, at a fundamental level, how mass transfer processes occurring at the feed–membrane interface respond to a range of imposed (and well controllable) flow conditions, and not to

replicate geometric features as encountered in industrial applications. The latter goal would indeed require working with complex geometries (see, e.g., spiral wound or pressurized hollow-fiber modules) that would make this job extremely challenging. Nevertheless, it was deemed necessary to design the test section to allow for dynamic and kinematic similarity with industrial flows. To the authors' opinion, the two non-dimensional numbers that dictate the achievement of the sought similarity are the already mentioned Reynolds number, $Re = Uh/\nu$, and the so-called suction coefficient, $\Gamma = V/U$ [17], where V is the vertical velocity at the feed-membrane interface and U is the bulk mean velocity of the overlying channel flow. Whenever these two numbers have each an equivalent value in different systems (e.g., our lab setup and an industrial setup, or two lab setups), the systems may be considered equivalent from a hydrodynamics standpoint. The chosen system of pipes and test section geometry permits to impose a wide range of feed-flow velocities, U , and internal pressures to be explored. These conditions result in the possibility to impose a wide range of Re ($1000 \div 20,000$) and achieve a large range of Γ (covering up to two orders of magnitude) in relation to the permeability of the installed membrane sheet and applied pressure. Indeed, the proposed setup nicely covers typical hydrodynamics conditions used in industrial settings spanning from microfiltration to nanofiltration applications.

2.3.3 Description of the Flow-Conditioning Unit and Pulsating Flow System

Much of the quality of the flows that develop in the test section depends on the reliability and functioning of the flow conditioning unit, which is described in detail as follows. The abrupt widening of the settling chamber is designed to slow the fluid down so that quasi-irrotational motion can be established. Further downstream, the fluid gradually re-accelerates while flowing into the ad hoc designed convergent that allows for further turbulence dissipation through the imposition of a strong favorable pressure gradient, which is known to be effective for flow laminarization [18, 19]. The design of the flow conditioning unit was a non-trivial task and driven by the need to meet several requirements. In particular:

- (i) The contraction ratio (the ratio between the cross-sectional area of the settling chamber and the test section) had to be at least equal to 4 for an effective turbulence damping to take place [20, 21];
- (ii) The convergent had to be gradual to avoid boundary layer separation and the potential shedding of undesired eddies resulting from boundary layer separation;
- (iii) The convergent shape was very unconventional (i.e., never investigated before) as it had to gradually join the bulk circular cross section of the settling chamber to the wide and thin rectangular slit of the test section.

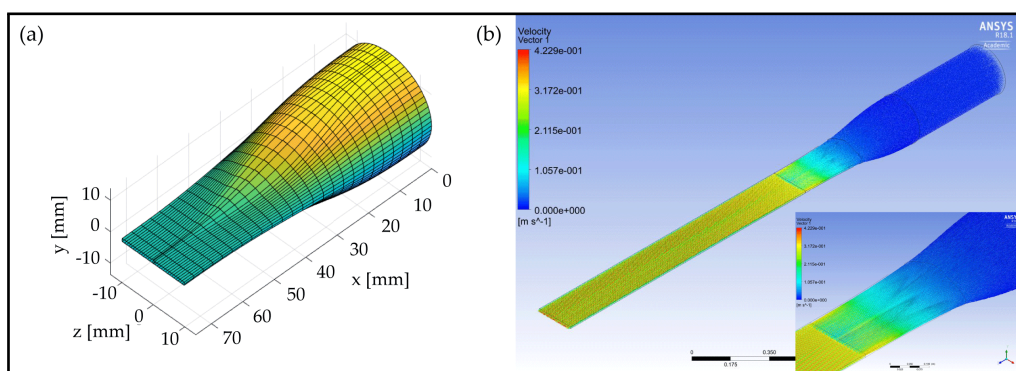


Fig. 2.2 (a) Geometry of the convergent section and (b) result of a CFD simulation performed inside the fluid-dynamic convergent, connection and test section.

To meet all these requirements, the entire conditioning unit was carefully designed with the aid of computational fluid dynamics (CFD) and various numerical simulations were carried out assuming laminar and turbulent flow conditions to develop in the unit (see an example in Figure 2.2). For both the conditions corresponding to a Reynolds number within the test section of 1000 and 10000, respectively six different meshes (1.08 to 11.94 million cells) were adopted to verify the independence of the results, and for the latter, CFD simulations were performed with both the $k - \omega$ and $k - \epsilon$ turbulent closure models.

Results from the simulations indicated that the chosen geometry allowed for smooth flow acceleration and a laterally uniform flow developing within the test

section. Concerning the generation of pulsating flows, Figure 3.3d illustrates the proposed device which is based on the work published by Ramaprian and Tu [22]. A rod with a 45° angle cut was inserted into a 90° elbow and connected to a 0.37 kW electric motor equipped with speed drivers and gears. By adjusting the rotation speed, rs ($5 \div 143$ RPM), and the distance, k , of the rod with respect to the elbow, the ratio between the outflow area and the pipe diameter can be varied harmonically and a pulsating flow established in the system.

2.4 Experimental Procedure and Measuring Equipment

This section describes the measuring systems and procedures used to carry out the experiments. The section is divided in two parts. Section 2.4.1 is devoted to the description of the (herein called) fluid dynamic tests, which were carried out with the unit equipped with an impermeable plexiglass floor with the goal to test the development of canonical channel flows. Section 2.4.2. reports how filtration tests were carried out and describes the experimental technique used to monitor membrane fouling.

2.4.1 Fluid Dynamic Tests

Velocity measurements were carried out by means of a PIV system. This technique employs a series of image pairs, acquired at predefined time intervals, to evaluate the displacement of individual seeding particles illuminated by a planar laser sheet. Image pairs are compared using a cross-correlation algorithm, providing a two-dimensional velocity field with a spatial accuracy of 16×16 pixels, herein corresponding to approximately 0.19×0.19 mm. The equipment used in this study is a PIV Dantec system consisting of a 200 mJ YAG laser (wavelength of 532 nm corresponding to green light) that can be shot at a maximum frequency of 15 Hz. Images were acquired by means of an IMPEREX c-4080 camera (sensor size 18.8×14.1 mm) coupled to a 200 mm Nikon lens. The laser beam is conveyed through an optic-fiber cable into a mechanical arm ending with an optical unit made of cylindrical and spherical lens that allow for laser sheet generation and control in terms of width and focusing. Both optical unit and camera were mounted on a structure of modular aluminum profiles that allowed for very precise positioning and control of the alignment and parallelism between the camera, the main flow direction and the laser plane, whose thickness in the present experiments was set between 1 and 2 mm. Acquired images were then calibrated using a custom-built calibration plate inserted within the unit and then analyzed with DynamicStudio 6.4 to work out the velocity field.

Table 2.1 Summary of the chosen hydraulic conditions to perform the flow-dynamic tests. The columns indicates: the Reynolds number, $Re = Uh/\nu$, the viscous Reynolds number, $Re^* = u^*h/\nu$, the maximum speed, U_m and the friction velocity, $u^* = \sqrt{\tau_0/\rho}$. For all tests, 2000 image pairs (window size 34.5 mm \times 5 mm) were analyzed with a grid step size of 16 \times 16 pixels and a spatial accuracy of 0.19 \times 0.19 mm.

Test Name	Symbol	Coordinates [cm]	Re [-]	Re^* [-]	U_m [m/s]	u^* [m/s]
F-1	▼	x = 82.5, z = 5	3981	74	0.287	0.0148
F-2	●	x = 34.5, z = 5	3981	74	0.287	0.0144
F-3	■	x = 130.5, z = 5	4038	74	0.285	0.0145

Measurements aiming at checking flow uniformity within the test section were taken at three different longitudinal positions and a fixed distance from the channel side wall (i.e., $z = 5$ cm). In particular, with reference to the coordinate system presented in (Figure 3.3b) the laser sheet was first placed in the cross section identified by longitudinal coordinate $x = 82.5$, then at an upstream ($x = 34.5$) and finally at a downstream cross section ($x = 130.5$), respectively. Each of the three PIV acquisitions was conducted at the same dimensionless Reynolds number $Re = Uh/\nu \approx 4000$ (U is the mean bulk velocity, h is the semi-height of the channel and ν is the kinematic viscosity) or equivalently, $Re^* = u^*h/\nu = 74$ (u^* is the friction velocity defined as $u^* = \sqrt{\tau_0/\rho}$, where ρ is the fluid density and τ_0 is the wall shear stress, namely, the friction forces per unit area acting at the bottom wall), to achieve dynamic similarity with flows typically established in traditional membrane systems [23, 24]. Since at this Re the flow is turbulent, 2000 image pairs were acquired, in order to estimate both first and second-order velocity statistics, with good confidence. A summary of experimental acquisitions is given in Table 2.1 in which we want to point out that the small differences in the Reynolds numbers are attributable to experimental variability.

2.4.2 Filtration Tests

Experimental findings were obtained from pulsating and steady-state flow tests. In both cases, 5 g of kaolin ($D_{50} = 1.5 \mu\text{m}$) and 10 g of green clay ($D_{50} = 0.2 \mu\text{m}$), which represent the main colloidal foulants in this application, were added to 555 l of tap water (feed concentration $c = 27$ ppm and feed viscosity $\nu = 10^{-6} \text{ m}^2/\text{s}$), in order to reproduce the same total suspended solids (TSS) concentrations and similar particle composition as encountered in a nearby river (Po River [25, 26]), which is currently used as main source of water for the city of Turin, and whose water will be soon potabilized by means of a new ultrafiltration plant, which is currently being installed by the water provider. A new polyethersulfone (PES) Synder-LY ultrafiltration flat-sheet membrane with a molecular weight cut-off (MWCO) of 100,000 Da and a nominal permeance between 80 and 123 l/m²/h/bar was mounted in the housing section for each test. An average Re of 4000 was maintained in all tests with a constant fluid temperature (in the range of $18 \div 20$ °C) and the applied pressure, p , was chosen between 1 and 1.5 bar. At these conditions, the suction parameter Γ varied between 1.37×10^{-4} and 1.84×10^{-4} . In order to also obtain preliminary data about potential fouling reduction under pulsating flow conditions, one experiment was carried out under the same hydraulic conditions as per the steady filtration tests (i.e., $Re \approx 4000$ and $\Gamma 1.37 \div 1.84 \times 10^{-4}$) but, this time, forcing the flow rate and pressure to undergo oscillations induced by the pulsed flow system described in Section 2.3.3 (see also Figure 3.3d). Towards this end, the distance between the rod and the elbow, k , was set to 13.3 cm and the rotation frequency equal to 0.09 Hz. This corresponds to variations of pressure and flow rate contained between 1.51 ± 0.04 bar and 0.42 ± 0.035 l/s, respectively. The frequency of the imposed oscillations sets the dimensionless frequency $\omega^+ = 2\pi f \nu / u^*{}^2$ to be equal to 0.0025, which, according to the literature pertaining to turbulent pulsating flows, corresponds to a regime whereby turbulence time scales are much smaller than the period, $1/f$, of the oscillations [27]. In terms of particle mass transport, it was hypothesized that this condition might be favorable to diminish particle depositions with respect to a steady flow condition. This because the high shear associated with the acceleration phase of an oscillation has the time to develop into enhanced

Table 2.2 Provides a summary of all experimental conditions for filtration tests. The columns indicate: the Reynolds number, $Re = Uh/\nu$, the pressure, p , the suction coefficient, $\Gamma = V/U$ and the non-dimensional frequency, $\omega^+ = 2\pi f\nu/u_*^2$.

Test Name	Symbol	Re [-]	p [bar]	Γ [$\times 10^{-4}$]	ω^+ [-]
S-4_1	●	4005	1.00	1.37	-
S-4_1r	◆	4013	1.00	1.38	-
S-4_1.5	■	3983	1.52	1.63	-
P-4_1.5_2.5	▼	3974	1.51	1.84	0.0025

turbulence (i.e., enhanced mixing) before it is damped by the decelerating phase. This “high-intensity” turbulent bursts should, in principle, increase the probability of particles to be entrained in the feed rather than depositing over the membrane surface. A summary of experimental conditions is given in Table 2.2.

In order to obtain a significant and measurable drop in the filtration rate over time, each test was carried out for a duration of 23 h. During all the filtration tests, the surface of the membrane was monitored by a series of photographs taken at 15 min intervals using a camera (Canon EOS 700) controlled by digiCamControl software. The camera was carefully mounted horizontally (i.e., parallel to the membrane) and was placed above the test section at a sufficient distance to capture its entire extent. A dark room was built around this portion of the system and 11 spotlights of 600 LM each were placed inside it in a fixed position to ensure uniform and constant light during the tests. An initial white balance was carried out for all the images and then the variation of the yellow band (which is the dominant one in the measured spectrum) was calculated with respect to the initial value of the corresponding area, providing the % of color variation in time at different locations over the membrane. This system allows to monitor the chromatic change of the membrane surface induced by colloidal fouling in time and, even more interestingly, in space to check for particle deposition uniformity over the entire cell unit.

2.5 Results

This section is split in two parts. Sections 2.5.1 and 2.5.2 provide results obtained from the fluid dynamic and filtration tests, respectively.

2.5.1 Fluid Dynamic Tests

This section contains the experimental results of the fluid dynamic tests carried out in the three different longitudinal positions within the test section, whose parameters are reported in Table 2.1. Figure 2.3a shows the mean flow field, superimposed to a PIV snapshot and the contour plot of the longitudinal velocity obtained from the time averaging of 2000 flow resolutions, obtained from PIV in the F-1 test.

The contour plot shows quite uniform flow conditions, thus indicating that the laser was positioned correctly and parallel to the flow. This gives confidence about measurements quality when assessing the standard “family portrait” of velocity statistics profiles reported in the other panels of the figure. These were obtained by further averaging flow properties obtained locally (i.e., for each PIV interrogation areas) over lines parallel to the wall to achieve enhanced statistical robustness. The vertical coordinate and the velocity statistics profiles presented in panels (b-f) of Figure 2.3 are plotted following a conventional normalization, employing the channel half-height, h , the maximum speed, U_m , and the friction velocity, $u^* = \sqrt{\tau_0/\rho}$ (τ_0 is the wall shear stress and ρ is the water density). As is common in turbulent channel flows, τ_0 was estimated, for each of the three cases, from the linear extrapolation to the bottom wall of the total shear stresses, τ , defined as $\tau(y) = \rho\nu\frac{d\bar{u}}{dy} - \rho\overline{u'v'}$, where ν is the kinematic viscosity, u is the longitudinal velocity component, u' and v' are the longitudinal and vertical velocity (time) fluctuations, respectively, and overbar denotes time-averaging [28]. Results from the extrapolation are reported in Figure 2.3b, which shows how profiles of τ as obtained from PIV measurements are reasonably linear as expected in uniform turbulent channel flows.

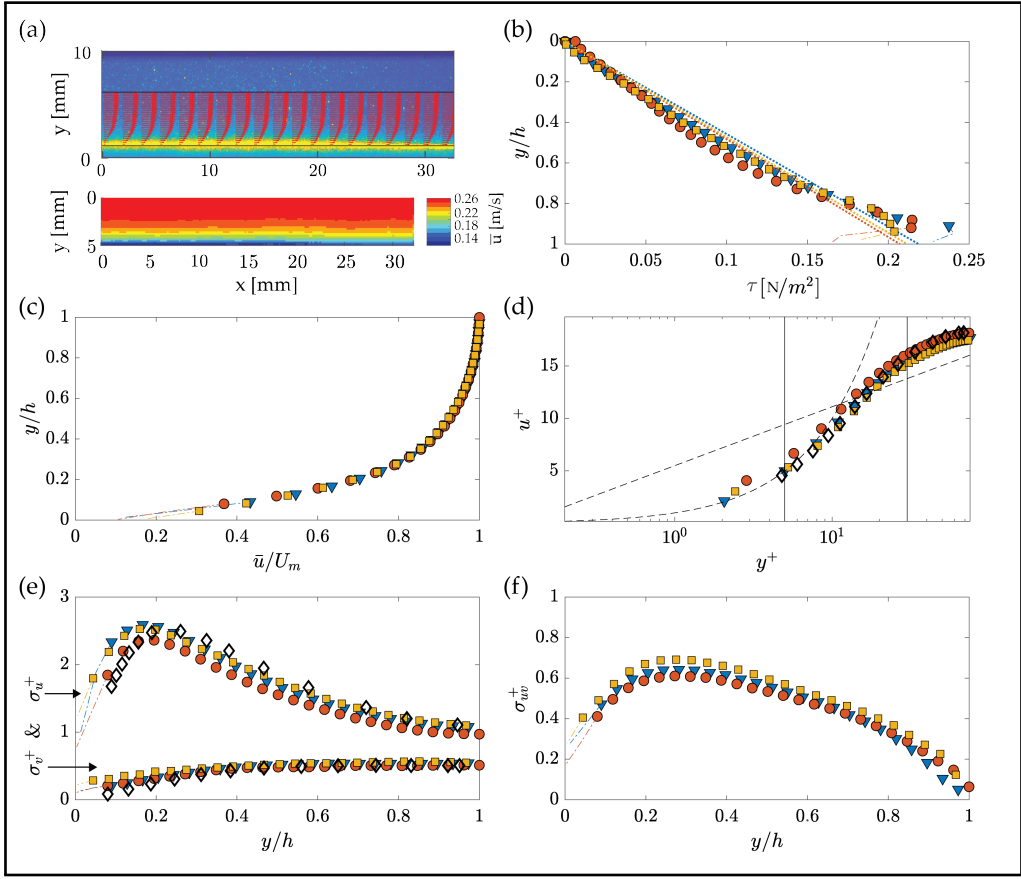


Fig. 2.3 Velocity statistics obtained from PIV measurements in the lower half of the test section for three different streamwise positions; h is the channel semi-height, $u^+ = \bar{u} / u^*$ is the normalized velocity; $y^+ = y u^* / \nu$ is the normalized distance from the wall, U_m is the maximum speed, $\sigma_v^+ = \sqrt{v'^2} / u^*$ and $\sigma_u^+ = \sqrt{u'^2} / u^*$ are the non-dimensional root squares of the variance for wall-normal and longitudinal velocity fluctuations, respectively, and $\sigma_{uv}^+ = \sqrt{v'u'} / u^*$ is the non-dimensional root square of the covariance. (a) Flow field and contour plot for test F-1; (b) total shear stress for all tests; (c) non-dimensional mean-velocity profiles (outer scaling); (d) non-dimensional mean-velocity profiles (inner scaling), the dashed line represent the linear law $u^+ = y^+$, characterizing wall flows for $y^+ \lesssim 5$; (e,f) non-dimensional profiles of velocity variances. Symbols and experimental conditions for all the tests are reported in Table 2.1, with the exception for \diamond that refers to the data from the DNS by Tsukara [29].

Figure 2.3c-f demonstrate that all the measured vertical profiles of mean velocities (panels (c) and (d)) and velocity variance (panel (e)) and covariance (panel (f)) collapse well, thus indicating the flow to be similar. Moreover, since all

the scaling parameters used in Figure 2.3 are reasonably constant for each test (i.e., at each different longitudinal coordinate) the flow can be considered uniform and hence fully developed. Further support about the quality of the data comes from the comparison with the direct numerical simulations of Tsukara et al. [29], performed at similar Re^* , whose data collapse very well with those presented herein, thus further demonstrating that the flows conform to canonical, turbulent channel flows, as sought. Further evidence for the occurrence of fully developed turbulence (and not transitional behavior) can be found in the Supplementary Information where, for both velocity fluctuations u' (longitudinal) and v' (wall-normal), a time series at a fixed point in space (Figure A.1) and a contour plot within the measurement window (Figure A.2) are presented. Both figures show that the flow presents a chaotic and irregular continuous pattern without the occurrence of intermittent laminar vs. turbulent behavior that is typically encountered in transitional conditions.

2.5.2 Filtration Tests

Figure 2.4 provides results of test S-4_1.5, which was conducted at steady flow conditions and an applied pressure of 1.5 bar.

The filtrate corresponding to each third of the membrane area, identified as “up”, “mid” and “down”, along the longitudinal direction of motion, is conveyed into the respective collection tray, which is then automatically emptied when a predefined value is reached (Figure 2.4a). The integral of these values, for each of the three areas, gives the respective cumulate from used to derive the flux associated with the test, as illustrated by Figure 2.4b. Since the global slope of the curves related to each section is almost the same, it is possible to infer that there is no evident longitudinal spatial variation in the filtrate flux. Note that in the filtration tests, part of the discharge is progressively lost along the direction of motion through the membrane (in our case a value between 1.9 and 2.5%), hence a slight non-uniformity of flow conditions should be expected. Our results indicate that such a slight non-uniformity has a negligible effect on the bulk flux of filtrate, which is essentially the same for the up, mid and down sections.

More spatially resolved information about the uniformity of the fouling rate is provided by the analysis of the photographs taken with the overhead camera, which is presented in figure Figure 2.5 for one experimental condition (the other tests showed a similar behavior as can be seen from Figure A.3 of the Appendix A).

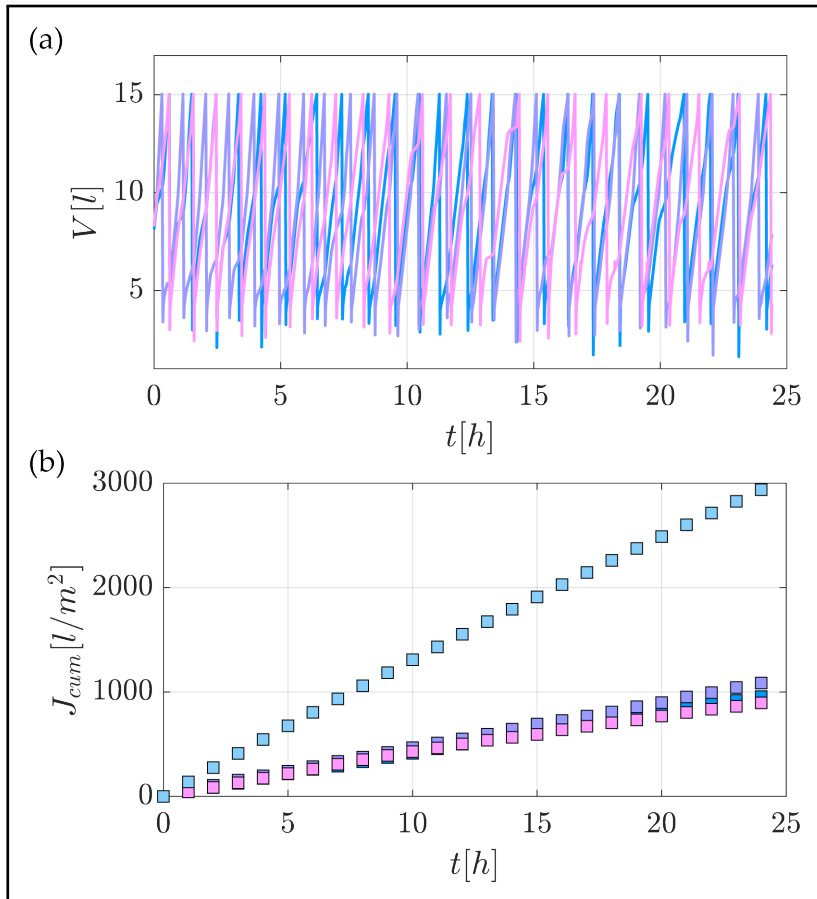


Fig. 2.4 Results of S-4_1.5 filtration test with a feed pressure of 1.5 bar; (a) fill levels of the three filtrate collection tanks vs. time; (b) total water flux and flux measured from the individual portions. In both panels, light blu, lavender and pink lines/symbols refer to, up, mid and down collection tanks, respectively (see Figure 3.3). Azure squares in panel (b) refer to the cumulative flux.

Here, panel (a) reports examples of the images taken over different time steps (note that full optical access to the surface of the membrane is prevented due to the

presence of braces that were used to avoid water leakage), while panel (b) shows the variation in yellow band color as detected by the camera over the 11 boxes highlighted in red in panel (a).

Panel (b) indicates that differences in yellow band variations (and hence the fouling rate) are minimal over the entire length of the channel at any point in time (differences between the upstream and downstream section are contained within 2 and 8.5%). Hence, it can be safely stated that fouling rates can be considered almost uniform across the membrane surface, as evidenced by the slight differences in filtrate flux measurements between the various longitudinal portions of the membrane. These results are important from an experimental point of view for mainly two reasons. Firstly, they demonstrate that the fouling rates measured within the facility can be directly associated with quasi-uniform and hence well-definable flow conditions, hence paving the way to establish clear cause–effect relations between flow and mass-transfer processes. Secondly, thanks to uniformity, measurements performed by means of conventional flow/particle-measurement devices, which are local (or quasi-local as per PIV) in nature, can be considered representative of the whole system and hence directly relatable to integral quantities such as filtrate fluxes, without the need of lengthy and costly flow characterization over the entire unit. Figure 2.5b also provides some insights about the fouling behavior over time, which is clearly non-linear, as expected [30]. Indeed, variations in the yellow-band color were faster at the beginning of the experiment and slower towards the end. This observation is consistent with the data presented in Figure 2.6, representing the behavior in terms of filtrate fluxes vs. time (it should be noted that the initial flux rate is consistent with the values of permeance indicated by the manufacturer), which, as expected, displayed a faster drop during the initial part of the experiment and a slower reduction towards the end.

Initially, at higher flux value, colloidal deposition is faster and particles interacted with the membrane surface, possibly causing direct pore clogging, thus resulting in a higher flux reduction rate. Later during the tests, particle deposition slowed down due to a reduction in permeate flux (i.e., reduction in convective flow toward the membrane surface) and particles started depositing on a layer of

pre-deposited particles, thus increasing the resistance of the cake layer but causing less direct pore clogging.

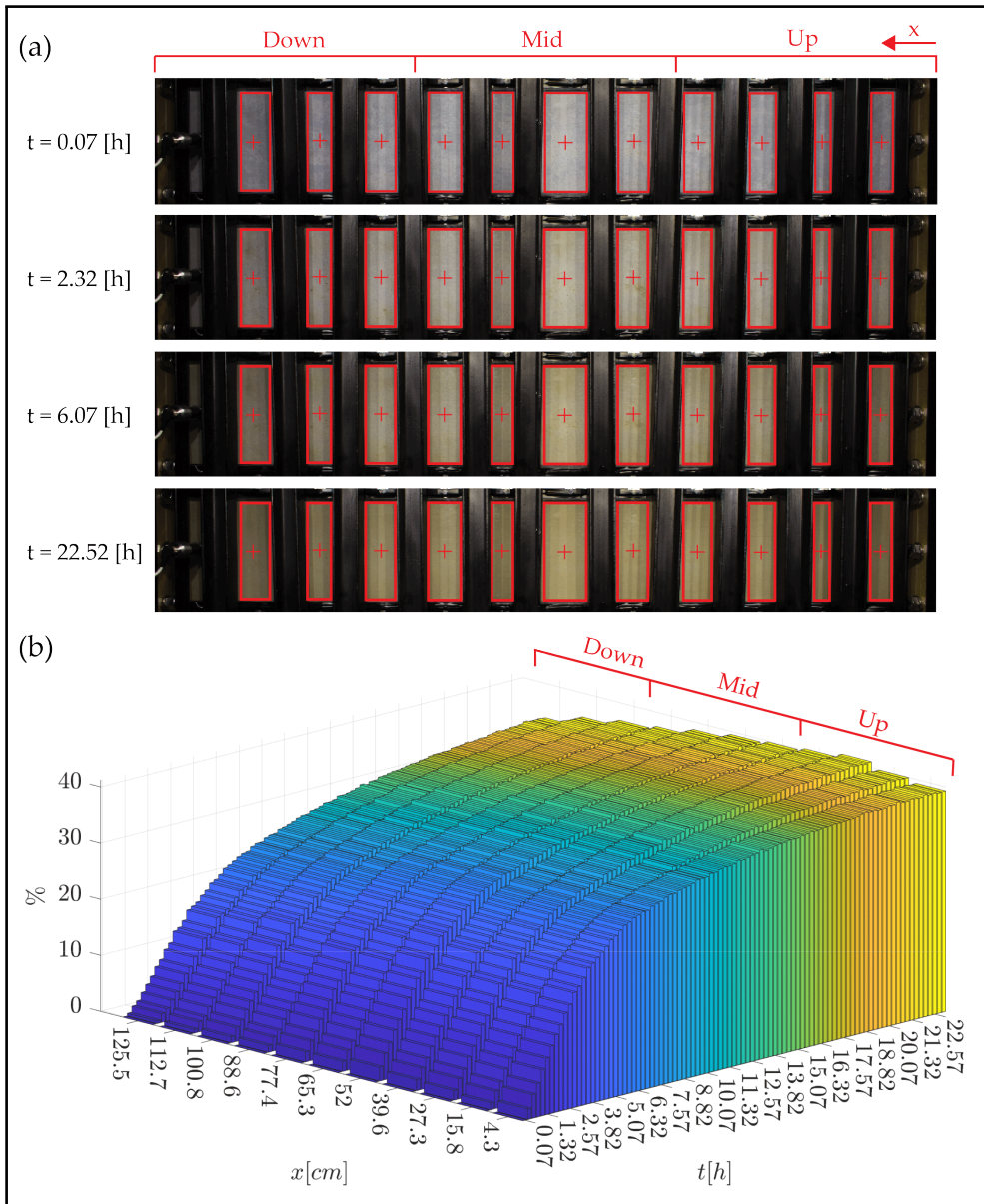


Fig. 2.5 Data related to colloidal fouling of the membrane. (a) Photographs from the overhead camera taken over the entire span of the test section and at different times, t (test S-4_1.5); (b) percentage variation of the membrane color (yellow band) measured at different longitudinal positions along the membrane surface (i.e., in each of the red boxes highlighted in panel (a) as a function of time).

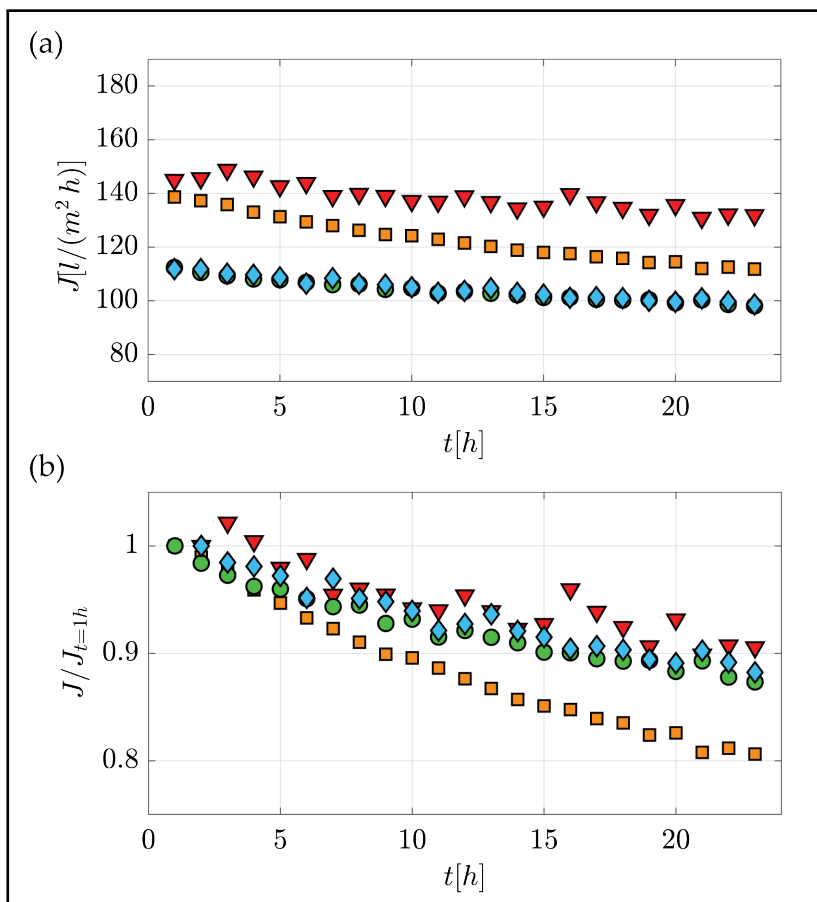


Fig. 2.6 Dimensional (panel (a)) and non-dimensional (panel (b)) filtrate fluxes vs. time for all experimental conditions (symbols as indicated in Table 2.2). In Panel (b), filtrate fluxes are normalized by their initial value.

More consistently with the objectives of the present study, Figure 2.6 provides evidence for the following important points:

- (i) Filtration tests carried out in the channel facility are controllable and repeatable because tests carried out at essentially identical experimental conditions display overlapping curves of filtrate vs. time (blue and green symbols).
- (ii) The pulsed flow case (red triangles, see Table 2.2) provided much improved filtrate flux behavior over time when compared to its steady flow counterpart (orange squares), as hypothesized in Section 2.2. Note that flux differences

are much greater than those associated with experimental uncertainty, as supported by the previous point about experimental repeatability. Specifically, flux values were maintained always larger than $130 \text{ l/m}^2/\text{h}$ in the pulsed flow case and a final normalized flux of 0.9 was achieved, thus halving the fouling-related flux reduction compared to the steady flow case. This observation suggests the potential of hydrodynamic methods to reduce colloidal fouling in ultrafiltration membrane systems.

2.6 Concluding Remarks

In this work, we presented and validated a new module-scale lab facility designed to investigate interlinks between hydrodynamics and fouling in membrane flow systems. The facility is rather innovative as it allows for the development of turbulent flow conditions (often encountered in membrane systems) at an unprecedented quality and controllability at least when compared to past studies pertaining to the membrane science literature [31, 32]. In this respect, PIV measurements indicated that fully developed turbulent channel flows were generated within the test section. These can also be considered canonical, in the sense that their velocity statistics compared very well with datasets presented in the literature and normally used as benchmark for quality check. Regarding filtration tests, these were carried out with waters containing a prescribed level of suspended colloids (clay) mimicking conditions of interest for the ultrafiltration of relevant surface waters. Results showed that tests were repeatable and displayed filtrate flux vs. time curves in agreement with those previously reported in the relevant literature. Despite the inherent (but slight) flow non-uniformity characterizing the filtration tests, fouling proved to occur rather uniformly along the whole unit. This was demonstrated from the measurements of filtrate fluxes at three different longitudinal sections of the unit, which proved to be nicely uniform and from the measurements of membrane color variations (as observed by means of an overhead camera and indicative of fouling), which also proved to be uniform. Finally, a pulsed flow test carried out by imposing pressure (and flow rate) variations at a dimensionless frequency, ω^+ of 0.0025, showed a significant reduction in colloidal fouling when compared to its steady counterpart, thus providing encouraging, albeit preliminary, results about pulsations as a viable hydrodynamic technique to reduce fouling in membrane systems. In this regard, ongoing work is focused to identify which pulsed-flow conditions, in terms of non-dimensional frequency and wave amplitudes, result in maximum fouling reductions within the context of applications in the water industry.

References

- [1] U. Water, “The united nations world water development report 2021: Valuing water,” 2021.
- [2] K. Zotalis, E. G. Dialynas, N. Mamassis, and A. N. Angelakis, “Desalination technologies: Hellenic experience,” *Water*, vol. 6, no. 5, pp. 1134–1150, 2014.
- [3] U. Caldera, D. Bogdanov, and C. Breyer, “Local cost of seawater ro desalination based on solar pv and wind energy: A global estimate,” *Desalination*, vol. 385, pp. 207–216, 2016.
- [4] B. Van der Bruggen, G. Cornelis, C. Vandecasteele, and I. Devreese, “Fouling of nanofiltration and ultrafiltration membranes applied for wastewater regeneration in the textile industry,” *Desalination*, vol. 175, no. 1, pp. 111–119, 2005.
- [5] S. Allen, D. Holena, M. McCunn, B. Kohl, and B. Sarani, “A review of the fundamental principles and evidence base in the use of extracorporeal membrane oxygenation (ecmo) in critically ill adult patients,” *Journal of intensive care medicine*, vol. 26, no. 1, pp. 13–26, 2011.
- [6] G. Daufin, J.-P. Escudier, H. Carrère, S. Bérot, L. Fillaudeau, and M. Decloux, “Recent and emerging applications of membrane processes in the food and dairy industry,” *Food and Bioproducts Processing*, vol. 79, no. 2, pp. 89–102, 2001.
- [7] S. Al Aani, T. N. Mustafa, and N. Hilal, “Ultrafiltration membranes for wastewater and water process engineering: A comprehensive statistical review over

- the past decade,” *Journal of Water Process Engineering*, vol. 35, p. 101241, 2020.
- [8] F. Wang, M. He, K. Gao, Y. Su, R. Zhang, Y. Liu, J. Shen, Z. Jiang, and R. Kasher, “Constructing membrane surface with synergistic passive antifouling and active antibacterial strategies through organic-inorganic composite modifier,” *Journal of Membrane Science*, vol. 576, pp. 150–160, 2019.
- [9] X. Lu, L. H. Arias Chavez, S. Romero-Vargas Castrillon, J. Ma, and M. Elimlech, “Influence of active layer and support layer surface structures on organic fouling propensity of thin-film composite forward osmosis membranes,” *Environmental science & technology*, vol. 49, no. 3, pp. 1436–1444, 2015.
- [10] M. Y. Jaffrin, “Hydrodynamic techniques to enhance membrane filtration,” *Annual Review of Fluid Mechanics*, vol. 44, pp. 77–96, 2012.
- [11] B. Gupta, P. Blanpain, and M. Jaffrin, “Permeate flux enhancement by pressure and flow pulsations in microfiltration with mineral membranes,” *Journal of membrane science*, vol. 70, no. 2-3, pp. 257–266, 1992.
- [12] J. Howell, R. Field, and D. Wu, “Yeast cell microfiltration: flux enhancement in baffled and pulsatile flow systems,” *Journal of Membrane Science*, vol. 80, no. 1, pp. 59–71, 1993.
- [13] M. Al-haj Ali, A. Ajbar, E. Ali, and K. Alhumaizi, “Optimization-based periodic forcing of ro desalination process for improved performance,” *Desalination and Water Treatment*, vol. 51, no. 37-39, pp. 6961–6969, 2013.
- [14] P. Saremirad, H. Gomaa, and J. Zhu, “Effect of flow oscillations on mass transfer in electro dialysis with bipolar membrane,” *Journal of membrane science*, vol. 405, pp. 158–166, 2012.
- [15] R. Vinuesa, A. Noorani, A. Lozano-Durán, G. K. E. Khoury, P. Schlatter, P. F. Fischer, and H. M. Nagib, “Aspect ratio effects in turbulent duct flows studied through direct numerical simulation,” *Journal of Turbulence*, vol. 15, no. 10, pp. 677–706, 2014.

-
- [16] Y. Çengel and J. Cimbala, *Fluid Mechanics: Fundamentals and Applications*. McGraw-Hill Education, 2018.
- [17] M. Ferro, *Experimental study on turbulent boundary-layer flows with wall transpiration*. PhD thesis, KTH Royal Institute of Technology, 2017.
- [18] U. Piomelli, E. Balaras, and A. Pascarelli, “Turbulent structures in accelerating boundary layers,” *Journal of Turbulence*, vol. 1, no. 1, p. 001, 2000.
- [19] D. S. Finnicum and T. J. Hanratty, “Effect of favorable pressure gradients on turbulent boundary layers,” *AIChE journal*, vol. 34, no. 4, pp. 529–540, 1988.
- [20] W. T. Eckert, K. W. Mort, and J. Jope, “Aerodynamic design guidelines and computer program for estimation of subsonic wind tunnel performance,” 1976.
- [21] I. Nedyalkov, “Design of contraction, test section, and diffuser for a high-speed water tunnel,” Master’s thesis, 2012.
- [22] B. Ramaprian and S.-W. Tu, “An experimental study of oscillatory pipe flow at transitional reynolds numbers,” *Journal of Fluid Mechanics*, vol. 100, no. 3, pp. 513–544, 1980.
- [23] K.-H. Ahn, H.-Y. Cha, I.-T. Yeom, and K.-G. Song, “Application of nanofiltration for recycling of paper regeneration wastewater and characterization of filtration resistance,” *Desalination*, vol. 119, no. 1-3, pp. 169–176, 1998.
- [24] J. Nikolova and M. Islam, “Contribution of adsorbed layer resistance to the flux-decline in an ultrafiltration process,” *Journal of Membrane Science*, vol. 146, no. 1, pp. 105–111, 1998.
- [25] V. Davide, M. Pardos, J. Diserens, G. Ugazio, R. Thomas, and J. Dominik, “Characterisation of bed sediments and suspension of the river po (italy) during normal and high flow conditions,” *Water research*, vol. 37, no. 12, pp. 2847–2864, 2003.

- [26] Arpa Piemonte, “Water quality in Torino (2009-2017).” http://webgis.arpa.piemonte.it/monitoraggio_qualita_acque/index.php?numcodice=001095, 2020. [Online; accessed 22-November-2021].
- [27] S. He and J. Jackson, “An experimental study of pulsating turbulent flow in a pipe,” *European Journal of Mechanics-B/Fluids*, vol. 28, no. 2, pp. 309–320, 2009.
- [28] C. Peruzzi, D. Poggi, L. Ridolfi, and C. Manes, “On the scaling of large-scale structures in smooth-bed turbulent open-channel flows,” *Journal of Fluid Mechanics*, vol. 889, 2020.
- [29] T. Tsukahara, Y. Seki, H. Kawamura, and D. Tochio, “Dns of turbulent channel flow at very low reynolds numbers,” in *Fourth International Symposium on Turbulence and Shear Flow Phenomena*, Begel House Inc., 2005.
- [30] C. Y. Tang, T. Chong, and A. G. Fane, “Colloidal interactions and fouling of nf and ro membranes: a review,” *Advances in colloid and interface science*, vol. 164, no. 1-2, pp. 126–143, 2011.
- [31] A. Kastl, E. Bar-Zeev, M. Spinnler, and T. Sattelmayer, “Impact of pulsating flows on particle deposition in forward osmosis with spacers,” *Journal of Membrane Science*, vol. 635, p. 119444, 2021.
- [32] A. Bogler, A. Kastl, M. Spinnler, T. Sattelmayer, A. Be’er, and E. Bar-Zeev, “Where, when and why? quantifying the relation of particle deposition to crossflow velocity and permeate water flux in forward osmosis,” *Journal of Membrane Science*, vol. 604, p. 118055, 2020.

Chapter 3

Suction effects on turbulence in channel flows at low Reynolds numbers

3.1 Abstract

This paper presents an experimental investigation dedicated to the study of wall suction effects on turbulence properties of channel flows at low Reynolds numbers. Suction was created by using thin membranes to establish a permeate flux along the bed-normal direction. By varying the membrane permeability and the bulk pressure in the channel, it was possible to generate different suction rates (without relaminarisation of the boundary layer), while keeping the Reynolds number constant throughout all the experiments. Longitudinal and bed-normal velocities were measured in a central cross-section of the channel by means of Particle Image Velocimetry (PIV) and Laser Doppler Anemometry (LDA). Results are presented as a comparative analysis between velocity statistics obtained in suction-wall flows and a canonical flow (i.e. with smooth impermeable boundaries) that was used as a benchmark. Comparison of velocity variances and covariances indicate that wall-suction tends to suppress turbulence. Interestingly, though, such suppression is independent of the suction rate despite variations of this parameter of more than one order of magnitude. Quadrant analysis reveals that suction tends to slightly alter sweeps and ejections as these become more frequent but less intense. The comparison between cross-correlation functions and 1-D spectra reveals no significant differences between the benchmark and suction-wall flows. However, 1-D spectra revealed an interesting flow feature. When plotted in premultiplied form, 1-D spectra of the longitudinal velocity component are characterised by a pronounced peak at very low wavenumbers, which is usually associated with the occurrence of Very Large Scale Motions (VLSM) in wall flows. Given the very low Reynolds number of the experiments this was rather unexpected. Indeed, it is herein demonstrated that this peak is not associated with VLSM but seems to be related to a laminar-to-transition phenomenon as it disappears as soon as the Reynolds number is raised. It was also observed that suction tends to make this peak more evident with respect to the benchmark case at an identical Reynolds number hence supporting the idea that suction tends to stabilise the flow and delay the transition to a fully developed turbulent regime.

3.2 Introduction

Turbulent wall flows with suction have been traditionally studied by aerodynamicists as they are an effective means to avoid boundary layer separation around airfoils. Most of the experimental studies dedicated to the investigation of this class of flows involved wind tunnel tests whereby turbulent boundary layers developed over perforated plates connected to a vacuum system to create suction [1–6]. Numerical investigations based on Large Eddy Simulations (LES) and Direct Numerical Simulations (DNS) are also available [7–9] for turbulent channel flows and flat plate boundary layers. Considering the case of distributed suction (i.e. not the case of a localised suction generated by a short slit as per airfoil applications) the main results from the available literature can be summarised as follows.

Most studies quantify the intensity of suction with the so-called suction rate parameter defined as $\Gamma = V/U$ where V is the characteristic velocity associated with transpiration (say, the volume flow rate that is extracted from the perforated plate divided by its surface area) and U is a characteristic outer layer velocity, e.g. U_∞ in flat plate turbulent boundary layers. If Γ is above a critical parameter Γ_{SST} (usually of about $3\text{--}4 \times 10^{-3}$) turbulence is totally suppressed and the flow is laminarised. For $\Gamma < \Gamma_{SST}$, flow does not undergo laminarisation and turbulence remains self-sustained. Recent investigations confirm that, for $\Gamma < \Gamma_{SST}$ and long distances from the beginning of the perforated plate, turbulent boundary layers reach a streamwise invariant condition, whereby boundary layer growth is suppressed in response to an equilibrium between the momentum loss at the wall and entrainment of high momentum fluid due to suction [1]. Ferro demonstrated that TASBLs are characterised by mean velocity profiles that scale very well in outer coordinates (i.e. using U_∞ and boundary layer thickness δ as scaling parameters) regardless of Γ , while Bobke et al. [8] argue that it is more appropriate to use a classical log law of the wall (in inner scaling) where Von Karman and intercept constants are Γ -dependent.

Regarding other velocity statistics, there is a general agreement in the literature on the fact that normal and shear Reynolds stresses are significantly damped by suction over the entire height of the boundary layer. Moreover, it is argued that

normal Reynolds stress responds differently, with the vertical-velocity variance being more affected than its horizontal counterparts. Antonia et al. [10] argued that this turbulence damping and its associated anisotropy are caused by a phenomenon which can be described as a stabilisation of near-wall streaks, which in turn leads to a less intense near-wall burst cycle.

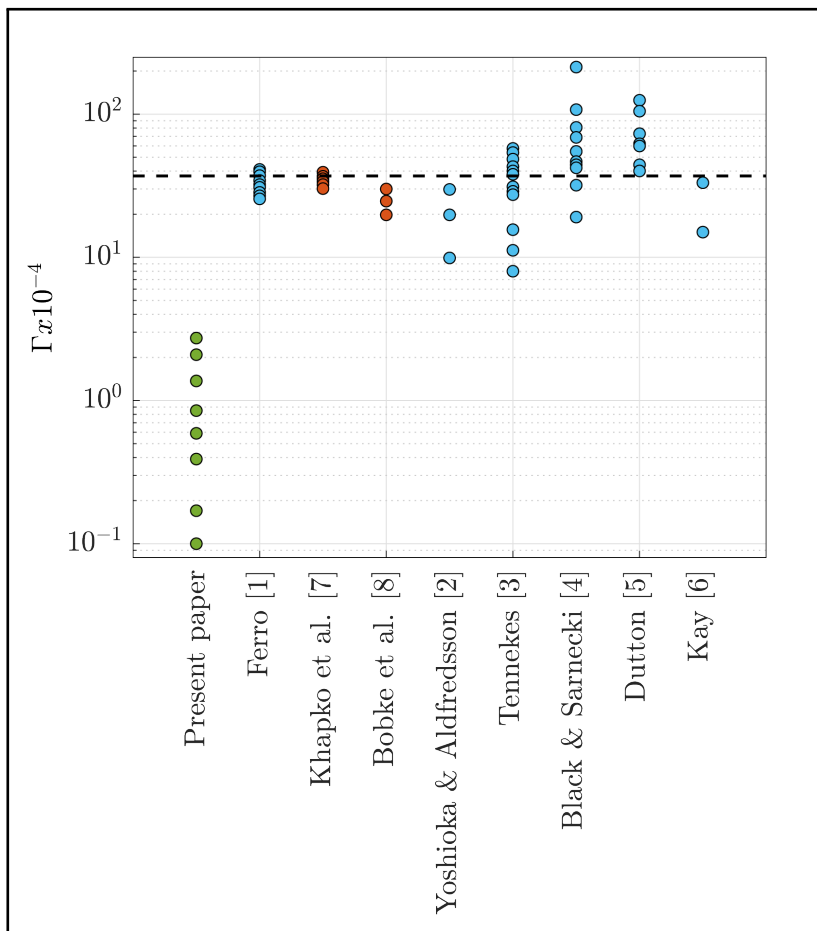


Fig. 3.1 Suction rates: All the points are calculated as $\Gamma = V/U_\infty$ (where V is the mean vertical velocity through the porous media and U_∞ is the free stream velocity) except for the present in which is calculated as $\Gamma = V/U_m$ (where U_m is the maximum velocity in the centre of the channel). Green dots come from membrane experiments, light blue dots refer to perforated plate experiments, and orange dots refer to DNS and LEN studies. The black dotted line indicate the value beyond which relaminarisation occur [7].

As far as the structure of turbulence is concerned, Ferro [1] and Bobke [8] point out that suction tends to suppress large-scale turbulence structures (i.e. structures that scale with the boundary layer thickness), while as conjectured by Antonia et al. [10], near-wall streaks become longer.

In general, the literature lacks of systematic investigations about the effects of suction on velocity statistics over a wide range of suction rates Γ . Figure 3.1 (readapted from Ferro [1]) shows that the only studies covering a good range of Γ are rather old (from the fifties and sixties) hence carried out with experimental equipment such as pitot tubes and hot wire anemometry that struggle to measure turbulence statistics of order greater than one (Antonia et al. [10]). In addition, much of the investigated values of Γ were beyond Γ_{SST} hence likely to be associated with boundary layers either fully laminarized or in the process of being relaminarized.

The present paper complements the existing literature with novel experiments designed to investigate turbulent channel flows with an unprecedented range of suction rates Γ covering more than one order of magnitude (see Figure 3.1), while keeping the bulk flow Reynolds number constant. Contrary to previous studies, though, such a Reynolds number was kept very low (i.e. just above transitional $Re = 4000$) as this is the typical value encountered in membrane systems, which represents the engineering application that drives and motivates the present study. In a nutshell, membrane systems involve turbulent flows bounded by an impermeable and a porous wall, the latter made by a membrane which is a thin fibrous filter usually made of polymeric material that works to retain particles and molecules and hence to separate the feed (namely the dirty fluid) from the permeate (the purified fluid). Membrane systems often work in "cross flows", namely very similarly to suction wall flows where the permeate represents the vertical mass flux associated with suction (see Figure 3.2) and the feed the overlying flow. Clearly, the permeate must be driven by a pressure difference between the fluid in the feed and the outside region. In these systems, the flow of the feed is usually kept turbulent to maximise mixing and avoid as much as possible membrane clogging (namely, the trapping of particles and molecules

on the membrane surface), which is notoriously the biggest bottleneck in the application of these filtering techniques [11, 12].

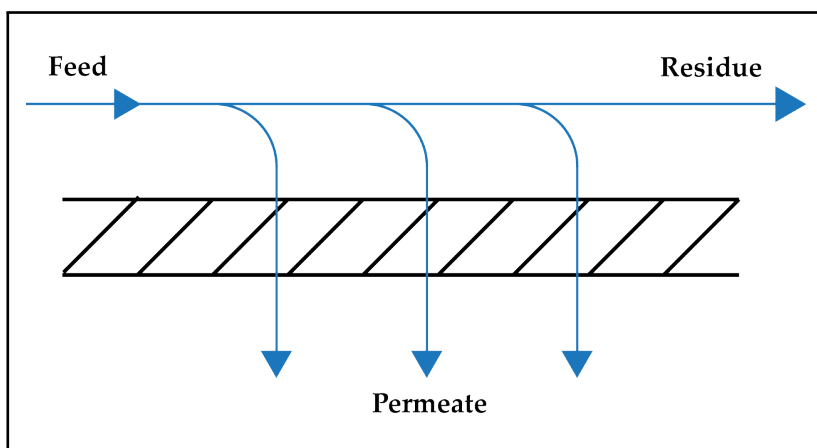


Fig. 3.2 Cross-flow scheme in a membrane module.

It is the author's opinion that groundbreaking advances in the field of clogging minimisation will be made only if the details of turbulence in membrane flow systems are fully understood, as these are the main drivers of the mass transfer processes occurring at the membrane-feed interface, which are responsible for the clogging itself. To the best of the author's knowledge, the effects of permeate flux (i.e. suction rates) on the properties of turbulence in the feed flow have never been investigated from a fluid mechanics perspective, hence the present paper intends to contribute to bridging this knowledge gap.

The chapter is organised as follows: Section 3.3 describes the hydraulic facility where all the tests were conducted; Section 3.4 presents the equipment used for data acquisition, such as Particle Image Velocimetry (PIV) and Laser Doppler Anemometry (LDA) and the related experimental procedure; Section 3.5 presents experimental data validation and discussion of results and Section 3.6 is devoted to conclusions.

3.3 Experimental Methods

This section briefly describes the experimental facility used for the experiments. The interested reader may refer to a previous article [13] for more detailed information about components, design and working principles

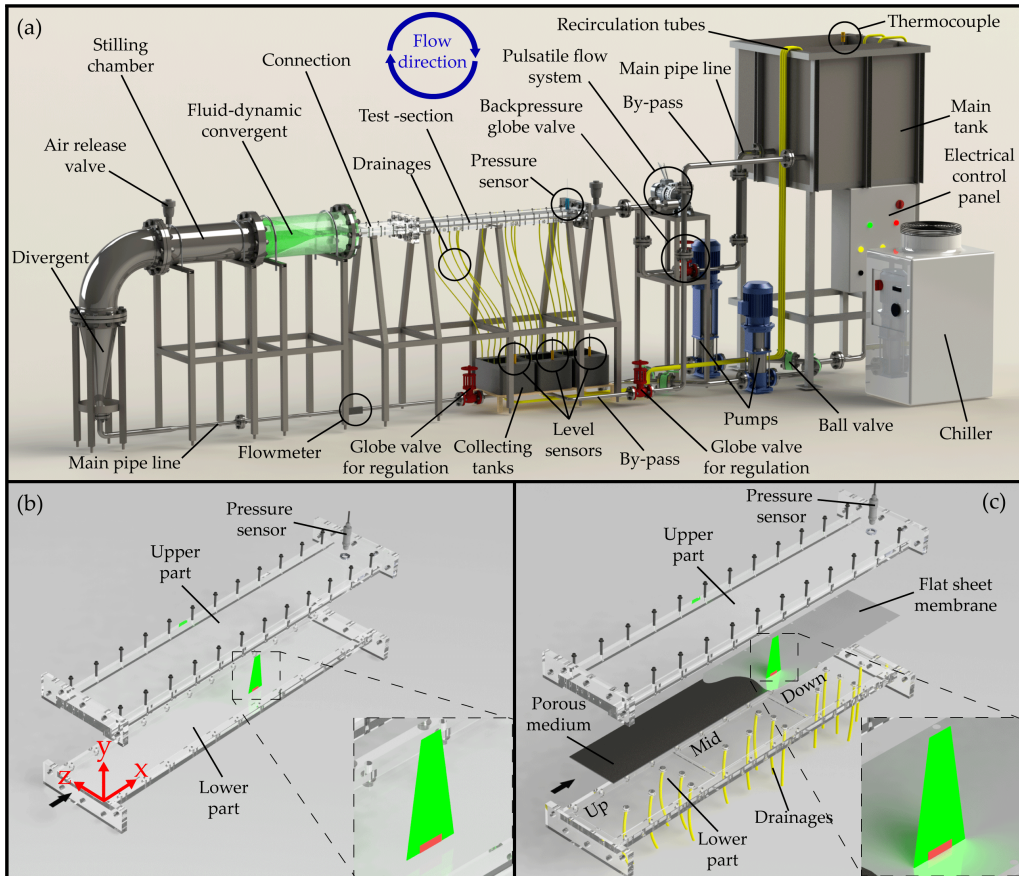


Fig. 3.3 Overview of the proposed setup: (a) Rendering of the entire hydraulic facility; (b) Sketch of test section; (c) Sketch of the test section used for filtration tests where a thin flat sheet membrane leans on top of a high permeability stainless steel porous medium used simply as mechanical support. Panel (b) also shows the reference system used in the present study, the origin is chosen at the right-bottom entrance of the test section and x , y , z coordinates correspond to streamwise, wall-normal and spanwise directions, respectively.

The facility is composed of a recirculating hydraulic circuit driven by two pumps and a series of pipes and conduits made mostly of stainless steel (see Figure

3.3a). The feed solution is drawn from a 1 m³ tank by two in-parallel computer-controllable multi-stages pumps that, once combined, allow for the establishment of flow rates corresponding, within the test section, to Reynolds numbers within the range 1000÷20000 hence covering the full range of laminar, transitional and fully turbulent flows. Right downstream of the pumps one main pipeline conveys water through a divergent tube that gently connects to a conditioning unit made of a stilling chamber and contraction that was specifically designed to avoid boundary layer separation while imposing a favourable pressure gradient to help suppress background turbulence [14]. After the contraction, water is gently conveyed in the test section, which is a 0.01 m high, 0.2 m wide and 1.4 m long channel flow with transparent top and lateral walls that allows for velocity measurements using laser diagnostics. The pressure inside the facility is controlled by a "backpressure" valve located at the downstream end of the main pipeline and right upstream of the main tank where water is then recirculated.

Two types of experiments were carried out. The first experiment involved a channel flow with smooth, impermeable boundaries made of perspex (Figure 3.3b hereafter referred to as the benchmark test). The second set of tests (hereafter referred to as filtration tests) was carried out by replacing the impermeable bottom wall with thin sheet membranes leaning on top of a high permeability porous medium made of metallic foam, which was used simply as mechanical support (see Figure 3.3c). For filtration tests, underneath the metallic foam, three separate compartments made of perspex were arranged to collect the filtrate through five drainage pipes each, conveying the permeate into three collecting tanks located underneath the test section, where water level sensors were employed to monitor the flux rate. The collecting tanks were emptied by a bilge pump once the water reached a critical level and the water returned to the main tank. The use of the three compartments allowed us to monitor in time to what extent the filtration rate was uniform over the full length of the test section. Water temperature was kept constant by means of a 5 kW chiller unit to maintain fluid properties constant throughout the entire duration of the experiments.

In a previous paper, Bert et al. [13] demonstrated that, within the channel test section, turbulent flows at the same Reynolds number as those that will be

Table 3.1 Summary of the experimental conditions for benchmark and filtration tests. U is the bulk velocity in the channel; U_m is maximum velocity as obtained from PIV measurements; $Re = Uh/\nu$ is the Reynolds number where ν is the kinematic viscosity of water at the mean measured temperature T ; p is the gauge pressure measured within the test section; J is the amount of permeate observed for each experiment during velocity measurements; $\Gamma = V/U$ is the suction rate with V being a vertical velocity estimated as the flux divided by the membrane surface area; $\Delta_{x,y}$ is the pixel size in the images grabbed using the PIV system described in Section 3.4.1 and "Grid" identify the size (in pixels) of the interrogation area employed for the analysis of PIV images.

Experiment	Symbol	U [ms ⁻¹]	U_m [ms ⁻¹]	Re [-]	T [°C]	p [bar]	J [lm ⁻² h ⁻¹]	Γ [x10 ⁻⁴]	$\Delta_{x,y}$ [mm]	Grid [pix]
Benchmark	★	0.209	0.287	3981	20.8	-	-	-	0.012	16
BN 1	●	0.211	0.283	4010	19.7	0.15	10.5	0.14	0.0121	16
BN 2	▲	0.210	0.28	3990	19.7	0.25	17.6	0.23	0.0121	16
BN 3	✦	0.210	0.277	4002	19.8	0.50	38.7	0.51	0.0121	16
BN 4	▶	0.210	0.275	3998	19.9	0.75	58	0.77	0.0121	16
BN 5	■	0.210	0.272	4003	20	1.01	82.9	1.10	0.0121	16
LY 1	▲	0.211	0.263	4017	19.5	1.51	130	1.71	0.0109	16
LY 2	▼	0.210	0.259	4004	20.1	1.99	195.1	2.58	0.0109	16
LY 3	◆	0.209	0.253	3971	21	2.47	248.3	3.30	0.0109	16

herein investigated become well developed and uniform already at $x=0.35$ m from the inlet (see Figure 3.3b for the definition of the origin and axes of the chosen reference system). Taking a conservative approach, all velocity measurements were carried out further downstream at $x=0.82$ m.

Filtration tests were carried out by extensively varying the membrane permeability and channel pressure to investigate flows over a wide range Γ while maintaining a constant Reynolds number. In particular, two different Synder flat-sheet ultrafiltration membranes, namely BN and LY and a range of gauge pressure varying between 0.015 and 0.247, allowed to establish flows with Γ variations spanning more than one order of magnitude (see Table 3.1). The Reynolds number $Re = Uh/\nu$ (U is the bulk velocity, h is the semi-height of the channel, and ν is the kinematic viscosity) was set to 4000, which is a value that is representative of flows in membrane systems and hence of interest in the present paper as discussed in Section 3.2 .

3.4 Experimental Procedure and Measuring Equipment

This section presents the experimental procedure and the measuring equipment used to investigate flow characteristics pertaining to the benchmark and filtration tests and data validation. Velocity measurements were carried out mainly by means of Particle Image Velocimetry (PIV) (see Section 3.4.1), which were complemented by Laser Doppler Anemometry (LDA)(see Section 3.4.2) for spectral analysis. Section 3.4.3 is dedicated to data validation while 3.4.4 reports the assessment of flow non-uniformity within the PIV measurement domain.

3.4.1 PIV Measurements

Velocity measurements for all the experiments reported in Table 3.1 were carried out by means of a 2-D PIV Dantec Dynamic system, composed of a 12 mp IMPEREX c-4080 camera (sensor size 18.8x14.1 mm) equipped with a Nikon lens and a green 200 mJ double pulsed YAG laser with a wavelength of 532 nm. The laser beam, which can be shut at a maximum frequency of 15 Hz, is conveyed into a movable mechanical arm ending with an optical unit made of a cylindrical and spherical lens to allow for laser sheet generation and control in terms of focus and width. Both optical unit and camera were mounted on a modular aluminium profiles structure to obtain a very precise positioning control in terms of parallelism and alignment between the main flow direction, the 1-2 mm laser sheet and the camera. The latter was placed at 0.6 m from the laser sheet providing a magnification factor M of 2.5. The flow was seeded with hollow glass spheres (concentration 0.09 g/L) particles with a mean diameter of 7.97 μm and a standard deviation of 3.52 μm [15].

For each test, the laser sheet was placed at $x = 82.5$ cm, $y = 0.5$ cm and $z = 5$ cm (Figure 3.3b) and images were taken over a 35 x 5 mm flow domain (please note that 5 mm is the semi-height of the channel), where longitudinal and wall-normal velocity fields (hereafter referred to as u and v , respectively) were measured by applying an image cross-correlation algorithm between 1500 image

pairs grabbed at a frequency equal to 4 Hz. The time interval between the two consecutive images (and hence two laser pulses) was set as to correspond to the mean particle displacement of approximately 8-pixel particles and resulted equal to $\Delta_t = 465 \mu\text{s}$. A custom-built calibration plate was used to calibrate the images and compensate for any residual optical distortion caused by small misalignments between the camera, the laser and the main flow direction.

All the images were analysed by means of Dantec Dynamics 6.4 software which is based on a cross-correlation adaptive algorithm over interrogation areas of size 16 x 16 pixels (corresponding to approximately 0.19 x 0.19 mm). Each resulting velocity field was validated using the Peak Height Ratio [16] PIV Uncertainty algorithm. The data thus obtained were then exported and post-processed with the universal outliers detection method proposed by Westerweel and Scarano [17], and the spurious vectors were replaced accordingly to the mean value of the adjacent valid vectors. Matlab codes were then used to compute all the velocity statistics presented in the results section.

3.4.2 LDA Measurements

The PIV technique is unsuitable for spectral analysis, which is herein used to study the structure of turbulence in the investigated flows. Indeed, on the one hand, the size of the illuminated area is too small to capture the contribution of large-scale structures via 1-D spectra directly in the wavenumber domain. On the other hand, the temporal resolution of the velocity fields is far too coarse to obtain meaningful results in the frequency domain. To compensate for such limitations, Laser Doppler Anemometry (LDA) was employed as it allows for high-frequency point velocity measurements and ultimately for comprehensive spectral analysis in the frequency domain, which can then be transposed into the wavenumber domain using Taylor's hypothesis of frozen turbulence.

LDA is a non-intrusive, high-resolution method for which the absence of an initial calibration provides very accurate measurements over a wide range of flow velocity. Its working principle is very simple: a laser source generates two pairs of lasers beam that converge within a small volume creating two ellipsoidal

measuring points. If the flow is properly seeded, a tracer particle passing by will create a signal of alternating scattered light intensity, which is sensed by a photomultiplier and analysed to work out the doppler shift between the incident and scattered light. If the plane containing the two beams is appropriately aligned with a characteristic direction of the investigated flow, the doppler shift can be related to a specific velocity component performed to gain further information on turbulence structure through power spectra analysis.

In this work, we employed a two-dimensional Dantec Dynamics Flow Explorer DPSS system equipped with two YAG laser beams of maximum power equal to 300 mW with wavelengths 532 nm (green light) and 561 nm (yellow light). The former was split into two beams that were then aligned to measure the longitudinal velocity component, while the latter was split and aligned to measure the wall-normal velocity component. Note that, in this specific application, the vertical velocity component was not measured, though, as the small size of the channel did not allow for an undisturbed penetration of the associated laser beams.

The correct positioning and alignment of the LDA system were done using a computer-controlled traversing system (ISEL iMC-S8) which allows for a displacement sensitivity of 6 μm along with the three spatial directions. Furthermore, great attention was paid to making the bottom of the channel and the laser beams associated with the longitudinal velocity component parallel and placing the measurement volume in correspondence with the plane for which PIV campaigns were conducted. The signal analysis was carried out with a Dantec Dynamics Burst Spectrum Analyzers (BSA F600-2D) and a dedicated BSA flow Software v6.5.

Table 3.2 provides a summary of all the experiments carried out using LDA and shows that most of them were carried out for the benchmark case over a wide range of Re . This is because, as it will be explained later in the results section, the observed peculiar features of the large-scale turbulence in both the benchmark and filtration tests were mainly driven by Re -effects. Such features could be captured by simple measurements of the longitudinal velocity component conducted at $y = 5$ mm and hence in the mid-height of the channel.

For all the experiments, 5 grams of HGS-Dantec Dynamics seeding particles were added to the water. This allowed to enhance the acquisition frequency up to

300 Hz and minimise the occurrence of outliers in the measurements, which were detected and removed using a threshold method (all velocity fluctuations exceeding 3 times the standard deviation of the time series were deemed as outliers). For each run, 250000 velocity measurements were taken to obtain smooth spectra.

3.4.3 Data validation

Throughout this section and the remaining part of the paper, u and v are the longitudinal and wall-normal velocity components measured along with the x and y directions. The overbar and the prime index denote time-averaged fluctuations, respectively, so that $u = \bar{u} + u'$ and $v = \bar{v} + v'$.








Data validation is based on the comparison between the velocity statistics obtained for the benchmark test and those retrieved from the simulations by Tsukara et al. [18], who performed DNS at Reynolds number $Re_\tau = hu^*/\nu = 70$ (with u^* the friction velocity and ν the kinematic viscosity) which is similar to that used for the benchmark case, i.e. $Re_\tau = 74$.

Note that, within the context of the PIV measurements presented in this paper, all velocity statistics are estimated in two steps. First, they are assessed for each interrogation area using time averaging. Then they are spatially averaged along transects parallel to the wall for the entire width of the PIV measurement domain to increase their statistical robustness. This averaging is carried out assuming mean flow non-uniformities in the longitudinal direction are negligible. This is clearly ensured for the benchmark experiment, as this relates to a uniform channel flow configuration, while it should be highlighted that that invariance cannot be satisfied for the filtration tests due to the progressive loss of fluid mass caused by suction at the bottom wall. This issue will be addressed in Section 3.4.4.

Vertical profiles of mean velocities \bar{u} , standard deviations $\sqrt{v'^2}$ and $\sqrt{u'^2}$ and covariance $-\overline{u'v'}$, estimated as described above are reported in Figure 3.4¹, where the friction velocity $u^* = \sqrt{\tau_0/\rho}$ (τ_0 is the wall shear stress estimated from linear

¹Note that \bar{u} , $\sqrt{v'^2}$, $\sqrt{u'^2}$ and $-\overline{u'v'}$ should be complemented by a spatial averaging operator reflecting the transect-averaging described in the previous paragraph. This is herein omitted to avoid symbols' overcrowding in the next figures.

Table 3.2 Summary of the experimental conditions for LDA measurements. The columns indicate: the distance at which LDA measurements are taken (centre of the channel); the eddy-convection velocity that correspond to the local mean streamwise velocity U ; the Reynolds number $Re = Uh/\nu$; the mean temperature T ; the mean pressure p ; the amount of flux through the membrane; the suction rate $\Gamma = V/U$ and the number of samples acquired.

Experiment	Symbol	y/h [mm]	U [ms ⁻¹]	Re [-]	T [°C]	P [bar]	J [lm ⁻² h ⁻¹]	Γ [x10 ⁻⁴]	N° Data [-]
Smooth wall		1	0.158	3016	19.5	-	-	-	250000
Smooth wall		1	0.209	3987	20.1	-	-	-	250000
BN		1	0.209	3985	17.2	0.15	8.7	0.11	250000
Smooth wall		1	0.263	5013	19.5	-	-	-	250000
Smooth wall		1	0.313	5955	20.6	-	-	-	250000
Smooth wall		1	0.441	8398	19.9	-	-	-	250000
Smooth wall		1	0.631	12016	19.5	-	-	-	250000

interpolation to the bottom wall of the total shear stress $\tau = \tau_v + \tau_t$, estimated as the sum of the viscous $\tau_v = \rho \nu (d\bar{u}/dy)$ plus turbulent component $\tau_t = \rho (\overline{u'v'})$ is employed to provide the non-dimensional representation of the data in the usual outer and inner scaling.

Figure 3.4 shows that the agreement between the DNS of Tsukara et al. [18] and the present data is very good. Some (very) small deviations are observed in the near-wall region where velocity standard deviations do not perfectly match when plotted in outer coordinates (see Figure 3.4b). It is difficult to identify the cause of such a small mismatch as it can be related to experimental procedure issues (i.e. difficulties in aligning camera, laser sheet and flow) or scaling (uncertainty in the estimation of the friction velocity). However, as discussed in the following, the near-wall region is also where PIV data were affected by the highest measurement error, which is certainly another candidate to explain the observed mismatch.

In order to provide a more comprehensive assessment of data quality, an uncertainty analysis for all the conditions reported in Table 3.1 was also performed using the Peak Height Ratio method developed by Charonko & Vlachos [20]. This method indicates that the measurement error can be estimated from the ratio between the height of the primary and secondary peak detected by the PIV cross-correlation algorithm of image analysis. The non-dimensional measurement error for the longitudinal velocity component (the vertical component shows a similar trend) detected following [20] is reported in Figure 3.5 for the benchmark case and all filtration tests.

Figure 3.5 shows that in the region $0.2 < y/h < 1$, $\overline{E_u}/\bar{u}$ is very small and oscillate around 1% while an exponential increase occurs as the boundary approaches. A few comments can be made:

- (i) The perspex that made the bottom of the channel for the benchmark experiment and, even more, all the employed membranes are reflective surfaces that generate a high luminous disturbance that appears in the PIV images and partially inhibits particle tracking.
- (ii) Near these walls, higher gradients and low velocities coupled with a less homogeneous distribution of seeding close to surfaces worsen the sub-pixel

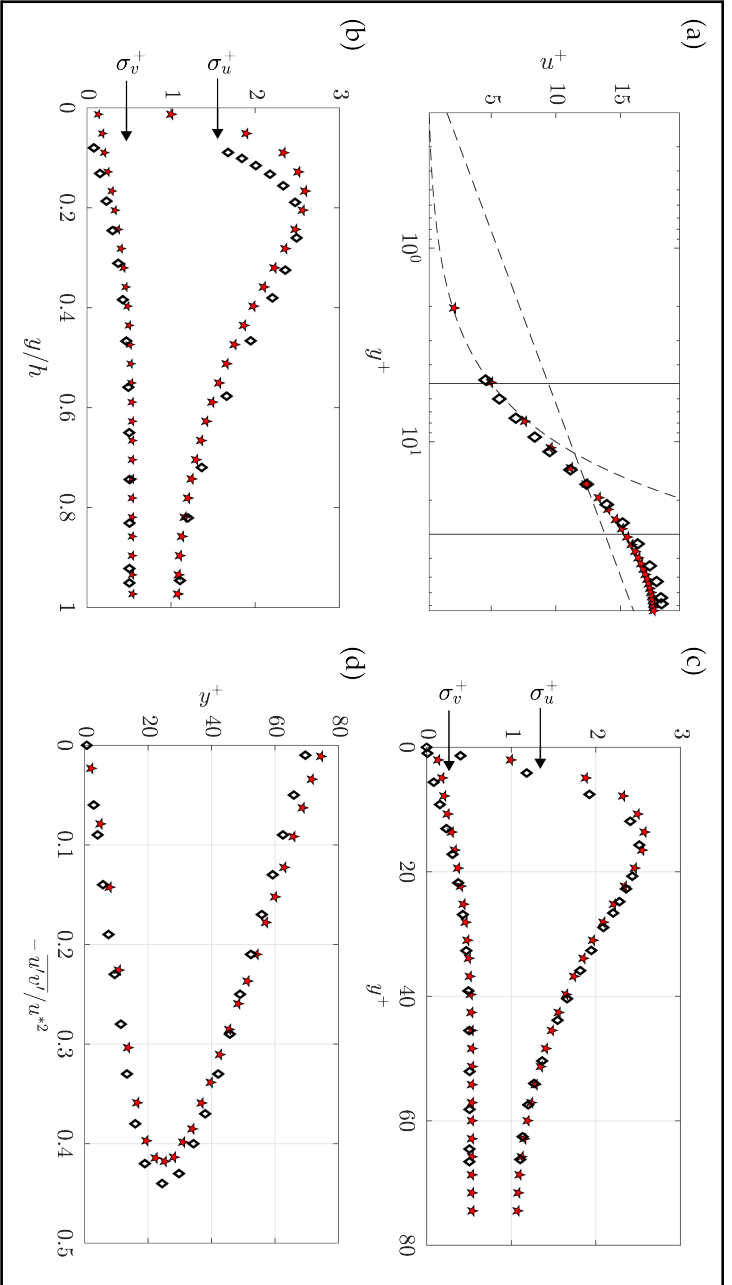


Fig. 3.4 Velocity statistics obtained from PIV measurements in the lower half of the test section at the streamwise position $x = 82.5$, $z=5$ cm (red stars) where h is the channel semi-height, $u^+ = \bar{u}/u^*$ is the normalised velocity, $y^+ = yu^*/\nu$ is the normalised distance from the wall; $\sigma_v^+ = \sqrt{\nu^2}/u^*$ and $\sigma_u^+ = \sqrt{u'^2}/u^*$ are the non-dimensional standard deviations of the wall-normal and longitudinal velocity, respectively and $\overline{u'v'}$ is the Reynolds shear stress. (a) non-dimensional mean-velocity profile (inner scaling), the dashed line represents the linear law $u^+ = y^+$, characterising wall flows for $y^+ \lesssim 5$ (see e.g., Pope [19]); (b) vertical profiles of σ_u^+ and σ_v^+ (outer scaling); (c) vertical profiles of σ_u^+ and σ_v^+ (inner scaling) and (d) non-dimensional Reynolds shear stress. Black diamonds indicate data from Tsukara [18], red stars indicate data from the benchmark test.

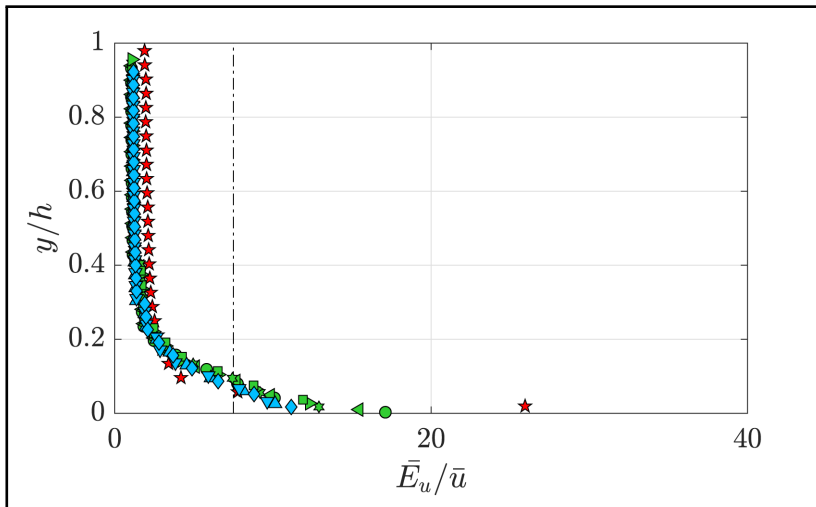


Fig. 3.5 Results of the uncertainty analysis of the PIV data at different distances from the wall (h is the channel semi-height) normalised with the local mean streamwise velocity \bar{u} and reported in percentage form. Symbols and experimental conditions for all the tests are reported in Table 3.1.

displacement assessment and hence the error in estimating the velocities [21].

- (iii) The perspex channel has tick lateral walls of 2.5 cm and presents a discontinuity right at the joint between the bottom and lateral walls. Both cause difficulties in acquiring the images due to slight distortion and less focus of frames within the very thin channel of 0.01 m.

These effects make it more difficult for the algorithm to detect particles close to the membrane and smooth-wall surface. A careful analysis of results-figures for both the benchmark indicates that for $y/h \leq 0.1$ (which corresponds to $\bar{E}_u/\bar{u} \approx 7.4\%$) the vertical profiles of various velocity statistics measured for the benchmark case (see e.g. Figure 3.4 and 3.11) become somewhat erratic and diverge from the expected behaviour. It was therefore decided that for $y/h \leq 0.1$ (i.e. $\bar{E}_u/\bar{u} \geq 7.4\%$) PIV data for all experimental conditions were not entirely reliable. For this reason, in the remaining part of the paper, data points pertaining to $y/h \leq 0.1$ should not be considered. They are, however, included in the result figures and indicated with a light dotted line for the sake of completeness and full transparency.

3.4.4 Assessment of non-uniformity in the filtration tests

The assessment of the flow non-uniformity associated with filtration tests is important for two reasons. Firstly, to justify the spatial averaging along transects parallel to the wall used for the calculation of velocity statistics (see Section 3.4.3), and secondly, to support the hypothesis underlying the estimation of the production term in the turbulent kinetic energy balance (see Section 3.5.1). For the first purpose, as already mentioned, it is necessary to demonstrate that the non-uniformity of the longitudinal velocity are negligible along the homogenous flow direction over the entire length of the measurement domain of the PIV tests (i.e. 35x5 mm) for a fixed distance from the wall y/h . For the second purpose, with reference to the same measurement domain, it is instead necessary to demonstrate that the changes in the mean flow in the longitudinal direction are negligible compared to those in the wall-normal direction.

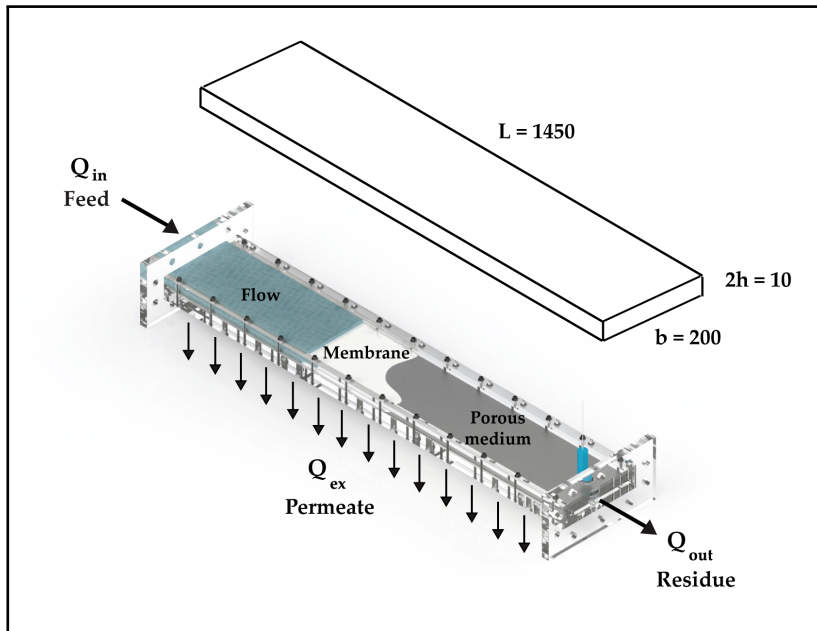


Fig. 3.6 Cross-flow scheme in a membrane module: Geometry of the test section (top) and representation of filtration process (bottom) where Q_{in} represent the feed flow, Q_{out} represent the residue of the process and Q_{ex} represent the permeate through the membrane.

The analysis is carried out for the worst case scenario, which corresponds to the LY 3 test reported in Table 3.1, namely, the test for which the higher permeate was observed and hence the maximum flow inhomogeneity is expected. Considerations based on dimensional analysis suggest the following:

- (i) The flux rate of $248.3 \text{ lm}^{-2}\text{h}^{-1}$ multiplied by the membrane area (i.e. 0.28 m^2) generates an outflow from the system Q_{ex} of approximately 69.5 lh^{-1} , corresponding to 4.6% of the feed flow Q_{in} . This change in flow rate, assuming a uniform filtration motion across the whole membrane (see Bert et al. [13]) corresponds to a linear change in longitudinal velocity along the test section of length $L = 1450 \text{ mm}$. Based on the geometry of the system shown in Figure 3.6, it is possible to obtain a difference between the average feed-flow velocity (estimated with the volume flow rate $Q_{in} = 1505 \text{ lh}^{-1}$) and that of the residue (estimated with volume flow rate $Q_{out} = 1435.5 \text{ l}^{-1}$) of approximately 0.0095 ms^{-1} . This implies that the variation in the mean longitudinal velocity $\partial\bar{u}/\partial x \approx 0.0095/1.45 = 0.0066 \text{ s}^{-1}$. This value referred to the length of the measurement domain used for the PIV acquisitions (equal to 35 mm) produces a mean longitudinal velocity variation of $2.31 \times 10^{-4} \text{ ms}^{-1}$, which is three orders of magnitude smaller than the average longitudinal velocity ($U = 0.209 \text{ ms}^{-1}$).
- (ii) The ratio between the derivative of the mean flow along the wall-normal direction can be estimated as $(\partial\bar{u}/\partial y) \approx U/h \approx 4.2 \text{ s}^{-1}$ which is order of magnitude larger than the estimated $\partial\bar{u}/\partial x$.

Therefore, based on what has been obtained, both assumptions (i.e. uniformity of flow in the direction of motion at a fixed distance from the wall y/h and negligible longitudinal derivatives with respect to the vertical ones) underlying the calculations procedures are verified.

3.5 Results

This results section is split into two parts. Section 3.5.1 presents a comparative analysis between the filtration and benchmark tests in terms of classical one-point velocity statistics. Section 3.5.2 attempts to provide an overview of how suction alters the structure of turbulence by means of quadrant analysis, cross-correlation functions and 1-D velocity spectra.

3.5.1 One-point statistics

The latest work on turbulent boundary layers over suction walls suggests that, for this class of flows, mean velocity profiles scale well in outer coordinates using the maximum velocity rather than the usual friction velocity u^* [1]². Figure 3.7 supports this idea as mean velocity profiles scale very well when normalised with the maximum velocity U_m , except perhaps in the region $y/h < 0.15$ where some weak dependence on Γ seems to occur. This implies that the new proposed scaling works well for both high and low Re (Ferro performed experiments for Re much greater than those employed herein) and over a wide range of Γ . Contrary to Ferro, though, the present mean velocity profiles do not display a logarithmic region due to the very low Reynolds number of the experiments.

Figure 3.8 reports the vertical profiles of non-dimensional mean shear which provides a deeper look into the behaviour of the mean flow and will be used later on to discuss aspects related to turbulent kinetic energy production. This Figure shows that mean shear also scales well throughout the channel semi-height when data are normalised using U_m and h . Some slight differences between the filtration tests and the benchmark case seem to begin developing in the near-wall region, suggesting that suction tends to suppress mean shear. To the author's opinion, this is a plausible result since a porous wall, although as thin as the membranes employed herein, can impose a free slip at the wall and hence a drop in shear.

²This represents a great advantage as u^* is extremely difficult to estimate in the case of suction flows, where the wall shear stress is strongly influenced by the vertical momentum transfer caused by suction right at the wall (i.e. $\rho \overline{u'v'}$ at $y=0$), where velocity measurements are indeed very hard to perform.

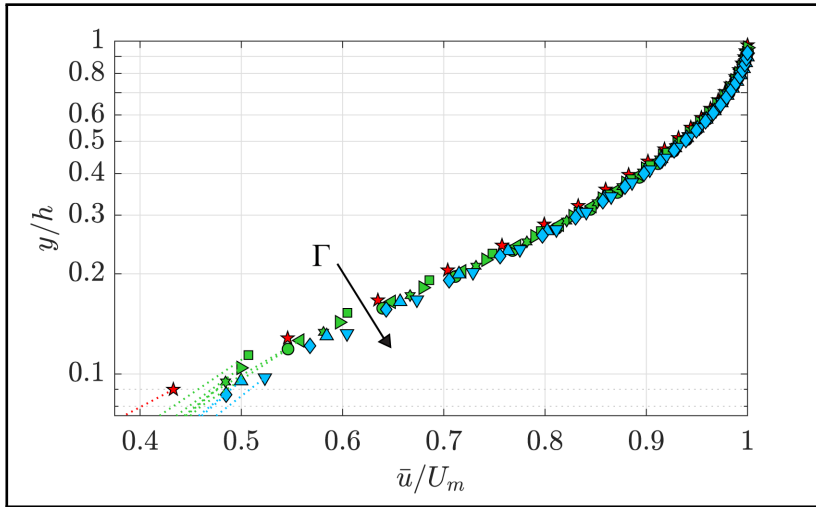


Fig. 3.7 Non-dimensional velocity profiles. h is the channel semi-height; \bar{u} is the local mean streamwise velocity and U_m is the maximum velocity at the centre of the channel. Symbols and experimental conditions for all the tests are reported in Table 3.1.

However, since this drop occurs in the proximity of the flow region where PIV data begin to be not as reliable, this aspect is not further discussed.

Figure 3.9 shows the vertical profiles of the non-dimensional standard deviations $\sigma_u^m = \sqrt{u'^2}/U_m$ and $\sigma_v^m = \sqrt{v'^2}/U_m$ for all the investigated cases. Some interesting aspects emerge:

- (i) Firstly, σ_u^m and σ_v^m profiles collapse nicely for all investigated filtration tests. Note that since Re was kept constant along with such tests, U_m was also roughly the same, hence implying that velocity standard deviations $\sqrt{u'^2}$ and $\sqrt{v'^2}$ are essentially insensitive to Γ .
- (ii) In past studies related to turbulent boundary layers, Antonia et al. [10] argued that suction tends to suppress vertical velocity fluctuations more than the longitudinal ones. In the present case, Figure 3.9 provides a picture that is more complex than that. With respect to the benchmark case, σ_v for filtration tests is essentially unaltered in the near-wall region (i.e. for $y/h < 0.2$), while it drops significantly (of about 25 %) in the outer region. In contrast, σ_u drops throughout the entire flow domain with the maximum drop occurring in the proximity of the near-wall peak.

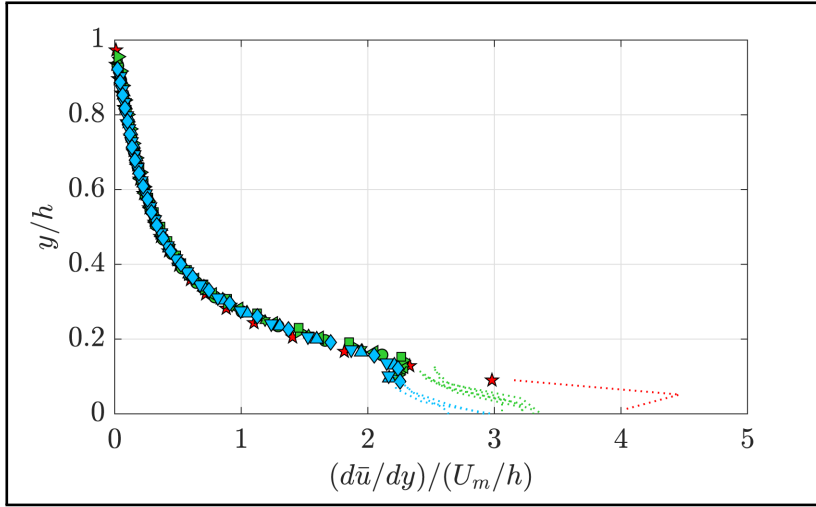


Fig. 3.8 Non-dimensional shear stress; h is the channel semi-height and U_m is the maximum velocity at the centre of the channel. Symbols and experimental conditions for all the tests are reported in Table 3.1.

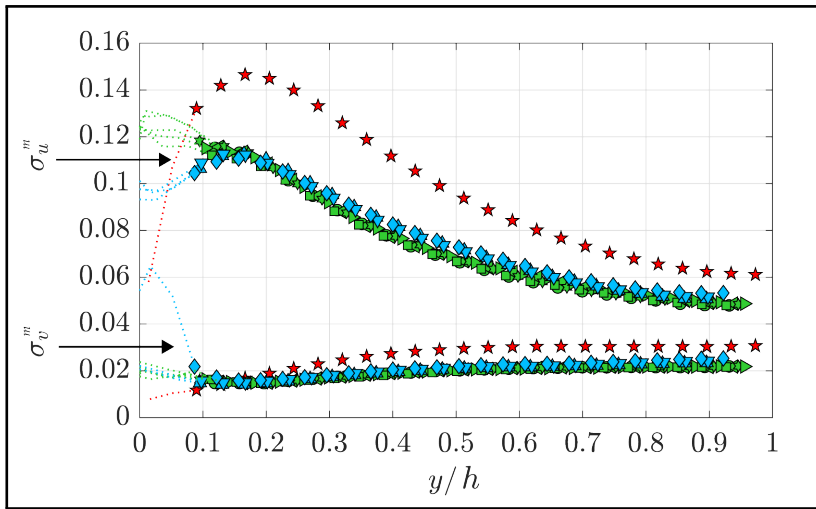


Fig. 3.9 Non-dimensional profiles of the velocity variances for the streamwise $\sigma_u^m = \sqrt{u'^2}/U_m$ and wall-normal $\sigma_v^m = \sqrt{v'^2}/U_m$ directions; h is the channel semi-height and U_m is the maximum velocity at the centre of the channel. Symbols and experimental conditions for all the tests are reported in Table 3.1

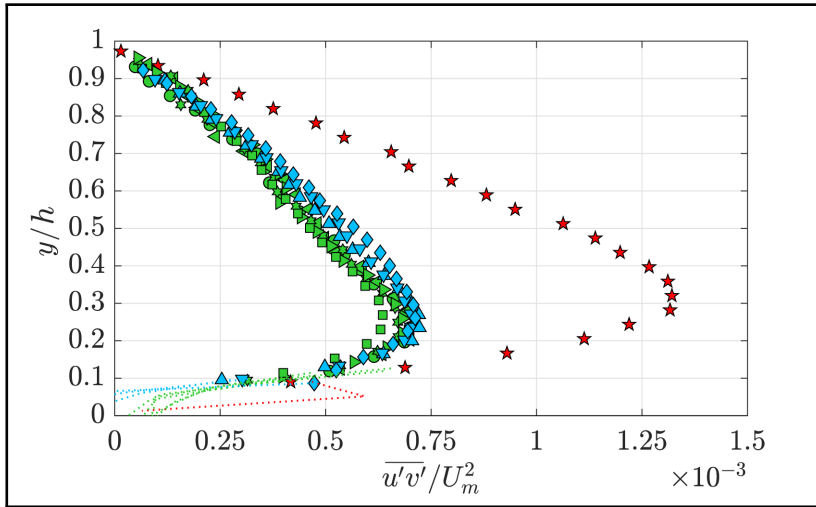


Fig. 3.10 Non-dimensional Reynolds stress; h is the channel semi-height and U_m is the maximum velocity at the centre of the channel and u' av' the velocity fluctuations in the streamwise and wall-normal direction, respectively. Symbols and experimental conditions for all the tests are reported in Table 3.1.

Analogously to $\sqrt{u'^2}$ and $\sqrt{v'^2}$ also the non-dimensional shear Reynolds stress $-\overline{u'v'}/U_m^2$ is significantly reduced by suction (see Figure 3.10) regardless of Γ .

It can be therefore concluded that turbulent velocity fluctuations are tremendously damped by suction, but such damping is independent of Γ . This result is rather counterintuitive. Antonia et al. [10] argued that turbulence damping by suction is associated with a stabilisation of near-wall streaks and, in turn, with the weakening of the burst cycle. The burst cycle is indeed triggered by the sinuous instability of near-wall vortices characterised by longitudinal vorticity (the footprint on these vortices on the longitudinal velocity field causes the alternating high and low velocity streaks normally observed near the wall) [19]. Our data somewhat supports the idea that suction tends to suppress/alter this sinuous instability so much so turbulence ends up being in a different state. Such a state is then maintained regardless of the suction rate Γ (at least for the range of the Γ -values herein investigated).

Further considerations about the observed damping of velocity fluctuations can be deduced from the analysis of Turbulent Kinetic Energy (TKE) production

and dissipation (Figure 3.12). Using index notation, the production term is defined as:

$$P = -\overline{u'_i u'_j} \frac{\partial \bar{u}_i}{\partial x_j} \quad (3.1)$$

This term contains nine components, however, assuming the flow to be roughly two-dimensional (i.e. $\bar{u}_2 = \bar{w} = 0$, where w is the lateral velocity component) and variations of the mean flow along the longitudinal and lateral directions to be significantly smaller than those along the vertical direction (i.e. $\partial/\partial x, \partial/\partial z \ll \partial/\partial y$, see Section 3.4.4) implies that P can be estimated reasonably well, as:

$$P = -\overline{u'_1 u'_2} \frac{\partial \bar{u}_1}{\partial x_2} = -\overline{u'v'} \frac{\partial \bar{u}}{\partial y} \quad (3.2)$$

Reliable estimations of the TKE dissipation rate require careful measurement of the instantaneous strain rate tensor. This is clearly impossible with the measurement techniques employed in the present paper. However, a reasonably good estimation can be provided by making the isotropic approximation (this implies assuming that turbulence at small scales is isotropic) so that the TKE dissipation rate ε can be computed as (see e.g. Pope [19]):

$$\varepsilon = 15\nu \overline{\left(\frac{\partial u}{\partial x}\right)^2} \quad (3.3)$$

Estimating Equation 3.3 from PIV data is not an easy task. It is indeed not straightforward to choose the spatial distance Δ over which computing instantaneous velocity derivatives. From a purely theoretical standpoint, Δ should be taken as small as possible and approaching the Komogorov length scale. However, the smaller is Δ the more velocity differences are affected by experimental noise.

The problem was herein circumvented as follows. TKE dissipation rates were estimated by varying Δ extensively. Results were then compared with the DNS of Tsukara et al.[18] and it was observed that when $\Delta = 0.78$ mm a good agreement

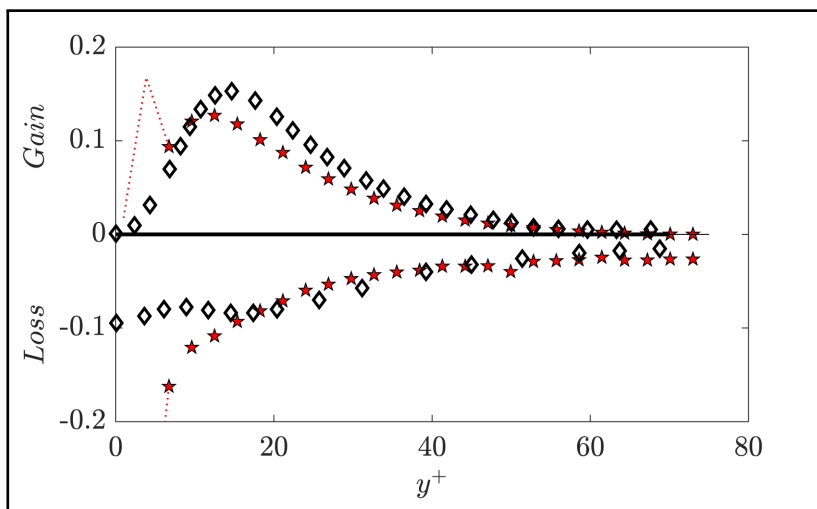


Fig. 3.11 TKE production P and dissipation ε . Black diamonds indicate data from Tsukara [18], red stars indicate data from the benchmark test.

of the data was obtained except near the wall for what concerns the dissipation rate (see Figure 3.11). The same value of Δ was employed to estimate ε also for the filtration tests as these were carried out at almost identical Reynolds number and very similar PIV setup.

Figure 3.12 presents P and ε plotted in non-dimensional form and shows that TKE production for filtration tests is significantly reduced when compared with the benchmark case, especially in the near-wall region. According to Equation 3.2, since the mean shear between the benchmark and filtration tests is very similar, the observed drop in P for the filtration tests is clearly associated with the decrease in Reynolds stress reported in Figure 3.10.

Interestingly, the vertical profiles of ε , when scaled with U_m and h , show no dependence on the suction rate Γ . This is reasonable because, intuitively, there is no reason why small scales of turbulence should be affected by suction. Moreover, for the filtration tests, it seems that the peak in P observed in the near-wall region is almost, if not completely, compensated by the dissipation rate ε , which then dominates over P in the overlying flow regions. This implies that, in filtration tests, very little TKE that is produced in the near-wall region is left to be transported vertically to fuel up velocity fluctuations in the outer region. Hence this explains

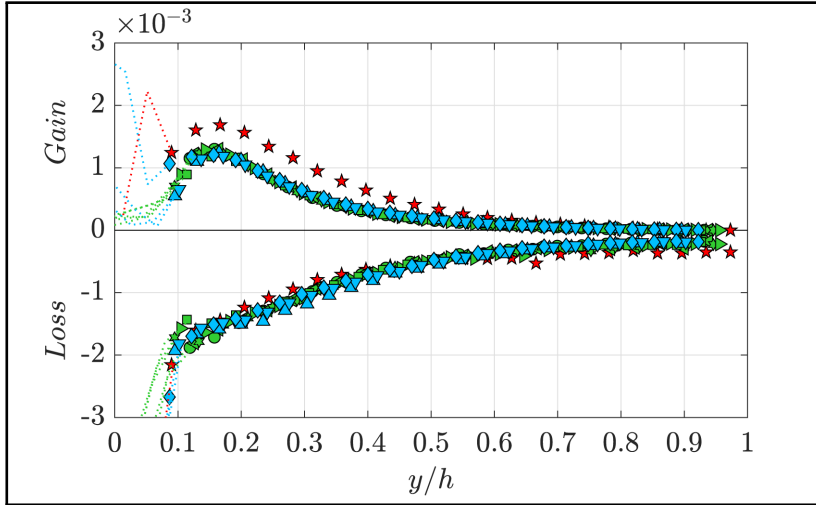


Fig. 3.12 Production term $P = \overline{u'v'}(\partial\bar{u}/\partial y)$ and dissipation term $D = \varepsilon = 15\nu\overline{(\partial\bar{u}/\partial x)^2}$ of the Turbulent Kinetic Energy (TKE) balance in non-dimensional form. Gain and Loss are multiplied by h/U_m^3 ; h is the channel semi-height and U_m is the maximum velocity at the centre of the channel. Symbols and experimental conditions for all the tests are reported in Table 3.1.

why an altered burst cycle in the near-wall region as conjectured by Antonia et al. [10] can be responsible for reducing velocity fluctuations (and hence TKE) away from the wall as observed in Figure 3.9.

3.5.2 Turbulent structure

This section attempts to provide an overview of how suction alters the spatial and temporal structure of turbulence. Towards this end, classical Quadrant Analysis (QA) represents a simple and straightforward way to gather some information. QA classifies instantaneous turbulence events according to the combined sign of instantaneous longitudinal and vertical velocity fluctuations. So-called sweeps, ejections, outward interactions and inward interactions are detected for $(u' > 0, v' < 0)$, $(u' < 0, v' > 0)$, $(u' > 0, v' > 0)$, $(u' < 0, v' < 0)$, respectively. In wall turbulence, it is well known that sweeps and ejections are the events that contribute to the dominant turbulent momentum transport term (i.e. to the covariance $\overline{u'v'}$) and hence are the focus of the present analysis [22]. In QA it is customary to focus

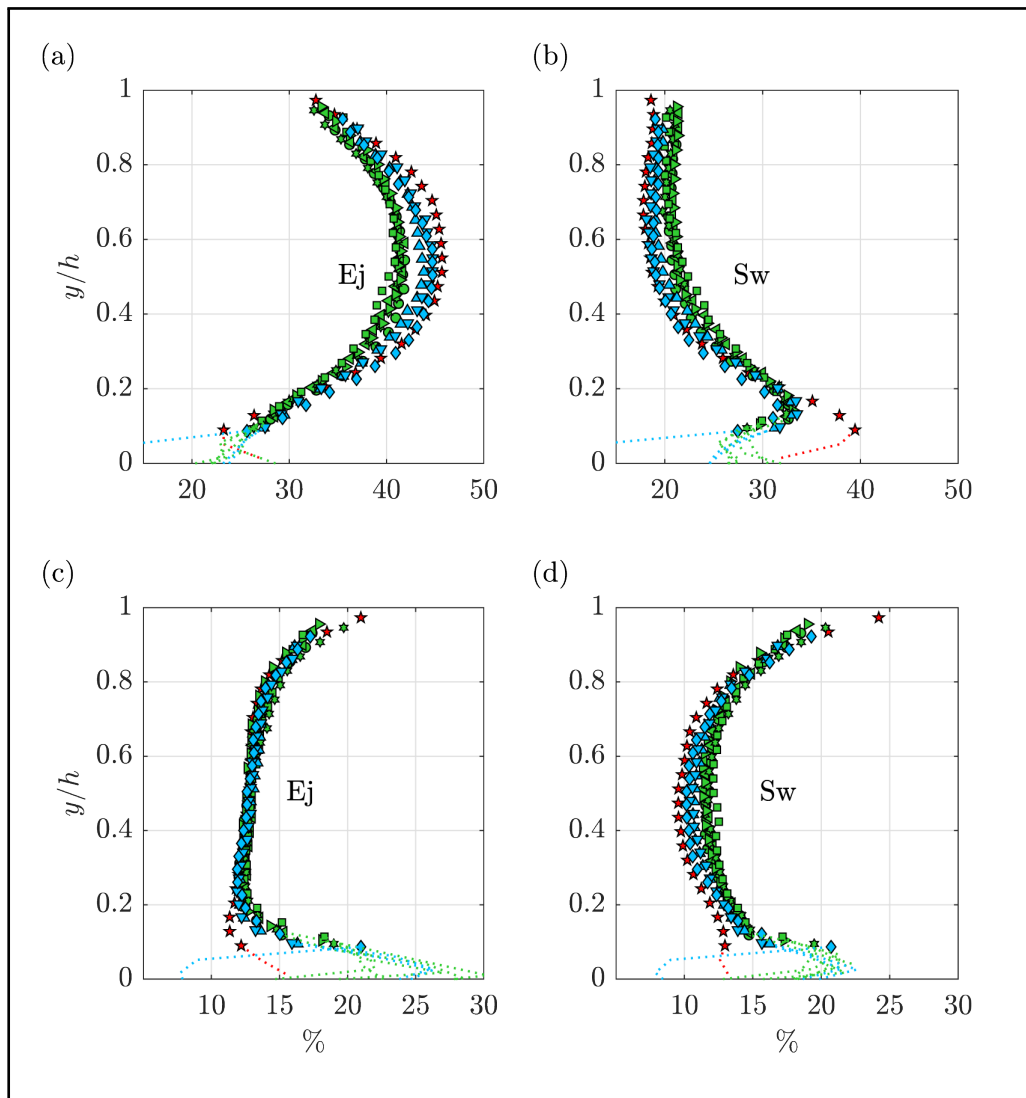


Fig. 3.13 Intensity ratio $Ir_{(ej)\vee(sw)} = \frac{\sum (u'v')_{(ej)\vee(sw)}}{\sum (u'v')_{(tot)}}$ and Occurrence ratio $Or_{(ej)\vee(sw)} = \frac{n_{(ej)\vee(sw)}}{n_{(tot)}}$ obtained from quadrant analysis at different y/h . "Ej" and "Sw" stand for Ejection and Sweep, respectively; u' and v' are the velocity fluctuations in the streamwise and wall-normal directions and n stands for the number of events. (a) Intensities of the Ejections; (b) Intensities of the Sweeps; (c) Occurrence of the Ejections and (d) Occurrence of the Sweeps. Symbols and experimental conditions for all the tests are reported in Table 3.1.

on the most intense events that satisfy the relationship $|u'v'| > H|\overline{u'v'}|$ with $H = 1.75$ (see [23, 24]).

Two different quantities were estimated: the intensity ratio Ir (Equation 3.4) and Occurrence ratio Or (Equation 3.5) defined as follows:

$$Ir_{(ej)\vee(sw)} = \frac{\sum (u'v')_{(ej)\vee(sw)}}{\sum (u'v')_{(tot)}} \quad (3.4)$$

$$Or_{(ej)\vee(sw)} = \frac{n_{(ej)\vee(sw)}}{n_{(tot)}} \quad (3.5)$$

Ir quantifies the contribution of sweeps or ejections to turbulent momentum transport, whereas Or quantifies how often one event occurs.

Figure 3.13a shows that the contribution of ejections to the total covariance $\overline{u'v'}$ is about the same for all experimental conditions (variations between filtration and benchmark tests are of 5% at most). However, Figure 3.13c demonstrates that in filtration tests ejections undergo a 10% increase in Or in the near-wall region, meaning that, at this location, they occur slightly more often than in the benchmark case. Within the same region, suction weakens the contribution of sweeps to the total covariance $\overline{u'v'}$ (Figure 3.13 b) while forcing them to occur more often than in the benchmark case (Figure 3.13 d). In summary, it appears that suction tends to force momentum transport to occur over an increased number of weakened ejection and sweep events. Figure 3.14 indicates that this slight weakening of sweeps and ejections for the filtration tests results in a slight but not dramatic weakening of the correlation coefficient $R = (\langle \overline{u'v'} \rangle) / (\langle \sqrt{u'^2} \rangle \langle \sqrt{v'^2} \rangle)$, which, to some extent, quantifies the level of coherency of turbulence.

In order to obtain information about how suction alters the spatial structure of large-scale turbulence, it is instructive to assess contour plots of the two-point cross-correlation function for the longitudinal velocity component defined as:

$$R_{uu}(X, Y) = \frac{\overline{u'(X, Y)u'(X + \Delta X, Y + \Delta Y)}}{\sigma_{u(X, Y)} \sigma_{u(X + \Delta X, Y + \Delta Y)}} \quad (3.6)$$

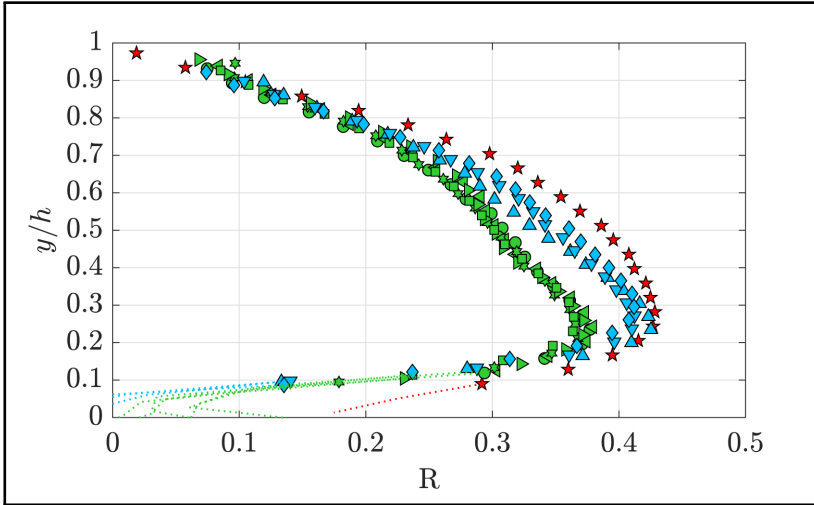


Fig. 3.14 Non-dimensional autocorrelation coefficient $R = \langle \langle u'v' \rangle \rangle / (\langle \sqrt{u'^2} \rangle \langle \sqrt{v'^2} \rangle)$; h is the channel semi-height and u' and v' the velocity fluctuations in the streamwise and wall-normal direction, respectively. Symbols and experimental conditions for all the tests are reported in Table 3.1.

Where X, Y was fixed at $X = 7\text{mm}$, $Y = 1.2\text{mm}$ (corresponding to $Y/H_c = 0.24$) and the spatial lags varied to cover the entire flow domain (see Figure 3.15a). Contour plots of R_{uu} are often used to estimate the angle γ at which large-scale structures are tilted in response to mean shear. Towards this end, it is assumed that γ corresponds to the slope of the line fitting the position of local maxima in R_{uu} contours (see e.g. the dash-dot line in Figure 3.15a). The exact value of γ is notoriously dependent on the vertical coordinate of the fixed point Y [25–27]. In order to explore such dependence and have a more objective overview of results, γ was estimated by varying Y within the range $0.17 < Y/H_c < 0.3$. Results from these calculations are reported in Figure 3.15b, which shows how, for all experimental conditions, γ is extremely small when compared with the 10–15 degrees normally reported for high Reynolds number boundary layers. This is clearly an effect of the low Re at which experiments were carried out, whereby long longitudinal vortices associated with high and low-speed streaks are pervasive over the full half depth of the channel H_c and dominate the observed values of R_{uu} . Contrary to coherent structures normally observed for high Reynolds number wall

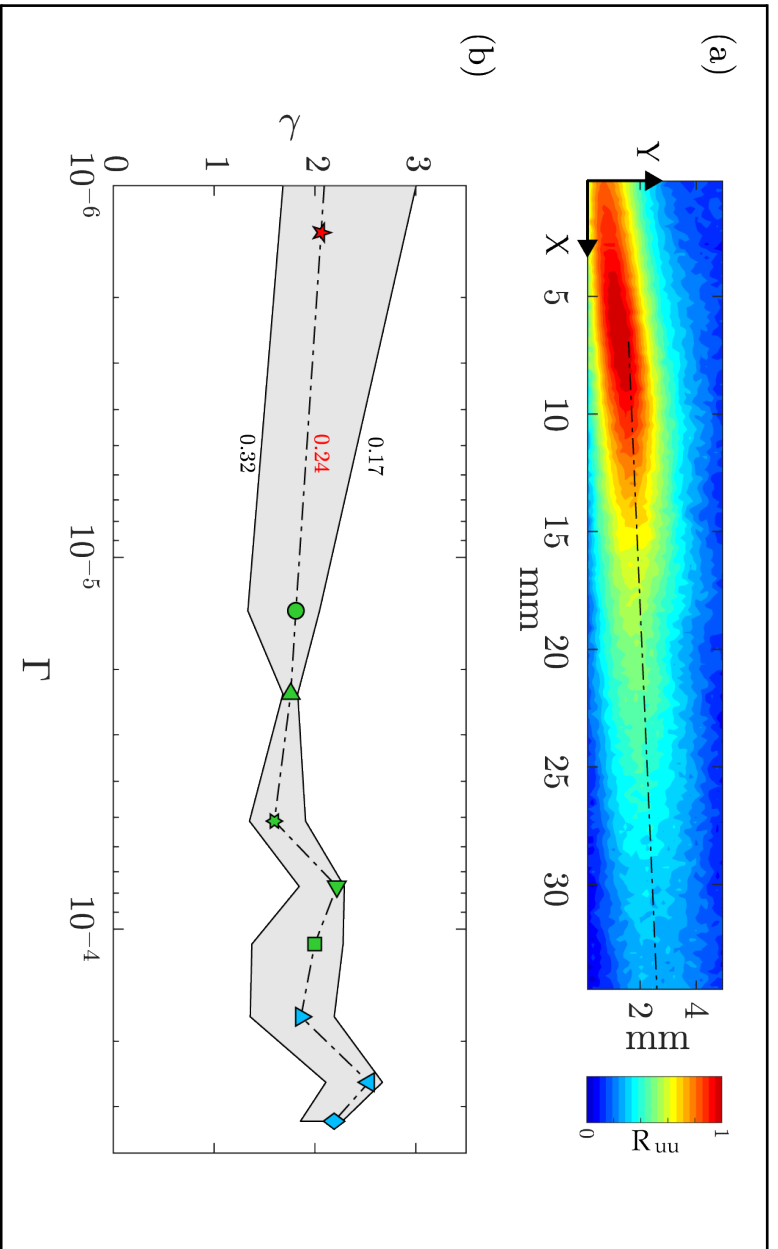


Fig. 3.15 Large turbulence structures inclination angle: (a) Contour plot of the turbulent structure obtained from the two-point correlation $R_{uu}(X, Y) = u'(X, Y)u'(X + \Delta X, Y + \Delta Y) / \sigma_{u(X,Y)}\sigma_{u(X+\Delta X, Y+\Delta Y)}$ for the impermeable wall condition. Coordinates of the point used for the calculation are $X = 7$ mm and $Y = 1.2$ mm, which corresponds to a ratio $Y/H_c = 0.24$ (this contour plot refers to the red star in panel b); (b) Inclination angle γ vs. suction rate $\Gamma = V/U$ (where V is the mean vertical velocity through the porous media and U the mean velocity of the feed flow) at the position $x = 7$ mm for three different distances from the wall $Y/H_c = 0.17$, $Y/H_c = 0.24$ and $Y/H_c = 0.32$. Symbols and experimental conditions for all the tests are reported in Table 3.1.

flows (i.e. hairpin eddies and packets of hairpin eddies), such vortices are known to be wall parallel with essentially no inclination angle.

In order to obtain more information about how energy is distributed among different scales of motion, it was decided to carry out a spectral analysis. It became immediately apparent that PIV data were not suited for such a task because, on the one hand, the low sampling frequency of velocity fields (i.e. 4Hz) made it meaningless to estimate spectra in the frequency domain. On the other hand, the relatively small size of the measuring window investigated by means of PIV made it meaningless to compute 1-D spectra directly in the wavenumber domain as a large-scale structure would have been left out. Moreover, as far as small scales are concerned, below a certain cut-off value, which is a function of the grid dimension, the accuracy of spectral estimations using PIV data is known to be limited by noise and spatial filtering [28].

As outlined in Section 3.4.2, some LDA measurements were therefore performed to complement PIV data and compute 1-D spectra in the frequency domain. Transformation into the wavenumber domain was carried out using the Taylor's hypothesis of frozen turbulence using local time-averaged velocities as the convection velocity. Hence wavenumbers k_x , were estimated as $k_x = 2\pi f / \bar{u}$.

Figure 3.16a reports (dimensional) spectral densities estimated for the longitudinal velocity E_{uu} and plotted in premultiplied form for the benchmark case. At $Re = 4000$ (i.e. the same Re as used in the PIV experiments) premultiplied spectra display an unexpected bimodal distribution, with a peak occurring at $k_x \approx 20$, which corresponds to scales of the order of 30 times the total channel height. Scales of motion of this size in wall turbulence are normally associated with Very large Scale Motions, which however, require large Reynolds numbers to form and to be captured by spectral analysis (see e.g. Peruzzi et al. [29]). Experiments were therefore carried out over a wide range of Re (see Table 3.2) and a clear picture emerged. The higher is Re the more such a peak moves towards higher wavenumbers and eventually dies off, leaving another peak to further emerge at wavenumbers corresponding to about 1000 viscous wall units (i.e. $1000 \nu / u^*$), which is the length of near-wall streaks normally detected in wall flows (see figure 3.16a). It is therefore plausible that, at the Reynolds numbers at which benchmark

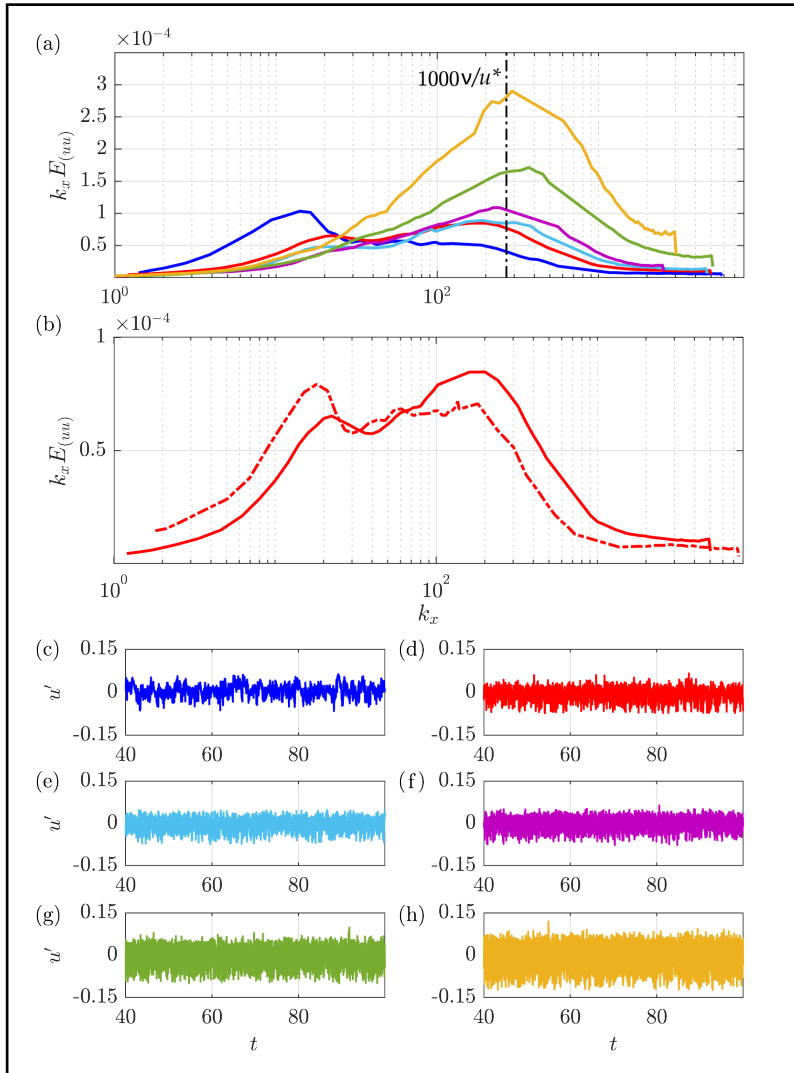


Fig. 3.16 Power spectra analysis and non-dimensional velocity signals where k_x is the wave number $k_x = 2\pi f/\bar{u}$, $k_x E_{(uu)}$ is the spectral density of the longitudinal velocity component $k_x E_{uu} = (\bar{u}/2\pi)E_{(f)}$, \bar{u} is the mean velocity calculated from the time series of the eddy-convective velocity and time t is expressed in seconds. (a) Pre-multiplied power density spectra for smooth-wall impermeable condition and Reynolds number between 3000 and 12000; (b) Comparison of the pre-multiplied power density spectra at Reynolds number 4000 for the smooth-wall impermeable condition and BN flat-sheet membrane; (c) Non-dimensional velocity signal at $Re = 3000$; (d) Non-dimensional velocity signal at $Re = 4000$; (e) Non-dimensional velocity signal at $Re = 5000$; (f) Non-dimensional velocity signal at $Re = 6000$; (g) Non-dimensional velocity signal at $Re = 8400$; (h) Non-dimensional velocity signal at $Re = 12000$. Panel (a) also show the line for $k_x = 1000$ corresponding to the length of near-wall streaks. Symbols and experimental conditions for all the tests are reported in Table 3.2

and filtration tests were investigated, transitional effects were still significant. In other words, it is plausible that the most unstable modes which are responsible for laminar to turbulence transition in channel flows (and which typically occur at fairly large scales, see [30]), were still able to impose their footprint in the flows and were not yet dissipated by turbulence in its fully developed form, despite the measured velocity time series display to sign of turbulent puffs and laminarised events as normally observed in transitional flows (see Figure 3.16c-h).

Note that for the investigated filtration test at $Re \approx 4000$ (figure 3.16a, dashed red line) the low wavenumber peak is also present in premultiplied spectra and more pronounced with respect to the benchmark case (solid red line). This is somewhat in agreement with the hypothesis that suction favours flow stability, as speculated in the preceding sections when discussing its effects on near-wall streaks.

3.6 Conclusion

The most relevant results obtained from both PIV and LDA experiments are summarised as follows:

- (i) Vertical profiles of one-point statistics measured in filtration tests scale very well using the mid-channel height h and the maximum mean longitudinal velocity U_m to normalise the vertical coordinate and velocity statistics, respectively.
- (ii) Suction reduces the standard deviations of the longitudinal and wall-normal velocity fluctuations as well as their covariance (i.e. all measured Reynolds stress components). Surprisingly, this reduction is independent of the value of the suction rate Γ . It was therefore argued that, as surmised from the literature, suction works to stabilise near-wall streaks and to generate turbulence pertaining to a different self-sustained state that is independent of Γ .
- (iii) Consistently with this reduction in Reynolds stress, the enhanced flow stability mentioned in point 2 contributes to reducing the production of TKE, especially in the very near-wall region. In contrast, estimations of TKE dissipation rate seem to be unaltered by suction. This implies that production and dissipation in the proximity of the near-wall peak of P are almost in equilibrium hence leaving no TKE to be transported higher up to fuel up turbulence intensities in the outer region as it happens in canonical wall flows. It was speculated that it is for this reason that velocity standard deviations are reduced by suction throughout the channel height and not only in the near-wall region where the presumed stabilisation phenomenon occurs.
- (iv) Despite suction has clearly macroscopic and evident effects on one-point statistics, it is puzzling to observe that it has rather weak effects on the turbulence structure as detected by means of quadrant analysis and two-point cross-correlation functions.
- (v) The spectral analysis demonstrated that both benchmark and filtration flows at $Re = 4000$ show the presence of some large-scale motions that were

completely unexpected. Experiments at different Re demonstrate that the spectral signature of such scales of motion becomes more evident as Re decreases and less evident at high Re until it disappears. This suggests that such scales of motion are probably related to unstable modes associated with laminar to turbulence transition. Interestingly, it was also observed that suction tends to enhance the spectral peak associated with the aforementioned large-scale structures. This is consistent with the idea proposed in point 2 that wall suction tends to stabilise the flow hence further delaying the occurrence of a fully turbulent state.

References

- [1] M. Ferro, *Experimental study on turbulent boundary-layer flows with wall transpiration*. PhD thesis, KTH Royal Institute of Technology, 2017.
- [2] S. Yoshioka and P. H. Alfredsson, “Control of turbulent boundary layers by uniform wall suction and blowing,” in *IUTAM Symposium on Laminar-Turbulent Transition*, pp. 437–442, Springer, 2006.
- [3] H. Tennekes, “Similarity laws for turbulent boundary layers with suction or injection,” *Journal of Fluid Mechanics*, vol. 21, no. 4, pp. 689–703, 1965.
- [4] T. Black and A. Sarnecki, “The turbulent boundary layer with suction or injection,” 1958.
- [5] R. A. Dutton, “The effects of distributed suction on the development of turbulent boundary layers,” 1958.
- [6] J. M. Kay, “Boundary-layer flow along a flat plate with uniform suction,” 1948.
- [7] T. Khapko, P. Schlatter, Y. Duguet, and D. S. Henningson, “Turbulence collapse in a suction boundary layer,” *Journal of Fluid Mechanics*, vol. 795, pp. 356–379, 2016.
- [8] A. Bobke, R. Örlü, and P. Schlatter, “Simulations of turbulent asymptotic suction boundary layers,” *Journal of Turbulence*, vol. 17, no. 2, pp. 157–180, 2016.
- [9] Y. Kametani, “Direct numerical simulation of friction drag reduction in spatially developing turbulent boundary layers,” 2013.

- [10] R. Antonia, Y. Zhu, and M. Sokolov, "Effect of concentrated wall suction on a turbulent boundary layer," *Physics of Fluids*, vol. 7, no. 10, pp. 2465–2474, 1995.
- [11] P. Xu, J. E. Drewes, T.-U. Kim, C. Bellona, and G. Amy, "Effect of membrane fouling on transport of organic contaminants in nf/ro membrane applications," *Journal of Membrane Science*, vol. 279, no. 1-2, pp. 165–175, 2006.
- [12] W. S. Ang, A. Tiraferri, K. L. Chen, and M. Elimelech, "Fouling and cleaning of ro membranes fouled by mixtures of organic foulants simulating wastewater effluent," *Journal of membrane science*, vol. 376, no. 1-2, pp. 196–206, 2011.
- [13] R. Bert, C. Manes, and A. Tiraferri, "New facility for membrane fouling investigations under customizable hydrodynamics: Validation and preliminary experiments with pulsating cross-flow," *Membranes*, vol. 12, no. 3, p. 334, 2022.
- [14] I. Nedyalkov, "Design of contraction, test section, and diffuser for a high-speed water tunnel," Master's thesis, 2012.
- [15] R. Bosio, "Analisi sperimentale con lda in condizioni di turbolenza omogenea ed isotropa. = experimental analysis with lda in conditions of homogeneous and isotropic turbulence." Luglio 2018.
- [16] Z. Xue, J. J. Charonko, and P. P. Vlachos, "Signal-to-noise ratio, error and uncertainty of piv measurement," *PIV13*, 2013.
- [17] J. Westerweel and F. Scarano, "Universal outlier detection for piv data," *Experiments in fluids*, vol. 39, no. 6, pp. 1096–1100, 2005.
- [18] T. Tsukahara, Y. Seki, H. Kawamura, and D. Tochio, "Dns of turbulent channel flow at very low reynolds numbers," in *Fourth International Symposium on Turbulence and Shear Flow Phenomena*, Begel House Inc., 2005.
- [19] S. B. Pope and S. B. Pope, *Turbulent flows*. Cambridge university press, 2000.

-
- [20] J. J. Charonko and P. P. Vlachos, “Estimation of uncertainty bounds for individual particle image velocimetry measurements from cross-correlation peak ratio,” *Measurement Science and Technology*, vol. 24, no. 6, p. 065301, 2013.
- [21] S. Scharnowski and C. J. Kähler, “Particle image velocimetry-classical operating rules from today’s perspective,” *Optics and Lasers in Engineering*, vol. 135, p. 106185, 2020.
- [22] J. M. Wallace, “Quadrant analysis in turbulence research: history and evolution,” *Annual Review of Fluid Mechanics*, vol. 48, pp. 131–158, 2016.
- [23] W. Willmarth and S. Lu, “Structure of the reynolds stress near the wall,” *Journal of Fluid Mechanics*, vol. 55, no. 1, pp. 65–92, 1972.
- [24] Y. Shi, Z. Xia, and S. Chen, “A new identification method in sampled quadrant analysis for wall-bounded turbulence,” *Physics of Fluids*, vol. 28, no. 6, p. 061702, 2016.
- [25] H.-Y. Liu, T.-L. Bo, and Y.-R. Liang, “The variation of large-scale structure inclination angles in high reynolds number atmospheric surface layers,” *Physics of Fluids*, vol. 29, no. 3, p. 035104, 2017.
- [26] K. Chauhan, N. Hutchins, J. Monty, and I. Marusic, “Structure inclination angles in the convective atmospheric surface layer,” *Boundary-layer meteorology*, vol. 147, no. 1, pp. 41–50, 2013.
- [27] S. C. Morris, S. R. Stolpa, P. E. Slaboch, and J. C. Klewicki, “Near-surface particle image velocimetry measurements in a transitionally rough-wall atmospheric boundary layer,” *Journal of Fluid Mechanics*, vol. 580, pp. 319–338, 2007.
- [28] C. Atkinson, N. A. Buchmann, O. Amili, and J. Soria, “On the appropriate filtering of piv measurements of turbulent shear flows,” *Experiments in fluids*, vol. 55, no. 1, pp. 1–15, 2014.

- [29] C. Peruzzi, D. Poggi, L. Ridolfi, and C. Manes, “On the scaling of large-scale structures in smooth-bed turbulent open-channel flows,” *Journal of Fluid Mechanics*, vol. 889, 2020.
- [30] P. J. Schmid, D. S. Henningson, and D. Jankowski, “Stability and transition in shear flows. applied mathematical sciences, vol. 142,” *Appl. Mech. Rev.*, vol. 55, no. 3, pp. B57–B59, 2002.

Chapter 4

Fouling mitigation: An investigation by means of pulsed-flow

4.1 Abstract

As is widely known, fouling is the main issue in membranes-separation processes. Specifically, colloidal fouling of porous membranes involves particle deposition, either on the membrane surface or within the porous structure, which increases the hydraulic resistance leading to flux and selectivity reduction over time. Since this phenomenon is unavoidable, control approaches that minimise process complexity and operational costs are required to mitigate its effects. To this end, pulsed-hydrodynamics methods have proved to be cost-effective and easily implementable solutions. However, results presented in the literature so far are rarely of general validity and they provide marginal support to understanding the physics underpinning the problem. In this sense, more reliable information can be obtained using dimensionless quantities and better-designed apparatuses. For this reason, current-dominated pulsed flow experiments were conducted in newly constructed ad hoc facility under well-controlled conditions, and the imposed wave's non-dimensional frequency and non-dimensional amplitude were used to interpret the results. Quantitative measurements of the filtration rate have proven that fouling is less severe for low frequencies, and an increase in the filtration rate of the order of 10% was observed, while qualitative measurements of the surface suggest a less uniform pattern deposition compared to steady case. Conversely, the amplitude variation of the imposed disturbance seems to have little influence.

4.2 Introduction

Since the early 1960s, technological development and new manufacturing techniques have paved the way for the large-scale distribution of defect-free, high-flux membranes [1], providing a gradual transition from laboratory process to an industrial market with a value of more than USD 7 billion. This exponential growth is due to some of the inherent advantages of this technology, namely its high sensitivity in separating substances, low energy consumption, and the possibility to build compact and easily scalable systems [2]. As a result, high flux membranes are now deployed in a wide range of sectors, such as food production, energy production, pharmaceutical and chemical industries. Examples of their application are the processing of dairy products and beverages (e.g. wine, beer, fruit juices) [3], the separation of gases such as hydrogen, nitrogen enrichment, natural gas sweetening [4], CO₂ capturing from fossil fuel power plants and the production of nanoscale interfaces used in biological systems and medical applications such as drug delivery systems or microdialysis [5]. However, promoting the recovery of polluted water and meeting the growing water demand requires a better understanding of the limitation underpinning the operation of desalination [6] and wastewater treatment plants [7] that cover together 45% of the global membranes market [8].

The main problems with such application are concentration polarisation and fouling, which cause a decrease in the permeate over time if the flux through the porous medium induced by the application of transmembrane pressure (TMP) exceeds the so-called "critical flux" [9]. Concentration polarization is induced by membrane semi-permeability and selectivity and causes a reversible accumulation of rejected solutes or particles in a mass transfer boundary layer adjacent to the surface [10]. On the other hand, fouling may lead to an irreversible loss of permeability and damage the membrane as the matter in the feed solution leaves the liquid phase to form a deposit on either the membrane surface or inside its porous structure [11]. Consequently, fouling mechanisms (i.e. gel formation, adsorption, deposition, pore blockage, or cake formation) increase the osmotic pressure and hydraulic resistance across the membrane lowering the driving force

of the process and solute rejection, causing a reduction of membrane flux and selectivity over time.

Since fouling is unavoidable, control approaches are required to mitigate its adverse effect by implementing practical solutions that minimize the increase in process complexity and operational costs. Few examples in this regard are the use of membranes with different surface properties [12] and morphologies [13], high shear stress induced by ultrasonic cavitation [14], surface cleaning through chemical agents [15] or intermittent backflushing [16]. However, the last two methods require an interruption of the normal operation process and can damage the porous medium. Furthermore, dynamics techniques such as rotating or vibrating modules and hydrodynamic techniques such as air sparging, dean vortices, or pulsed flow were also employed [17]. In this panorama, pulsed-hydrodynamics methods used to generate the unsteady flow have proven to be cost-effective, easily implementable, and helpful in improving the permeate flux in all types of membrane applications relative to steady-state [18]. In this regard, Jaffrin has obtained a filtrate 40% higher for a frequency of 2 Hz [19], the paper of Beltram et al. provides an increase of 60% in the range between 7.2 and 11.7 Hz [20] and for two other works the flux enhancement is 45 and 68% respectively at 1 Hz [21, 22]. Nonetheless, dimensional frequencies are used for such studies and other experimental research [23, 24], providing results of no general validity and only of relative support for understanding the physical mechanisms involved.

The work presented in this Chapter aims to overcome this knowledge gap through experiments conducted under well defined and well controlled flow dynamic conditions and the use of dimensionless quantities. The signal frequencies were chosen within limits described in the paper of Papadopoulos and Vauros [25] for four different regimes, namely Low, Intermediate, High and Very High and the wave amplitudes Ac (i.e. the ratio between the amplitude of the pulsed wave and the mean flow velocity) were chosen following the guidelines of Binder et al. [26]. As they have confirmed that for a value of $Ac < 1$, belonging to the current-dominated regime, the amplitude slightly affects the change in the flow properties, small wave amplitudes have been used in this work to minimize the stress-induced on the membrane and system.

The paper is organized as follows: Section 4.3 describes the hydraulic facility used for assessing the membrane performance under different imposed flows; Section 4.4 presents the equipment and experimental methodology adopted for the filtration tests; Section 4.5 reports and describes the results coming for both, steady and pulsed feed-flows conditions and section 4.6 is devoted to the primary outcomes of the present work.

4.3 Experimental Methods

The filtration tests were carried out in the large-scale, recirculating facility for membrane fouling investigations at the Hydraulics Laboratory of Politecnico di Torino (Figure 4.1).

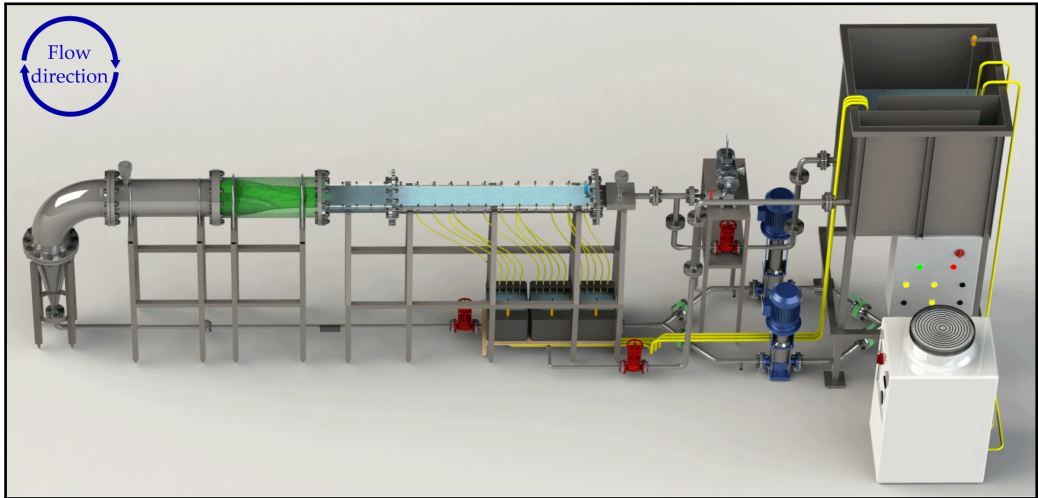


Fig. 4.1 Rendering of the hydraulic facility.

The system used for the experimental campaign is the one presented in detail in Chapter 1. Briefly, it was made with the following objectives:

- (i) Study fouling reduction induced by pulsed flows under controlled fluid-dynamic conditions;
- (ii) Replicate industrial flows using non-dimensional quantities to achieve kinematic and dynamic similarity.

For these reasons, particular attention has been paid to the fluid-dynamic components' geometries to obtain a fully developed flow within the measurement section. A key element in this sense is the flow conditioning unit, consisting of a stilling chamber and a fluid-dynamic convergent which allows, through a gradual reduction of the cross-section area, a progressive re-acceleration of the flow to avoid boundary layer separation and undesired eddies within the test section. The

latter is a rectangular channel (1.45 m long, 0.2 m wide and 0.01 m thick) entirely made of plexiglass to allow for flow measurements with optical techniques and evaluation of membrane surface alteration and is composed of two parts. The upper one is smooth and impermeable, and the lower one changes according to the test types. Smooth and impermeable for flow-characterization tests (herein called channel flow configuration) or with a special housing to accommodate a rigid stainless porous medium providing support for different types of flat-sheet membrane for filtration tests (herein called membrane configuration). In this case, the permeate from different locations along the flow direction is collected in three small trays underneath the cell unit to check for spatial uniformity of filtration rates. When a prefixed level is reached, they are automatically emptied into the 1 m³ main tank downstream of the system used to generate the pulsed flow (electric motor plus a rotating piston) to ensure a constant volume during the test.

The experimental conditions in terms of average pressure and flow regime (laminar transition or turbulent) within the test section are obtained respectively by means of the back-pressure valve, located at the end of the feed line, and by the coupled regulation of pump frequency, delivery and by-pass valves in order to control the amount of flow in each branch. For each test, the data regarding flow rate, pressure, levels within the collecting trays and temperature (kept constant through a 5 kW chiller) are acquired at the desired frequency and analysed. Further information about the design criteria of the main components (flow conditioning unit, test section and pulsating flow system), flow dynamics operation principle, investigable experimental conditions and details about the instrumentation used for measurement and data acquisition are described in the previous work "New Facility for Membrane Fouling Investigations under Customizable Hydrodynamics: Validation and Preliminary Experiments with Pulsating Cross-Flow" [27] and in the related supplementary material.

4.4 Experimental Procedure and Measuring Equipment

Filtration tests were carried out in stationary and pulsed feed-flow conditions. A periodic signal, proper of current-dominated regime (i.e. ratio $Ac = \text{velocity oscillation}/\text{mean centerline velocity}$ is < 1) was superimposed to the mean flow. For both the conditions the feed solution was prepared in order to replicate the composition and amount of total suspended solids (TSS) encountered in the nearby Po River [28, 29], which is currently the main water resource for the city of Turin and whose water will soon be treated with a new ultrafiltration plant by the local water supplier. To obtain the required concentration c of 27 ppm, 5 grams of kaolin ($D_{50} = 1.5 \mu\text{m}$) and 10 grams of green clay ($D_{50} = 0.2 \mu\text{m}$) were added to 555 l of tap water as colloidal foulants. A new polyethersulfone (PES) Synder-LY ultrafiltration flat-sheet membrane with a nominal area of 0.28 m^2 , permeance between 80 and $123 \text{ lm}^{-2}\text{h}^{-1}\text{bar}^{-1}$ and a molecular weight cut-off (MWCO) of 100,000 Da was mounted in the housing section for each test. An average Re numbers of ≈ 4000 , achieved from the Reynolds similarity with flows within others membrane plants [30, 31], was maintained with a constant fluid temperature of $16.5 \pm 0.5 \text{ }^\circ\text{C}$ and a mean pressure of 1.5 bar.

As mentioned in the introduction, dimensionless quantities were used to give results a general validity through the understanding of the physics mechanisms underpinning fouling reduction with hydrodynamic techniques and thus facilitate the design process of new equipments. The dimensionless frequency $\omega^+ = 2\pi f v / u_*^2$ (or equivalently $ls^+ = \sqrt{2/\omega^+}$) was used as an indicator of the pulsed-flow frequency. In contrast, the dimensionless parameter $\Gamma = V/U$ and $T^* = T_w u_* / h$ (where T_w is the time period of the imposed oscillation and h the semi-height of the channel) were used to assess the effect of the applied periodic disturbance. All the experimental conditions investigated, including the steady-state as benchmark case and all the various pulsed flow are shown in Table 4.1.

In order to study the effects of the different unsteady flow regimes: ii. Low-frequency, iii. Intermediate-frequency, iv. High-frequency and v. Rapid oscillation or Very-High frequency regime (indicated in the table with increasing Roman num-

Table 4.1 Summary of all experimental conditions for filtration tests. The columns indicate: the flow regime, the mean Reynolds number, $Re = U/h/\nu$, the mean pressure, p , the suction coefficient, $\Gamma = V/U$, the dimensional frequency, f , the non-dimensional frequency, $\omega^+ = 2\pi fV/u_*^2$ or $ls^+ = \sqrt{2}/\omega^+$, the dimensionless propagation length, $T^* = T_w u_*^2/h$ and the ratio between the velocity oscillation and the average velocity in the mid height of the channel, Ac . The limits of each flow regime are written in blue

Test Name	Symbol	Regime	Re [-]	p [bar]	Γ [10 ⁻⁴]	f [Hz]	ω^+ [-]	ls^+ [-]	T^* [-]	Ac [%]
S-4_1.5	■	Steady	3983	1.52	1.63	-	-	-	-	-
P-4_1.5_2.5_LA	▼	ii.	3974	1.51	1.84	0.09	0.0025 < 0.005	28.2 > 20	16.67	< 5
P-4_1.5_12.8_LA	▲	iii.	3969	1.5	1.79	0.46	0.005 < 0.0128 < 0.02	20 > 12.5 > 10	3.26	< 5
P-4_1.5_35.5_LA	◆	iv.	3952	1.5	1.83	1.27	0.02 < 0.0355 < 0.04	10 > 7.5 > 7.1	1.18	< 5
P-4_1.5_62.8_LA	●	v.	3957	1.51	1.56	2.25	0.04 < 0.0628	7.1 > 5.6	0.67	< 5
P-4_1.5_62.8_HA	●	v.	4005	1.51	1.84	2.25	0.04 < 0.0628	7.1 > 5.6	0.67	30

bers as the frequency increases) on the membrane fouling rates, non-dimensional frequency within the limits of each of the four intervals (i.e. for the entire experimental campaign $0.0025 < \omega^+ < 0.0628$) was imposed by means of the pulsed flow system. Furthermore the influence of the amplitude was evaluated for a fixed dimensionless frequency ($\omega^+ = 0.0628$). In this regard, since the installed ultrasound flow meter (AcquaTrans™ AT600) with two sensors does not allow the correct resolution of the signal due to the high sensibility to the variation of the velocity profile, the characterisation was made by the use of the pressure one. Maintaining a rod insertion depth k equal to 13.3 cm that produces a symmetrical pressure variation around the mean value and varying the rod vs. elbow insertion angle (see the previous work of Bert et al. [27] for an explanation of the functioning of the system used for the pulsed flow) two different conditions namely high amplitude (HA) with $Ac = 30\%$ and low amplitude (LA) with $Ac < 5\%$ were obtained. For the latter condition, a small value of the Ac ratio was adopted to minimise the stress induced respectively on membrane and on the whole system. In order to appreciate a significant reduction in the filtration rate over time, test conditions were maintained for 20 h and a final value of the suction parameter Γ in the range between 1.56×10^{-4} and 1.84×10^{-4} was obtained for all the applied conditions.

In addition, membrane surface variation was assessed by analysing photos acquired with a Canon EOS 700 camera controlled with digiCamControll software. The camera was placed horizontally above the test section at a sufficient distance to capture the framing area its whole extent, and constant light conditions for the entire test duration were ensured by means of 11 lights (600 Lm each) placed in a fixed position inside a dark room suitably constructed around the test section. For all the images acquired with a time interval of 15 minutes, after an initial white calibration, the percentage variation of the predominant chromatic band (yellow) was calculated locally with respect to their initial value. This procedure made it possible to investigate, for the whole-cell unit, the spatial and temporal chromatic variation of the membrane surface induced by colloidal fouling.

4.5 Results

This section provides the result of the filtration test reported in Table 4.1 that have been carried out with a mean Re numbers \approx to 4000 and an average pressure of 1.5 bar. For all the experimental conditions, the filtrate corresponding to each third of the membrane area along the direction of the motion is conveyed into the respective tray underneath the housing cell (identified as "up", "mid", "down") that are automatically emptied when a predefined value is reached. The integral of those values gives the respective flux of each portion and hence information about the spatial variation of the filtration rate, which depends on both the thickness and spatial distribution of the fouling layer [32].

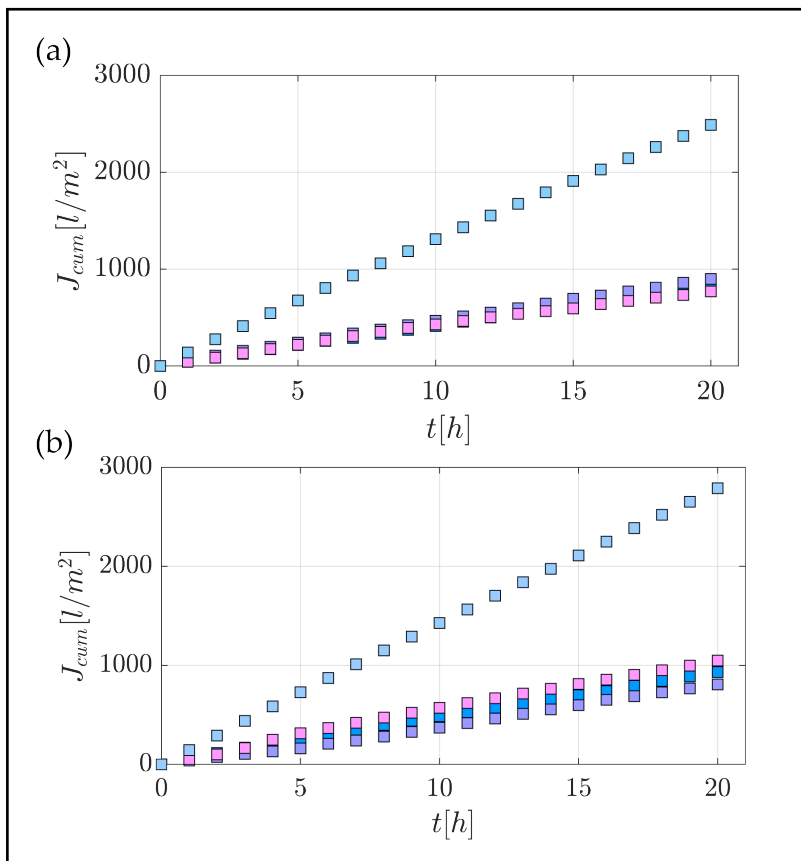


Fig. 4.2 Total water flux and measured from the individual portions: (a) Test S-4_1.5; (b) Test P-4_1.5_2.5_LA. In both panels, light blu, lavender and pink squares refer to up, mid and down collection tanks respectively and azure squares refer to cumulative flux.

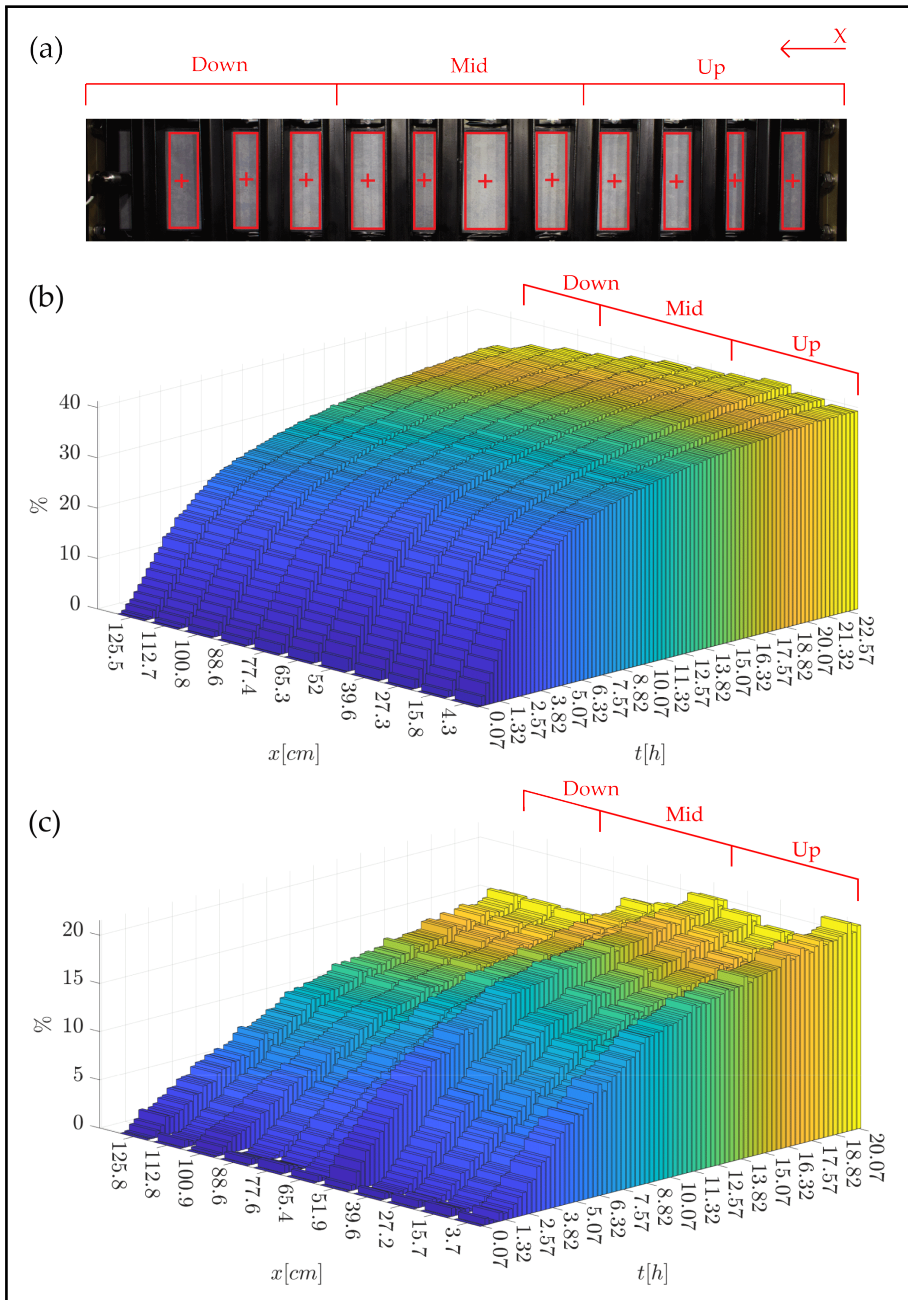


Fig. 4.3 Photo of the entire membrane taken with the overhead camera (Panel (a)) and percentage variation of the membrane color (yellow band) measured at different longitudinal positions along the membrane surface as a function of time for steady ((b) Test S-4_1.5) and pulsed flow conditions ((c) Test P-4_1.5_2.5_LA).

In this regard Figure 4.2a shows that in steady conditions, slight cumulative variations at a fixed time were obtained for each portion, providing nearly uniform pattern depositions over the entire membrane. Under pulsed feed-flow conditions, however, a more appreciable variation of the water flux, imputable to the change in the hydrodynamics conditions (feed composition and membrane type are the same for all tests) is observed between the three membrane areas (Figure 4.2b).

Further and more detailed information about the uniformity and temporal evolution of the pattern deposition, and hence of the filtration rate, can be obtained from the analysis of the membrane surface as done previously for both steady [33, 34] and pulsed-flow conditions [35], by others researchers. In this case, the evolution of the fouling rate was assessed from the images acquired from the overhead camera with a time interval of 15 min. Figure 4.3a provides a snapshot of the whole test section for which, after an initial white balance, the chromatic variation of the predominant band in the measured spectrum (yellow band) was assessed for the 11 membrane areas inside the red boxes (note that the full optical access is prevented by the reinforcements used to avoid water leakage).

This analysis, although semi-quantitative, confirms the spatial and temporal differences between steady and pulsed conditions. For the former (Test S-4_1.5) panel b of Figure 4.3 shows that the fouling behaviour and hence the flux rate varies moderately along the entire length of the channel at any point in time with differences between 2 and 8.5 % and that the major detrimental effect of fouling occurs in the initial phase. For the latter (Test P-4_1.5_2.5_LA) panel c of Figure 4.3 shows a higher difference in the behaviour between the different areas, a slower initial deposition rate and a lower value of "yellowing" at the end of the test compared to the steady case. In particular, the differences at any point in time between the steady and the pulsed case are contained between 1.45 and 6.9%, but for a maximum final change in the yellow band of about 21% (i.e. about half of that obtained for the stationary case). It is important to observe that the lower and less uniform fouling rate, deduced from the image analysis in reference to the pulsed flow conditions, agrees with results obtained from the filtrate measurement. That is, a more significant variation in the permeate flux inside the collection tanks and a higher total flux J_{cum} at the end of the test (i.e. 2489 l/m² for steady

conditions vs. 2788 l/m² for the pulsed flow with a non-dimensional frequency ω^+ of 0.09, equivalent roughly to a 12% increase in recovered water).

After preliminarily observing the beneficial effect of pulsed flow conditions in regards to the fouling mitigation, further tests were conducted to explore the influence of different frequencies and amplitude of the imposed wave. The first assessment in this sense can be made from the curves of the total water flux J_{cum} vs. time presented in Figure 4.4 as follow:

- (i) In Panel (a), the results for the four non dimensional frequency, proper of the different pulsed flow regimes, are compared with the steady condition (orange squares);
- (ii) In Panel (b), the same total non-dimensional water flux obtained for the steady condition is compared with two cases characterized by the non dimensional frequency $\omega^+ = 0.0628$ and $Ac < 5\%$ and equal to 30% respectively.

A first glance at both families of curves reveals that for all the applied conditions, the initial water flux lies between the values of performance indicated by the manufacturer, and a decrease in permeate is evident for all tests also if the steady-state flux is not reached. At the end of the experiments, the suction coefficient Γ is within the range $1.56 \div 1.84 \times 10^{-4}$ and except for the test P-4_1.5_62.8_LA, an increase is observed compared to the stationary case. However, it seems probable that the inconsistency of this result can be explained by the variance in the performance of the specific membrane sample rather than by the imposed perturbations.

In order to highlight the effects of different hydrodynamic conditions, the same results are presented in dimensionless form in Figure 4.5, dividing each trend by his value at the first hour. The results are important from an experimental point of view mainly for two reasons. Firstly, Panel (a) shows a reduction in the fouling rate when a periodic wave with a dimensionless frequency belonging to the ii. and iii. regimes of Table 4.1 is applied. For those conditions, the final normalised flux of 0.9 indicates that the fouling-related flux reduction is half of that associated with the steady case. On the contrary, flows belonging to the fourth

and fifth frequency range does not seem to lead to an improvement in system performance. Secondly Panel (b) shows that a change in the wave amplitude make no appreciable differences in regard to the fouling reduction.

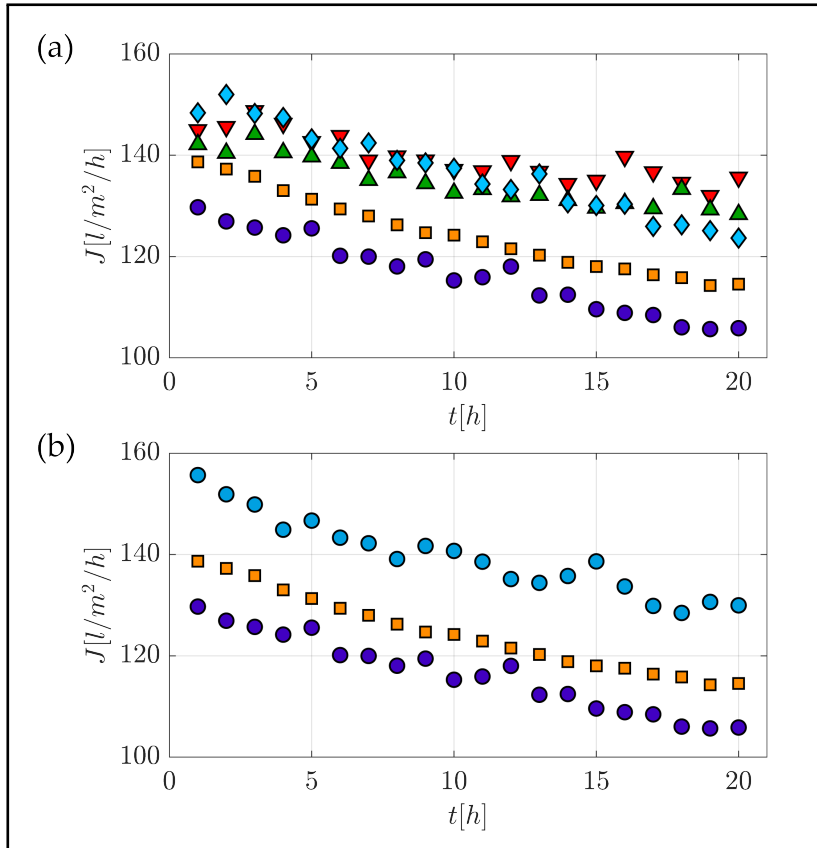


Fig. 4.4 Dimensional filtrate flux vs. time: **(a)** Steady vs. low amplitude pulsating flow for different adimensional frequencies; **(b)** Steady vs. low and high amplitude pulsating flow at the same adimensional frequency. Symbols and experimental conditions for all the tests are reported in Table 4.1.

The apparent improvement in performance in terms of flux rate within the system discussed above can be explained by the following important points:

- (i) Applying pulsed flow in a specific dimensionless frequency range seems to change the balance between the forces responsible for the particle deposition phenomena. That is equilibrium between convective forces that tend to

attract foulants near the membrane surface and the forces, mainly shear-induced diffusion and lift for colloid of that size [36], that act in the opposite direction. As a consequence, the rapid initial drop of the permeate flux induced in an early stage by the blockage of membrane pores and at a later stage by cake formation and enhancement [37] are slowed down;

- (ii) With pulsed flow conditions, the variation in the instantaneous flow rate at the membrane interface results in additional vorticity within the boundary layer that varies with time and is controlled by the dimensionless frequency ω^+ or ls^+ . These turbulent shear waves propagate from the wall into fluid with speed proportional to the friction velocity u^* [38], and the distance and extent of his effect can be explained through the use of the dimensionless outer scaling parameter T^* . In their paper, He and Jackson [39] became less than 10 the pulsating period was so short that the unsteadiness imposed on the mean flow could not be transmitted within any cycle from the wall to the region where turbulent production is significant, and therefore, the quantity of additional turbulence is attenuated. Furthermore, they state that if T^* is greater than unity, the imposed unsteadiness will affect the entire flow. Both the observations can be applied to the results of our experiments reported in Table 4.1 that highlight a higher production of additional turbulence and a consequent radial propagation outward to the centre of the channel for the second and third regimes (i.e. for the Low-frequency and Intermediate-frequency regime ls^+ are respectively 28.2 and 12.5 while T^* are equal to 16.67 and 3.26). Based on the above, it can therefore be said that the mitigation of fouling observed under these conditions is probably attributable to an increase in the probability of particles being entrained and retained in the feed rather than deposited on the membrane surfaces. Furthermore cannot be excluded that the additional vorticity may increase the membrane's "cleaning" effect against the particulate matter" that tends to settle on its surface, especially in the early stages of the test.
- (iii) For the current-dominated flows considered in this work, the variation in the hydrodynamic behaviour and hence the fouling ratio is primarily controlled by the dimensionless frequency ω^+ rather than by the amplitude ratio Ac

(i.e. 5 % to 30 %). In this sense, a small value of the amplitude of the imposed perturbation seems sufficient to achieve a lower flux reduction. This observation is supported by other pulsating turbulent channel flow studies with current-dominated conditions [40, 41].

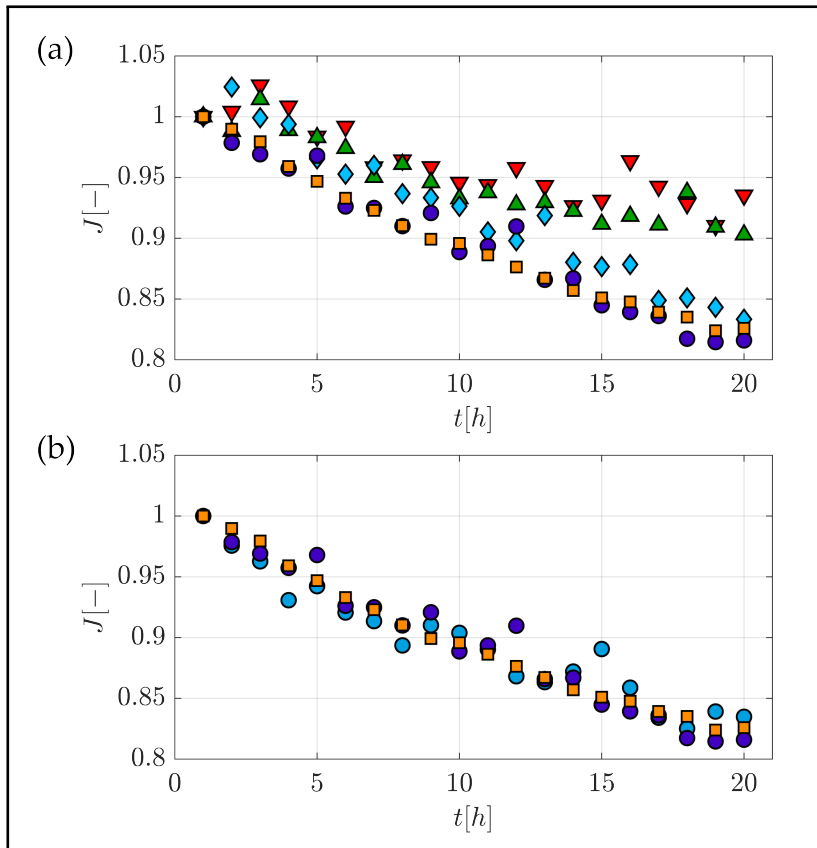


Fig. 4.5 Non-dimensional filtrate flux vs. time: **(a)** Steady vs. low amplitude pulsating flow for different adimensional frequencies; **(b)** Steady vs. low and high amplitude pulsating flow at the same adimensional frequency. Symbols and experimental conditions for all the tests are reported in Table 4.1.

4.6 Concluding Remarks

In this work, the application of a current-dominated pulsed flow to mitigate the detrimental fouling phenomenon was experimentally investigated under carefully controlled flow dynamic conditions. The spatial and temporal variation of the fouling rate was investigated for steady and pulsed-flow conditions with a dimensionless frequency ω^+ equal to 0.09 and an amplitude ratio Ac of 5%. Firstly the permeate flux of three different areas, namely "up", "mid" and "down" along the direction of motion, was monitored for all the test duration. Secondly, the surface variation of the membrane at any point in space and time was assessed through the chromatic change inferred from images. Even if the second gives only qualitative results, both methods used have shown a less uniform deposition pattern and a lower tendency to fouling for the pulsed-flow case. As a consequence of the decrease in the clogging speed, an higher water flux was obtained after 20 h. Furthermore, the effect of changing the imposed frequency or wave amplitude was investigated. Results demonstrate that for a value of the dimensionless parameter ω^+ within the ii. and iii. regimes, the fouling-related flow reduction is half of that associated with the steady case. On the contrary, no appreciable effect was found for the iv.th and v.th frequency range, also varying the value of Ac (from 5 % to 30 %). What has been observed can be explained with the following statement:

- (i) Probably under some pulsed conditions, there is a change in the equilibrium between the forces that tend to attract the foulants to the membrane surface or turn them away from it with respect to the steady case;
- (ii) For the lower and Intermediate frequency regimes, the instability that arises at the wall for each cycle reaches the zone of greatest turbulence production before being attenuated. Thus higher additional turbulence compared to other cases of pulsed flow was produced;
- (iii) The higher propagation distance associated with these lower frequencies enhance the probability of removed particles to be retained within the feed flow rather than deposited on the membrane sheet.

The dimensionless frequency and propagation length well capture these physical behaviours. The former controls wall effects while the latter provide informations about the distance and intensity at which they propagate with a velocity of the order of u^* . In this sense experiment results, in line with previous works, display a drop in the fouling rate when ls^+ and T^* are greater of about 10 and 1 respectively. On the contrary the parameter Γ used for assess the variation of the flux rate seems to suffer for the slight initial variance in membrane permeability. Finally, although the amplitude variation was studied for only one frequency, the preliminary result and those present in literature for current-dominated flows seem to prove the low Ac influence on fouling mitigation. This result, if confirmed by future tests, is of importance because it would limit the stresses induced on the system and membrane, necessary to keep it cleaner. Future work should focus on the fluid-dynamic study of flow statistics for those conditions that provide a substantial improvement in system performance. In this respect, the authors claim that Particle Image Velocimetry (PIV) measurements will help to gain a better understanding of the physics of the problem.

References

- [1] S. A. Aktij, A. Taghipour, A. Rahimpour, A. Mollahosseini, and A. Tiraferri, “A critical review on ultrasonic-assisted fouling control and cleaning of fouled membranes,” *Ultrasonics*, vol. 108, p. 106228, 2020.
- [2] S. P. Nunes, P. Z. Culfaz-Emecen, G. Z. Ramon, T. Visser, G. H. Koops, W. Jin, and M. Ulbricht, “Thinking the future of membranes: Perspectives for advanced and new membrane materials and manufacturing processes,” *Journal of Membrane Science*, vol. 598, p. 117761, 2020.
- [3] C. Charcosset, “Classical and recent applications of membrane processes in the food industry,” *Food Engineering Reviews*, vol. 13, no. 2, pp. 322–343, 2021.
- [4] C. Z. Liang, T.-S. Chung, and J.-Y. Lai, “A review of polymeric composite membranes for gas separation and energy production,” *Progress in Polymer Science*, vol. 97, p. 101141, 2019.
- [5] S. P. Adiga, C. Jin, L. A. Curtiss, N. A. Monteiro-Riviere, and R. J. Narayan, “Nanoporous membranes for medical and biological applications,” *Wiley Interdisciplinary Reviews: Nanomedicine and Nanobiotechnology*, vol. 1, no. 5, pp. 568–581, 2009.
- [6] N. C. Darre and G. S. Toor, “Desalination of water: a review,” *Current Pollution Reports*, vol. 4, no. 2, pp. 104–111, 2018.
- [7] E. Obotey Ezugbe and S. Rathilal, “Membrane technologies in wastewater treatment: A review,” *Membranes*, vol. 10, no. 5, 2020.

- [8] Fortune Business Insights Pvt. Ltd., “Membrane Market Size, Share & COVID-19 Impact Analysis, By technology (RO/FO, UF, NF, MF and Others), By application (Water & Wastewater Treatment, Food & Beverage, Gas Separation, and Others), and Regional Forecast 2022-2029.” <https://www.fortunebusinessinsights.com/membranes-market-102982>, 2022. [Online; accessed 28-April-2022].
- [9] R. W. Field, D. Wu, J. A. Howell, and B. B. Gupta, “Critical flux concept for microfiltration fouling,” *Journal of membrane science*, vol. 100, no. 3, pp. 259–272, 1995.
- [10] X. Shi, G. Tal, N. P. Hankins, and V. Gitis, “Fouling and cleaning of ultrafiltration membranes: A review,” *Journal of Water Process Engineering*, vol. 1, pp. 121–138, 2014.
- [11] M. El Batouti, N. F. Alharby, and M. M. Elewa, “Review of new approaches for fouling mitigation in membrane separation processes in water treatment applications,” *Separations*, vol. 9, no. 1, p. 1, 2021.
- [12] W. S. Ang, S. Lee, and M. Elimelech, “Chemical and physical aspects of cleaning of organic-fouled reverse osmosis membranes,” *Journal of Membrane Science*, vol. 272, no. 1, pp. 198–210, 2006.
- [13] E. M. Vrijenhoek, S. Hong, and M. Elimelech, “Influence of membrane surface properties on initial rate of colloidal fouling of reverse osmosis and nanofiltration membranes,” *Journal of membrane science*, vol. 188, no. 1, pp. 115–128, 2001.
- [14] M. Elimelech, Xiaohua Zhu, A. E. Childress, and Seungkwan Hong, “Role of membrane surface morphology in colloidal fouling of cellulose acetate and composite aromatic polyamide reverse osmosis membranes,” *Journal of Membrane Science*, vol. 127, no. 1, pp. 101–109, 1997.
- [15] F. Zamani, J. W. Chew, E. Akhondi, W. B. Krantz, and A. G. Fane, “Unsteady-state shear strategies to enhance mass-transfer for the implementation of ultrapermeable membranes in reverse osmosis: A review,” *Desalination*, vol. 356, pp. 328–348, 2015. State-of-the-Art Reviews in Desalination.

- [16] M. Bagheri and S. A. Mirbagheri, "Critical review of fouling mitigation strategies in membrane bioreactors treating water and wastewater," *Biore-source Technology*, vol. 258, pp. 318–334, 2018.
- [17] M. Y. Jaffrin, "Hydrodynamic techniques to enhance membrane filtration," *Annual Review of Fluid Mechanics* *jaffrin2012hy*, vol. 44, pp. 77–96, 2012.
- [18] T. Kennedy, R. Merson, and B. McCoy, "Improving permeation flux by pulsed reverse osmosis," *Chemical Engineering Science*, vol. 29, no. 9, pp. 1927–1931, 1974.
- [19] M. Jaffrin, "Enhancement of plasma filtration in hollow fiber filters by pulsatile blood flow," *Life Support Syst*, vol. 2, pp. 207–210, 1984.
- [20] C. Bertram, M. Hoogland, H. Li, R. Odell, and A. Fane, "Flux enhancement in crossflow microfiltration using a collapsible-tube pulsation generator," *Journal of membrane science*, vol. 84, no. 3, pp. 279–292, 1993.
- [21] E. Spiazzi, J. Lenoir, and A. Grangeon, "A new generator of unsteady-state flow regime in tubular membranes as an anti-fouling technique: A hydrodynamic approach," *Journal of membrane science*, vol. 80, no. 1, pp. 49–57, 1993.
- [22] B. Gupta, P. Blanpain, and M. Jaffrin, "Permeate flux enhancement by pressure and flow pulsations in microfiltration with mineral membranes," *Journal of Membrane Science*, vol. 70, no. 2, pp. 257–266, 1992.
- [23] A. Kastl, A. Präbst, F. Kiefer, M. Spinnler, T. Sattelmayer, *et al.*, "Colloidal fouling mitigation using pulsating flows in osmotic membrane processes," *Desalination and Water Treatment*, vol. 157, pp. 228–241, 2019.
- [24] *Overview of Membrane Science and Technology*, ch. 1, pp. 1–14. John Wiley & Sons, Ltd, 2004.
- [25] P. K. Papadopoulos and A. P. Vouros, "Pulsating turbulent pipe flow in the current dominated regime at high and very-high frequencies," *International Journal of Heat and Fluid Flow*, vol. 58, pp. 54–67, 2016.

- [26] G. Binder, S. Tardu, and P. Vezin, “Cyclic modulation of reynolds stresses and length scales in pulsed turbulent channel flow,” *Proceedings of the Royal Society of London. Series A: Mathematical and Physical Sciences*, vol. 451, no. 1941, pp. 121–139, 1995.
- [27] R. Bert, C. Manes, and A. Tiraferri, “New facility for membrane fouling investigations under customizable hydrodynamics: Validation and preliminary experiments with pulsating cross-flow,” *Membranes*, vol. 12, no. 3, p. 334, 2022.
- [28] V. Davide, M. Pardos, J. Diserens, G. Ugazio, R. Thomas, and J. Dominik, “Characterisation of bed sediments and suspension of the river po (italy) during normal and high flow conditions,” *Water research*, vol. 37, no. 12, pp. 2847–2864, 2003.
- [29] Arpa Piemonte, “Water quality in Torino (2009-2017).” http://webgis.arpa.piemonte.it/monitoraggio_qualita_acque/index.php?numcodice=001095, 2020. [Online; accessed 22-November-2021].
- [30] V. Gekas and K. Ölund, “Mass transfer in the membrane concentration polarization layer under turbulent cross flow: Ii. application to the characterization of ultrafiltration membranes,” *Journal of membrane science*, vol. 37, no. 2, pp. 145–163, 1988.
- [31] J. Nikolova and M. Islam, “Contribution of adsorbed layer resistance to the flux-decline in an ultrafiltration process,” *Journal of Membrane Science*, vol. 146, no. 1, pp. 105–111, 1998.
- [32] K. Martin, D. Bolster, N. Derlon, E. Morgenroth, and R. Nerenberg, “Effect of fouling layer spatial distribution on permeate flux: a theoretical and experimental study,” *Journal of membrane science*, vol. 471, pp. 130–137, 2014.
- [33] L. Fortunato, S. Bucs, R. V. Linares, C. Cali, J. S. Vrouwenvelder, and T. Leiknes, “Spatially-resolved in-situ quantification of biofouling using optical coherence tomography (oct) and 3d image analysis in a spacer filled channel,” *Journal of Membrane Science*, vol. 524, pp. 673–681, 2017.

- [34] C. Picioreanu, J. Vrouwenvelder, and M. Van Loosdrecht, “Three-dimensional modeling of biofouling and fluid dynamics in feed spacer channels of membrane devices,” *Journal of Membrane Science*, vol. 345, no. 1-2, pp. 340–354, 2009.
- [35] A. Kastl, E. Bar-Zeev, M. Spinnler, and T. Sattelmayer, “Impact of pulsating flows on particle deposition in forward osmosis with spacers,” *Journal of Membrane Science*, vol. 635, p. 119444, 2021.
- [36] C. Y. Tang, T. Chong, and A. G. Fane, “Colloidal interactions and fouling of nf and ro membranes: a review,” *Advances in colloid and interface science*, vol. 164, no. 1-2, pp. 126–143, 2011.
- [37] A. Abdelrasoul, H. D. Doan, and A. Lohi, “Fouling in membrane filtration and remediation methods,” 2013.
- [38] A. Scotti and U. Piomelli, “Numerical simulation of pulsating turbulent channel flow,” *Physics of Fluids*, vol. 13, no. 5, pp. 1367–1384, 2001.
- [39] S. He and J. Jackson, “An experimental study of pulsating turbulent flow in a pipe,” *European Journal of Mechanics - B/Fluids*, vol. 28, no. 2, pp. 309–320, 2009.
- [40] F. S. Tardu and G. Binder, “Wall shear stress modulation in unsteady turbulent channel flow with high imposed frequencies,” *Physics of Fluids A: Fluid Dynamics*, vol. 5, no. 8, pp. 2028–2037, 1993.
- [41] S. F. Tardu, G. Binder, and R. F. Blackwelder, “Turbulent channel flow with large-amplitude velocity oscillations,” *Journal of Fluid Mechanics*, vol. 267, pp. 109–151, 1994.

Chapter 5

Conclusions

It is the author's opinion that our current knowledge of flow properties pertaining to membrane systems is still limited and an improved understanding of such properties is highly required to mitigate issues related to fouling and clogging. This thesis provides the first step towards this goal.

The key outcomes obtained in the present work are summarised below for each objective listed in chapter 1:

Objective 1

"Design, build and validate an ad hoc facility devoted to investigating the clogging phenomenon related to membranes separation process in well-controlled flow dynamics conditions."

In Chapter 1, the experimental facility, designed and constructed to carry out experiments under representative flow conditions of membrane systems, is presented and its operational principles accurately discussed. Furthermore, particular attention was paid to describing the criteria adopted to achieve well-controlled fluid-dynamic conditions.

The system was then validated from a hydraulic standard point by means of a laser diagnostic technique. Velocity measurements at three streamwise positions provide evidence for the development of a so-called canonical channel flow behaviour (i.e. velocity statistics collapse very well with dataset presented in literature at Reynolds numbers) and the establishment of a uniform and fully-developed flow within the test section. Preliminary filtration tests, on the other hand, have brought to light two aspects: firstly, concerning the stationary flow conditions, excellent test repeatability and nicely uniform filtrate fluxes were obtained over the entire membrane area; secondly, a preliminary filtration test conducted with the same mean flow parameters (i.e. Reynolds number and driving pressure P) under pulsed-flow conditions shows the potential of hydrodynamics pulsations in reducing fouling effects compared to the steady case.

Objective 2

"To evaluate the effects of suction in channel flow turbulence as a means to explore how flow characteristics in membrane systems are affected when permeate fluxes are changed."

This objective was addressed mainly in Chapter 2. Results indicate that the maximum velocity in the centre of the channel (U_m) and the semi-height of the channel (h) work very well as scaling parameters for all velocity statistics pertaining to channel flows with suction. This represents an important outcome as it allows for an easy parametrization of the time averaged flow characteristics and to overcome issues related to the estimation of the friction velocity u^* , which is difficult for the case of wall suction. The comparison between velocity statistics between impermeable and wall suction conditions, shows that suction reduces the standard deviation of the longitudinal and wall-normal velocity fluctuations as well as their covariance independently of the value of the suction rate Γ . Moreover, suction effects are also felt in a reduction of the production term of the turbulent kinetic energy balance, while the dissipation term seems to be unaltered. Such evidence suggests that probably suction stabilises near-wall streaks and generates turbulence pertaining to a different self-sustained state independent of Γ . Surprisingly, only weak effects of suction are observed concerning the turbulent structure of flows as detected by means of quadrant analysis and two-point cross-correlation functions.

Objective 3

"To explore the effects of pulsating flow conditions on particle deposition during filtration experiments in membrane systems".

Objectives 3 were investigated in Chapter 3. Filtration tests were designed to keep pressure and Reynolds number constant while the frequency and amplitude of an imposed pulsating flow were imposed. A steady flow characterised by almost identical pressure and Reynolds number was used as benchmark for comparison of permeate fluxes. Results show that the pulsating flow amplitude has little effects on permeate fluxes. On the contrary, frequency plays a key role in reducing fouling and increasing the amount of permeate. Improved effects in this respect were obtained for the lowest investigated frequencies. This result was interpreted in terms of the following two quantities the dimensionless frequency ls^+ that controls the effect induced by the pulsed flow in the near-wall region and the dimensionless propagation length T^* that controls both the intensity and distance at which such

wall effects propagate. When those values are greater than 10 and 1, respectively, a drop in the fouling rate was observed.

Appendix A

New Facility for Membrane Fouling Investigations under Customizable Hydrodynamics: Validation and Preliminary Experiments with Pulsating Cross-Flow

Table A.1 Geometries and properties of the main hydraulic components.

Pipes							
DN	PN	ϕ_{est} [mm]	ϕ_{int} [mm]				
25	16	26.9	22.9				
32	16	42.4	38.4				
250	16	273	267				
Pumps							
Type	Power [kW]	Q_{min} [l/s]	H_{max} [m]	$Q_{70\%}$ [l/s]	$H_{Q_{70\%}}$ [m]	Q_{max} [l/s]	H_{min} [m]
Lowara - 5SV05	0.75	0.67	36.4	1.67	28.2	2.35	17.1
Lowara - 5SV23	4	0.67	168.9	1.67	129.6	2.35	78.2
Tanks							
Type		Capacity [l]					
Main tank		1000					
Collecting tanks		15					
Test section							
Length L [mm]	Height H [mm]	Width B [mm]	Thickness [mm]				
1450	10	200	25				

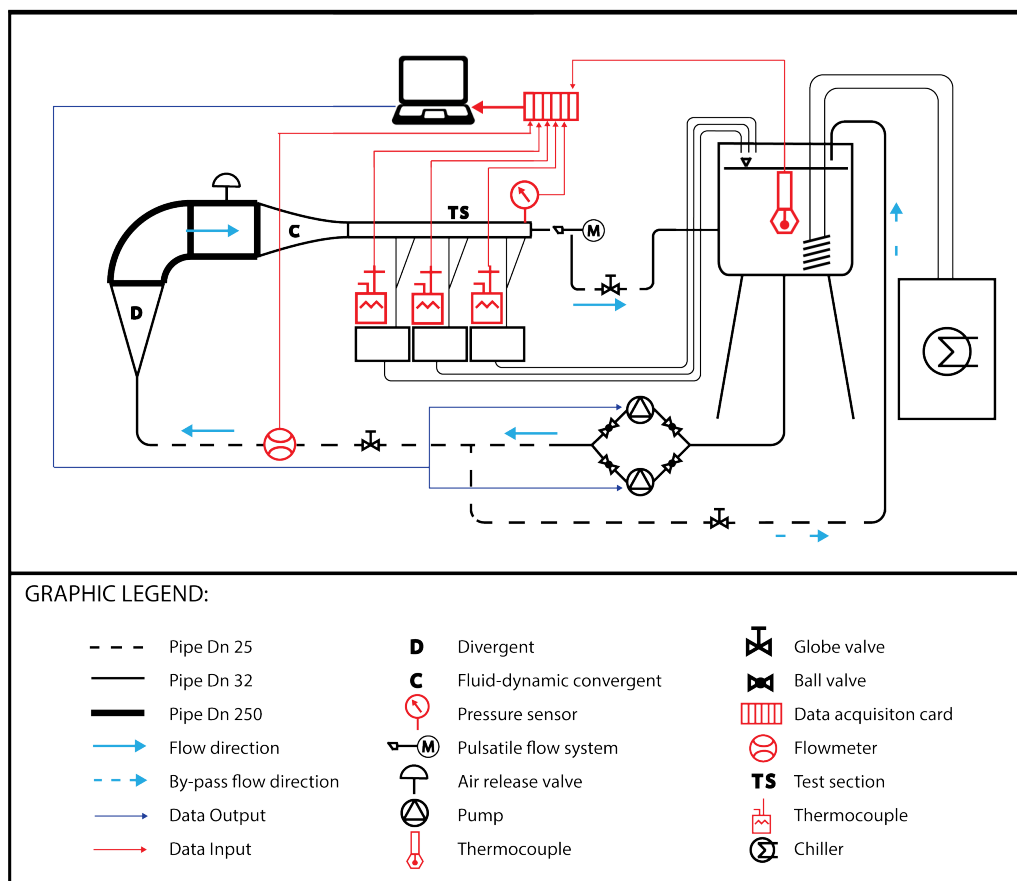


Fig. A.1 Pipes and instrumentation diagram (i.e. *P&ID* Diagram) of the overall facility.

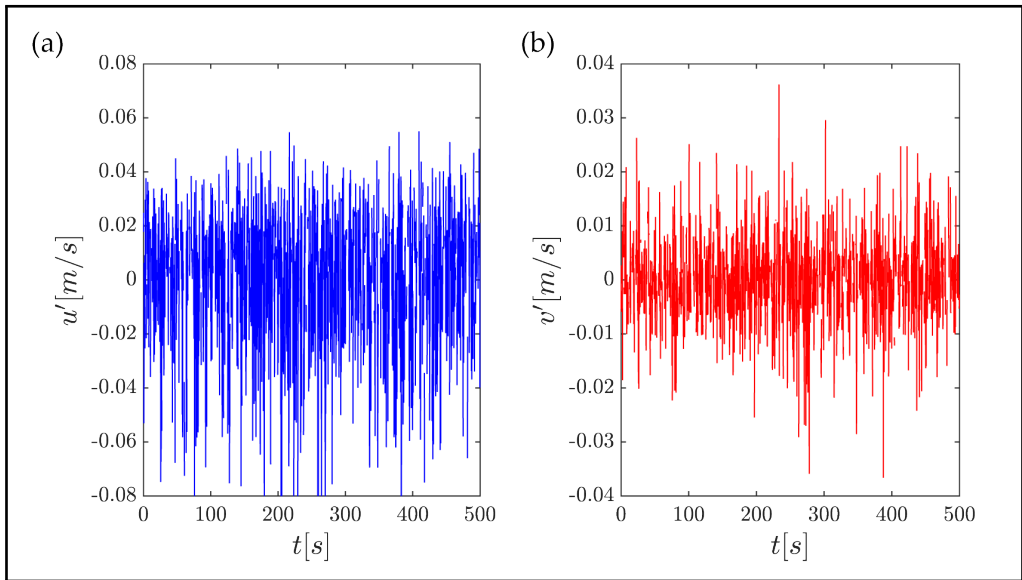


Fig. A.2 Time series of (a) the longitudinal u' and (b) wall-normal v' velocity fluctuations deduced by PIV measurement at the position F-2 and coordinates $x = 17$ mm and $y = 2.5$.

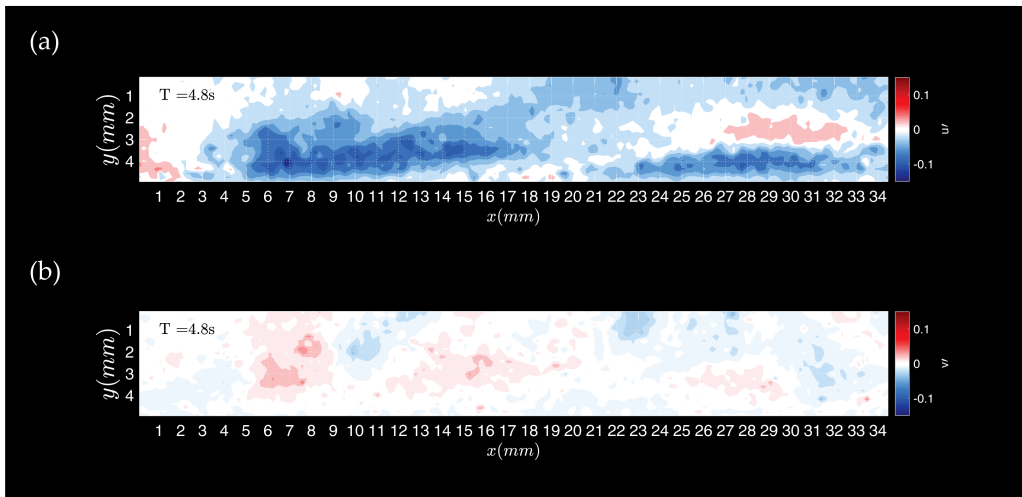


Fig. A.3 Contour plot of (a) the longitudinal u' and (b) wall-normal v' velocity fluctuations deduced by PIV measurement at the position F-2 at fixed time $T = 4.8$ s.

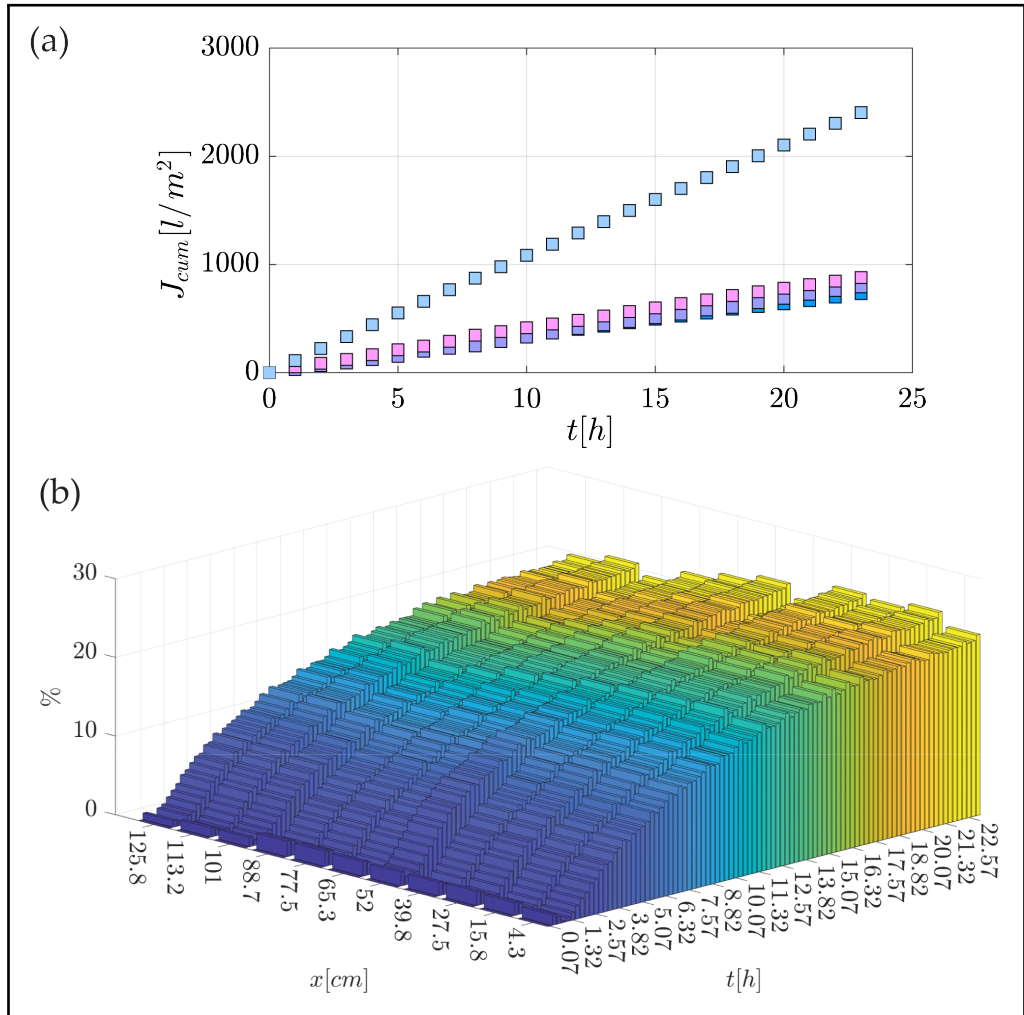


Fig. A.4 Results of filtration test S - 4.1: (a) Total water flux measured from the individual portions (where light blue, lavender and pink symbols refer to up, mid and down collection tanks respectively and azure squares refer to the cumulative flux) and (b) percentage variation of the membrane colour (yellow band) measured at different longitudinal positions along the membrane surface.

Appendix B

**Design drawings of the experimental
fluid-dynamic apparatus for fouling
reduction studies in membrane systems**

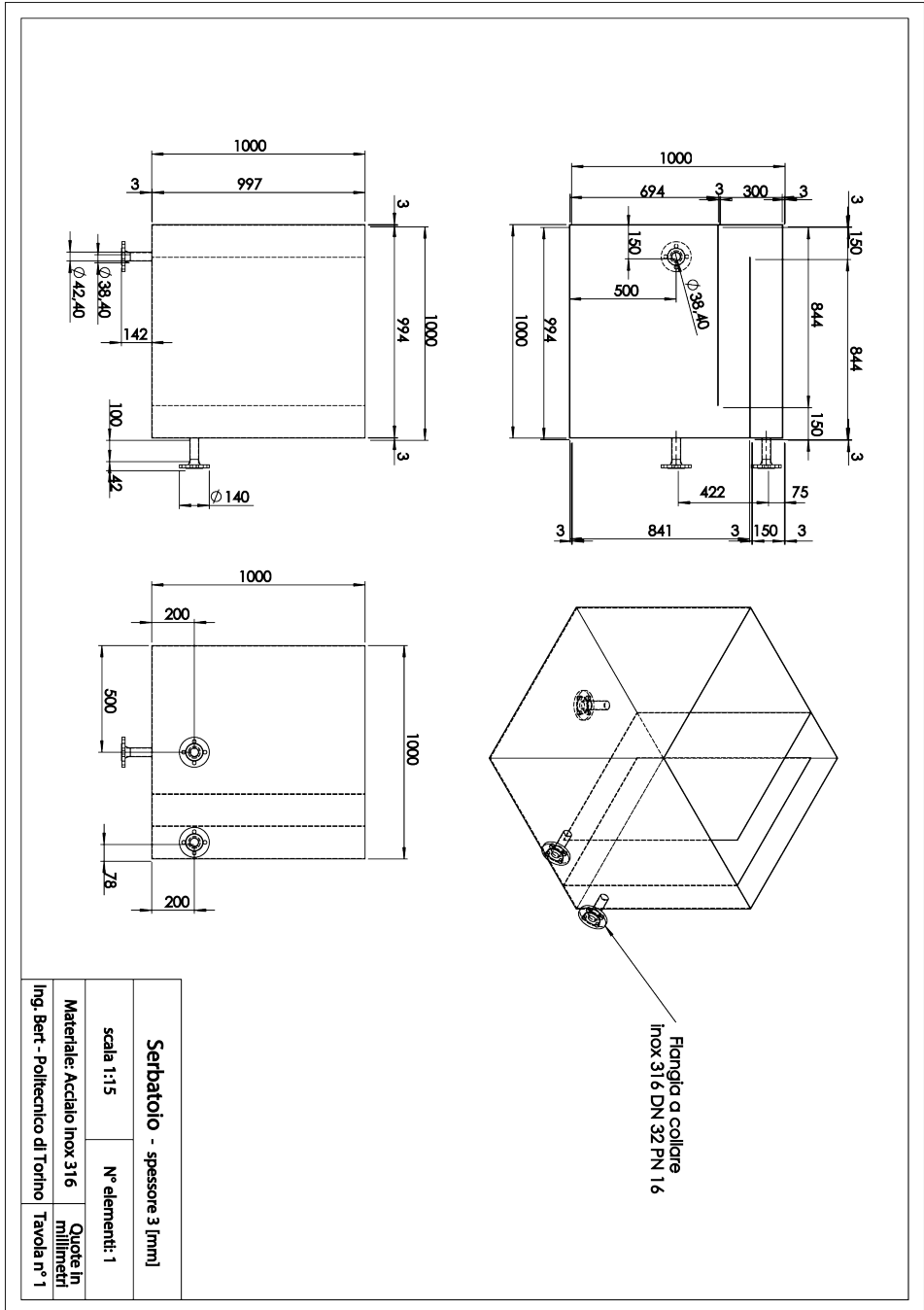


Fig. B.1 Main tank.

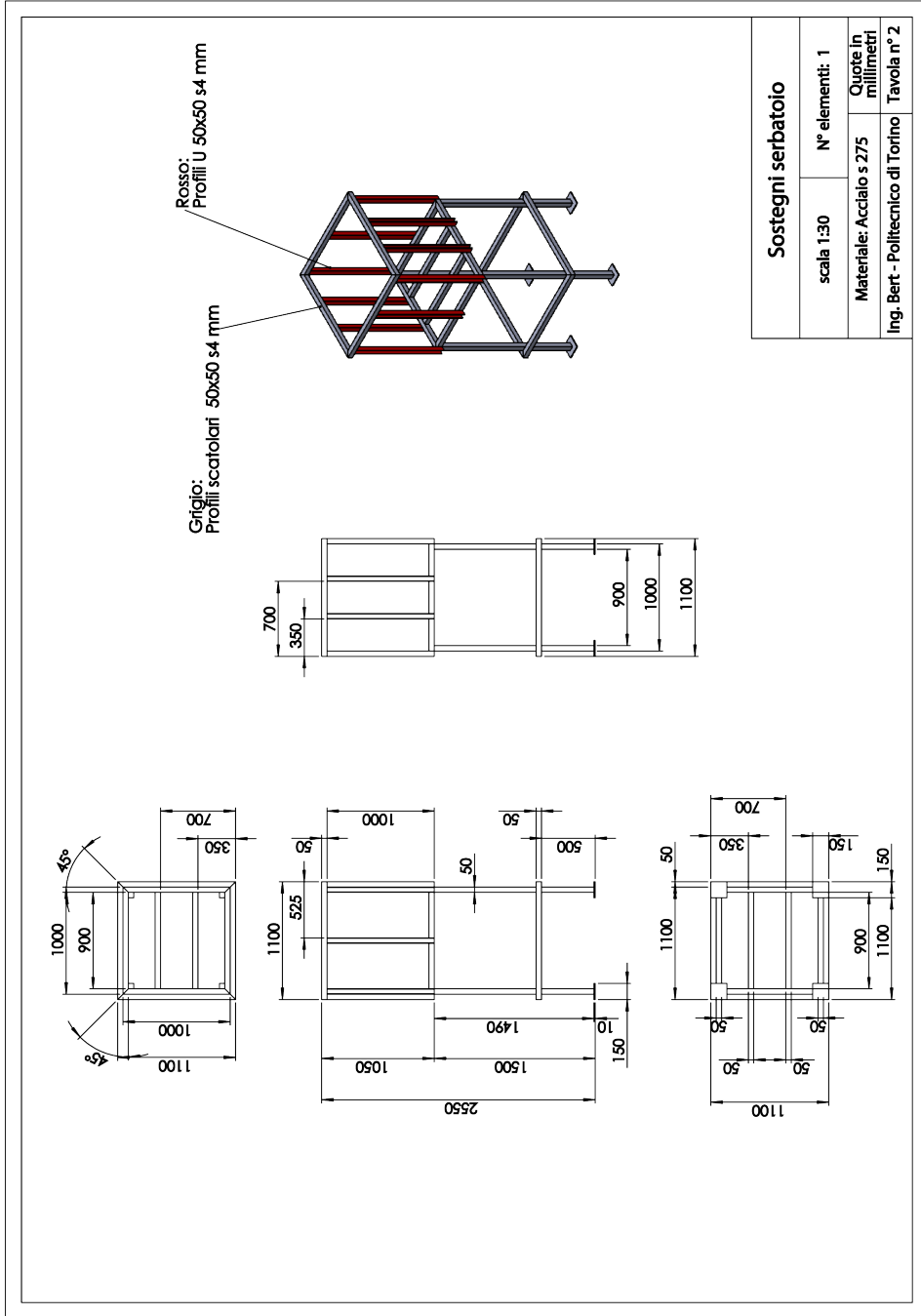


Fig. B.2 Supports of the main tank.

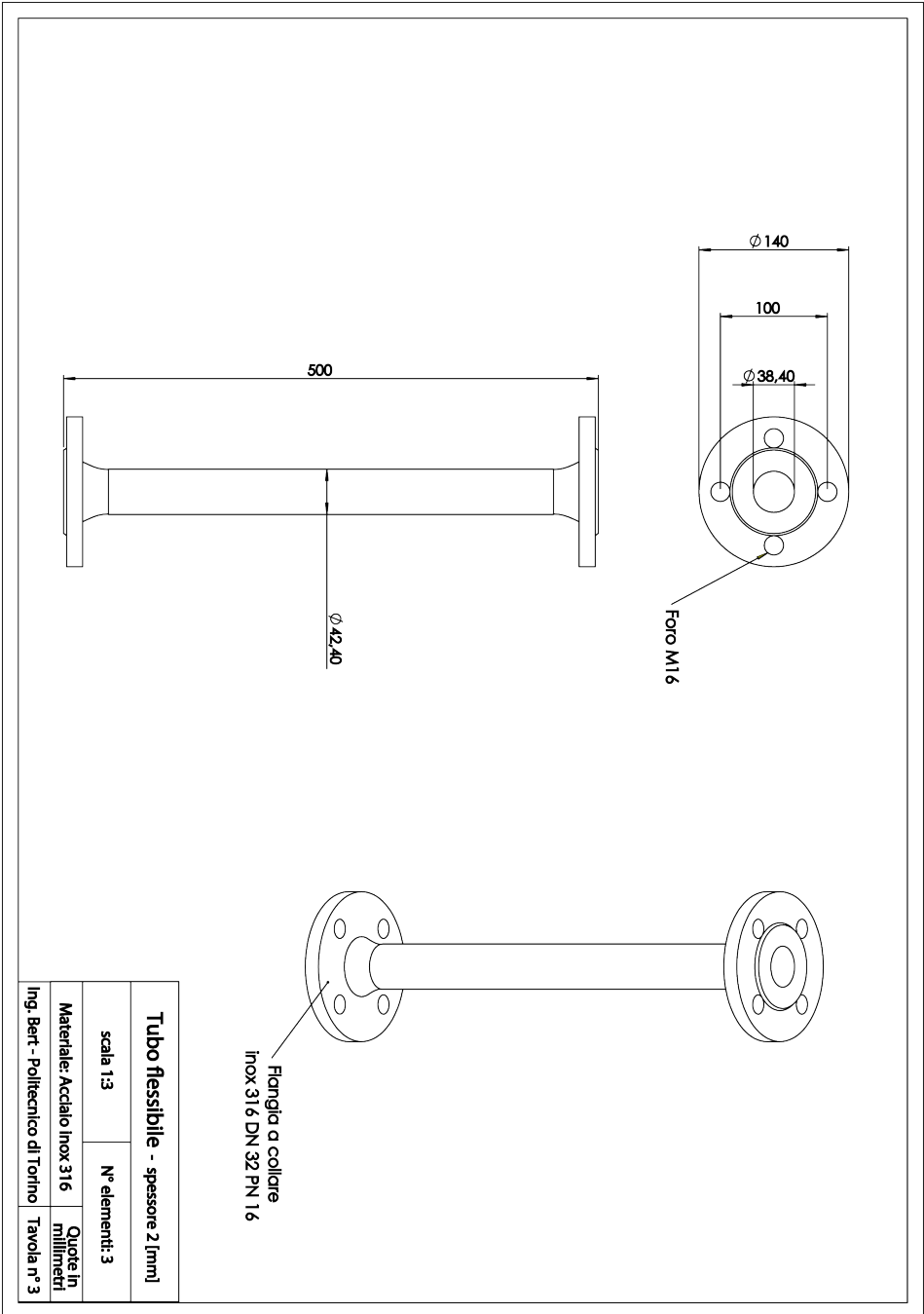


Fig. B.3 Flexible connection pipes.

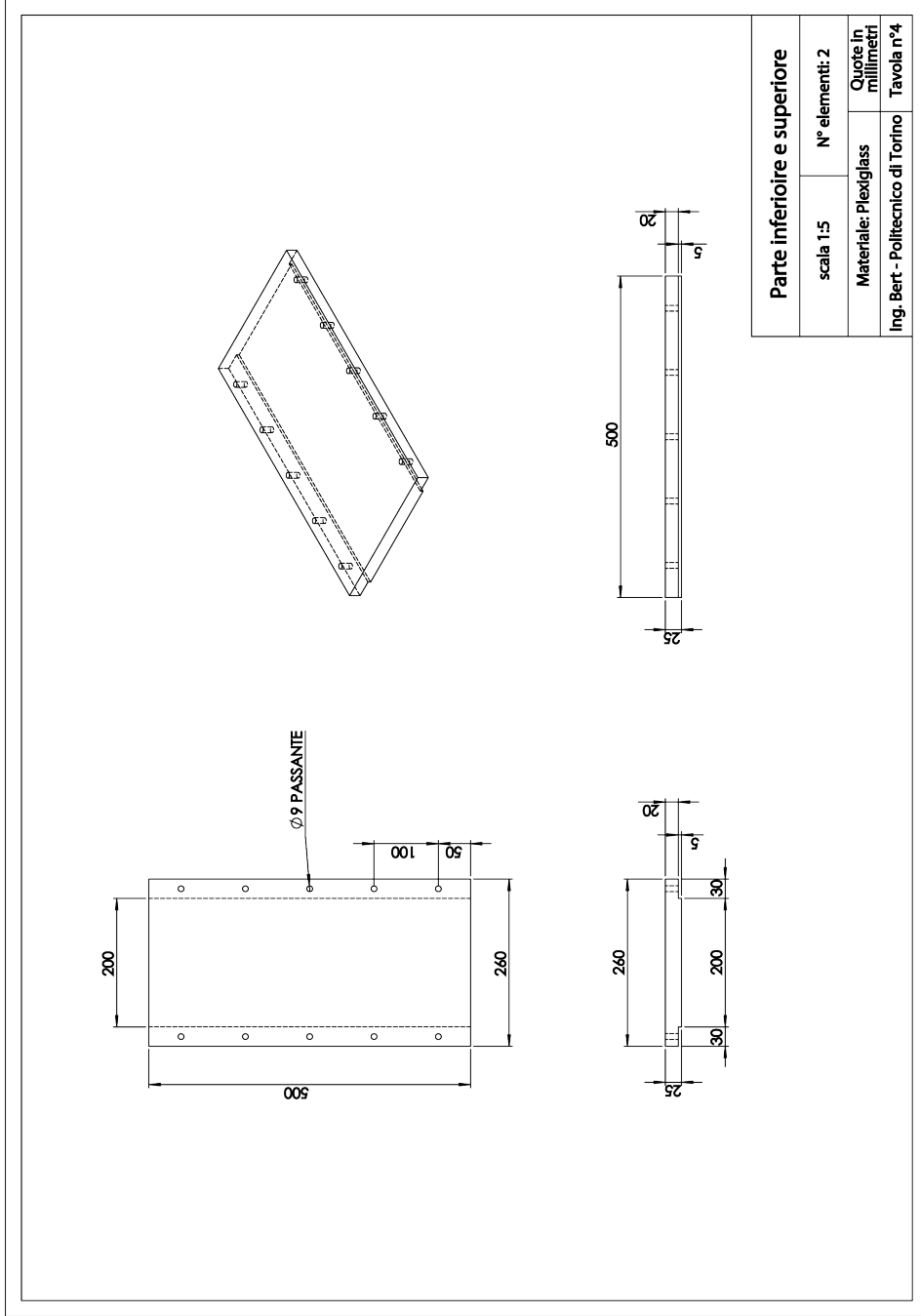


Fig. B.4 Upper and lower part of the connection between the fluid-dynamic convergent and the test section.

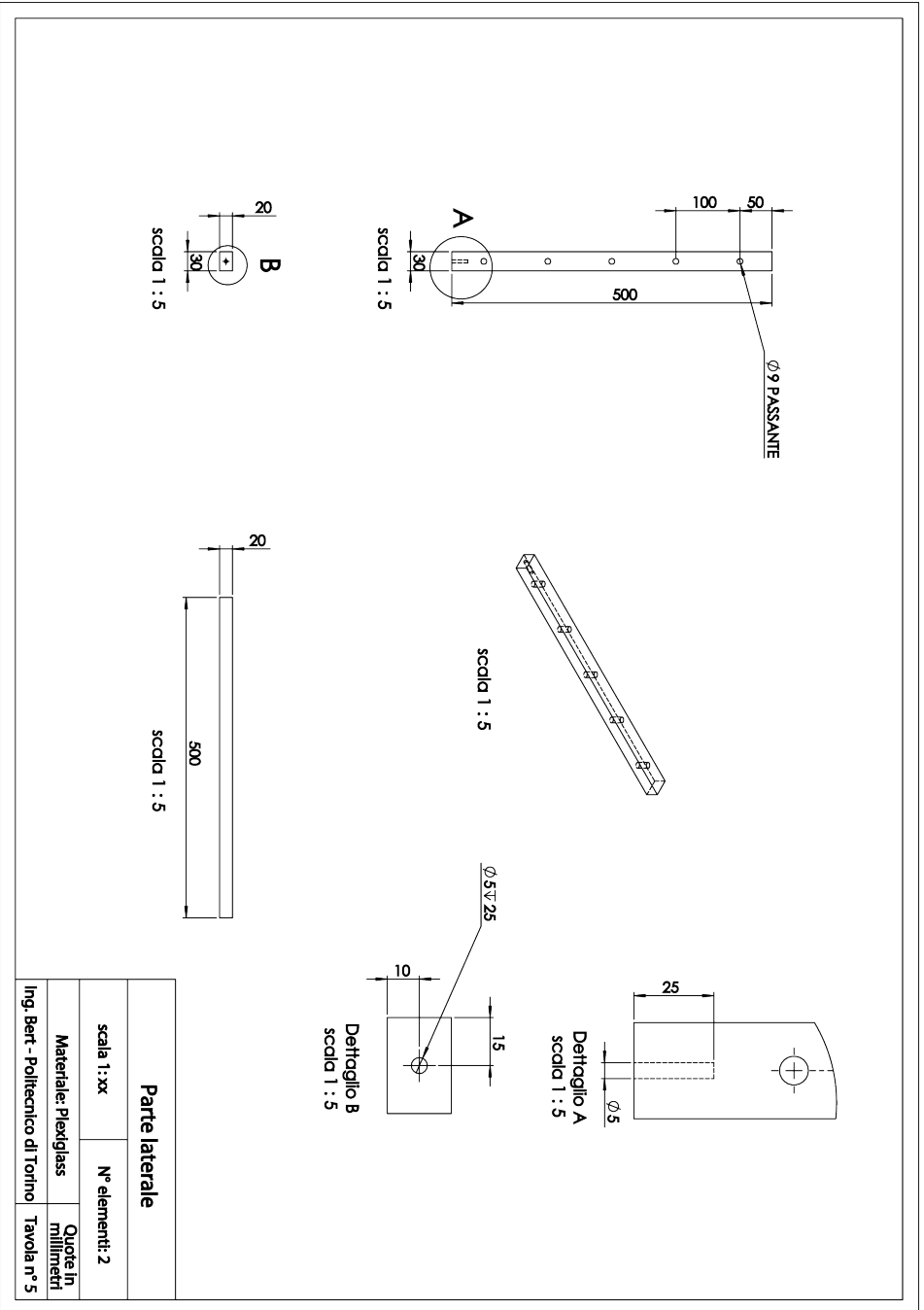


Fig. B.5 Side part of the connection between the fluid-dynamic convergent and the test section.

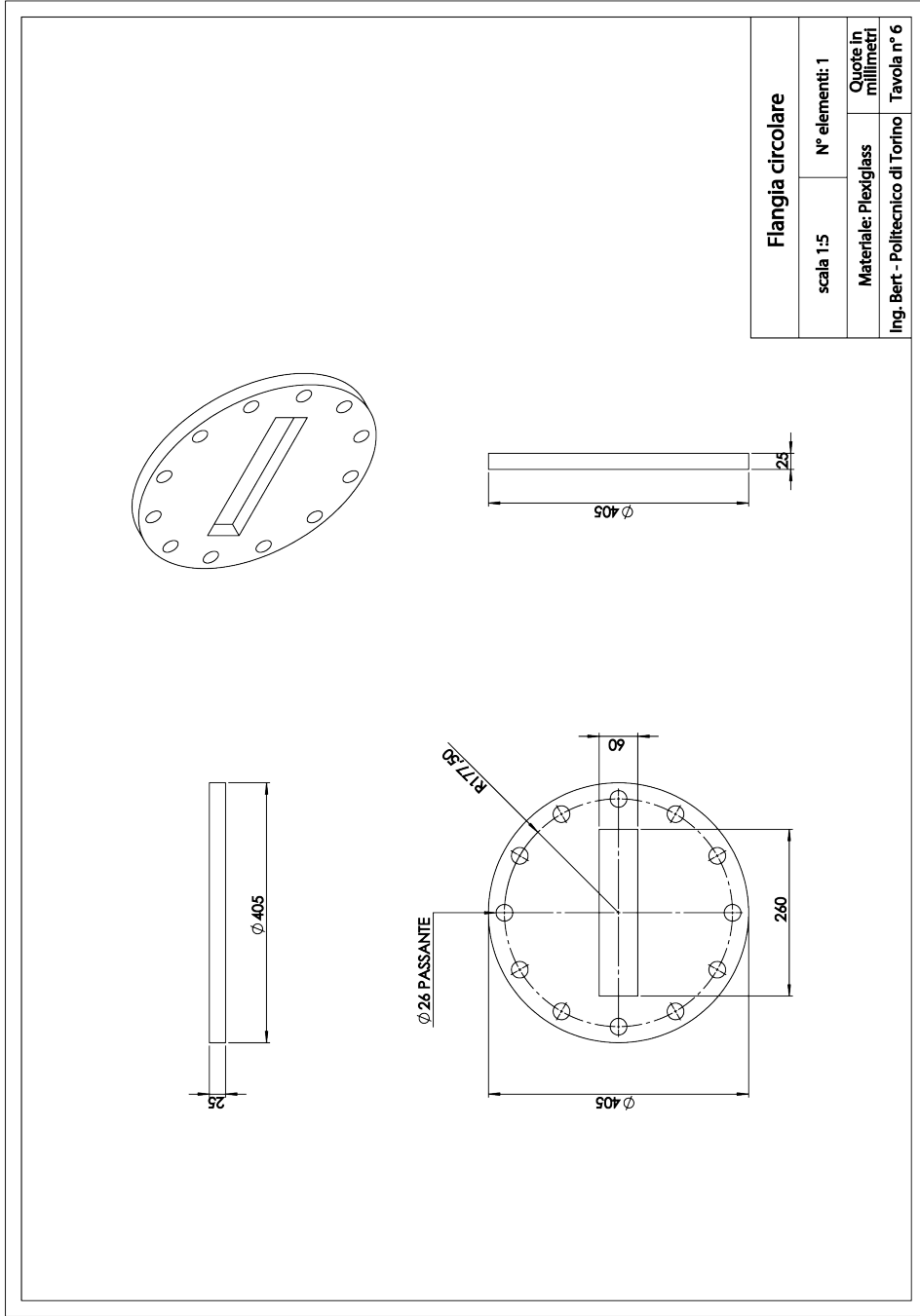


Fig. B.6 Circular flange for connection with the fluid dynamic convergent.

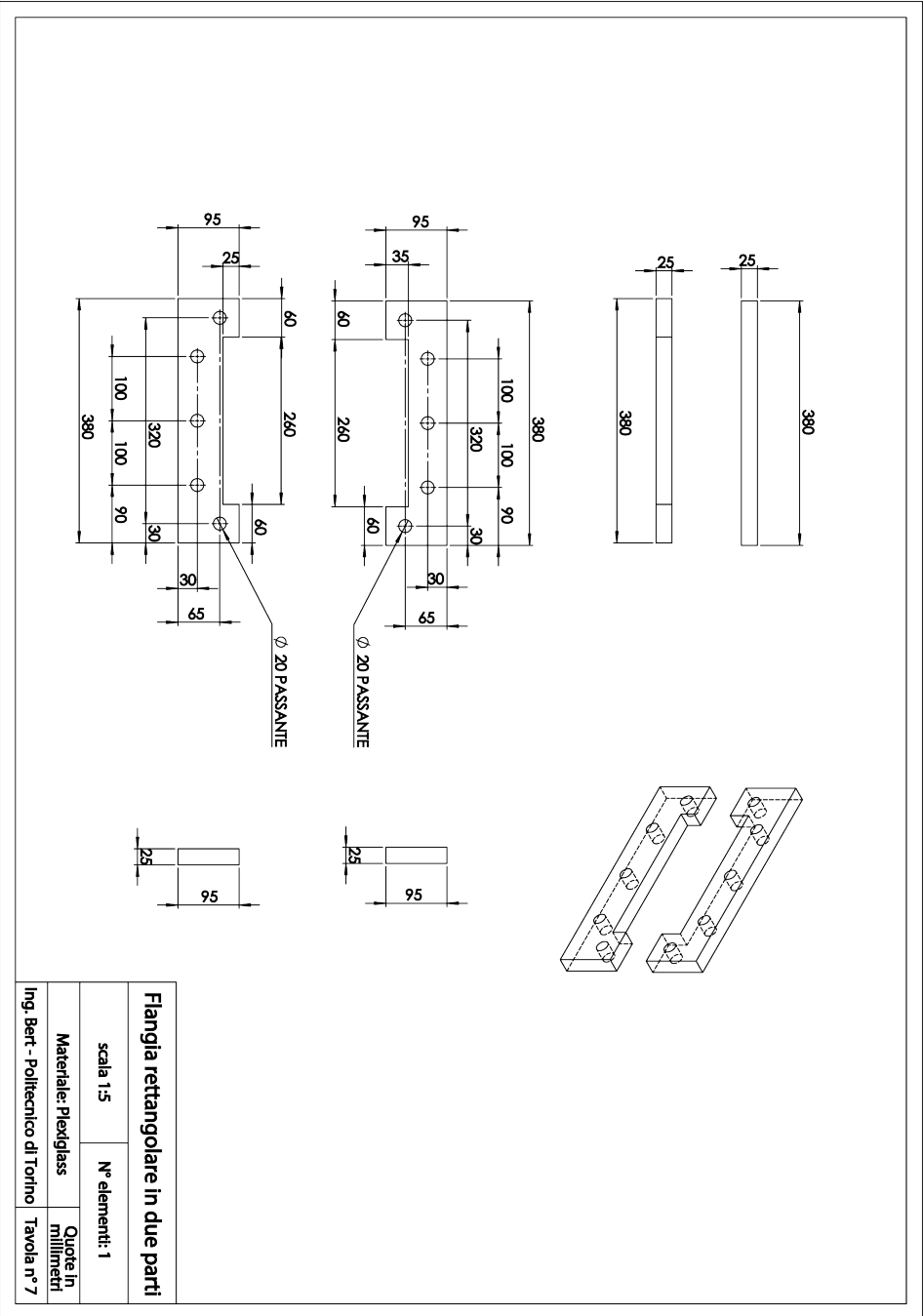


Fig. B.7 Rectangular flange for connection with the test section.

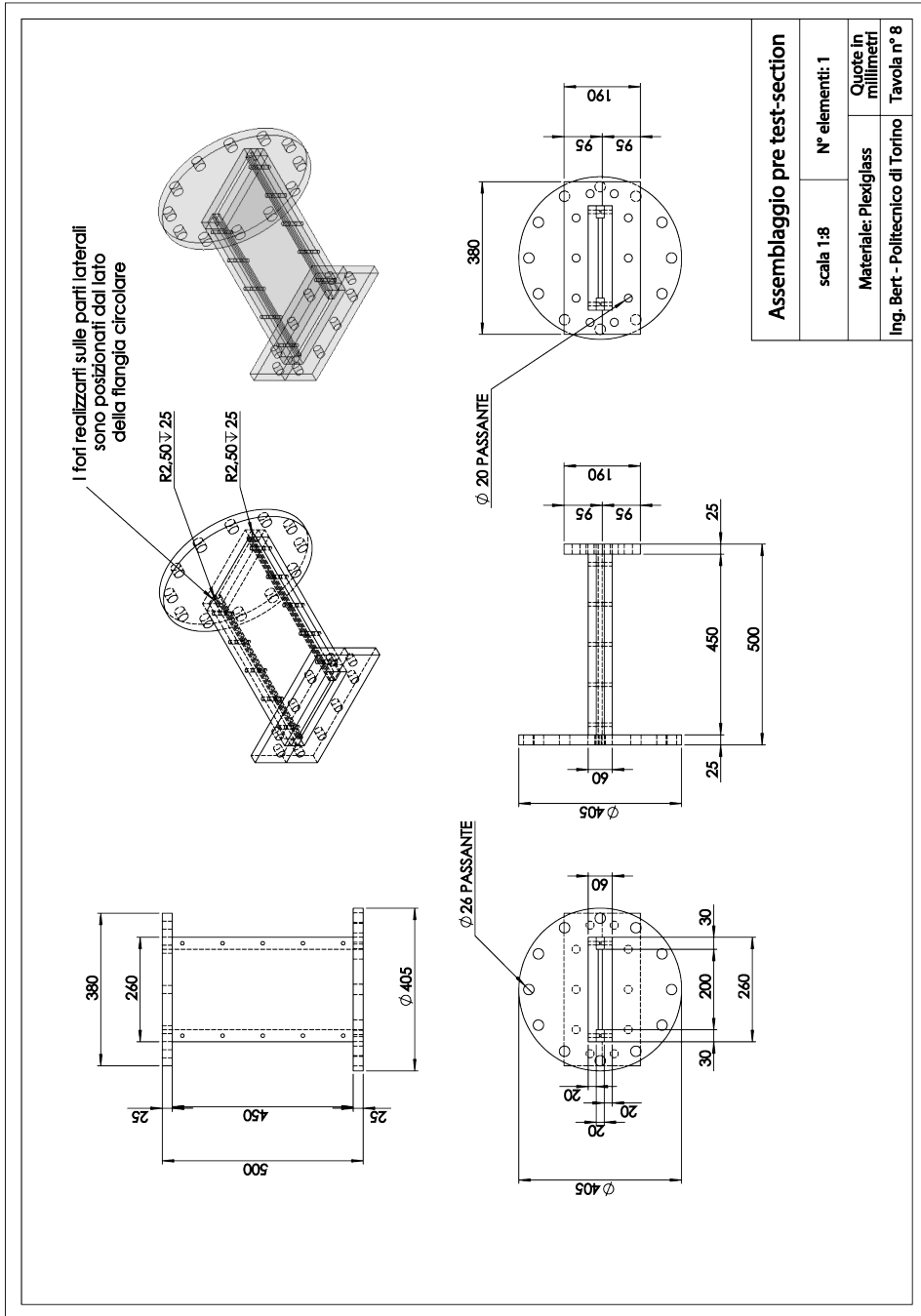


Fig. B.8 Assembly of the connection.

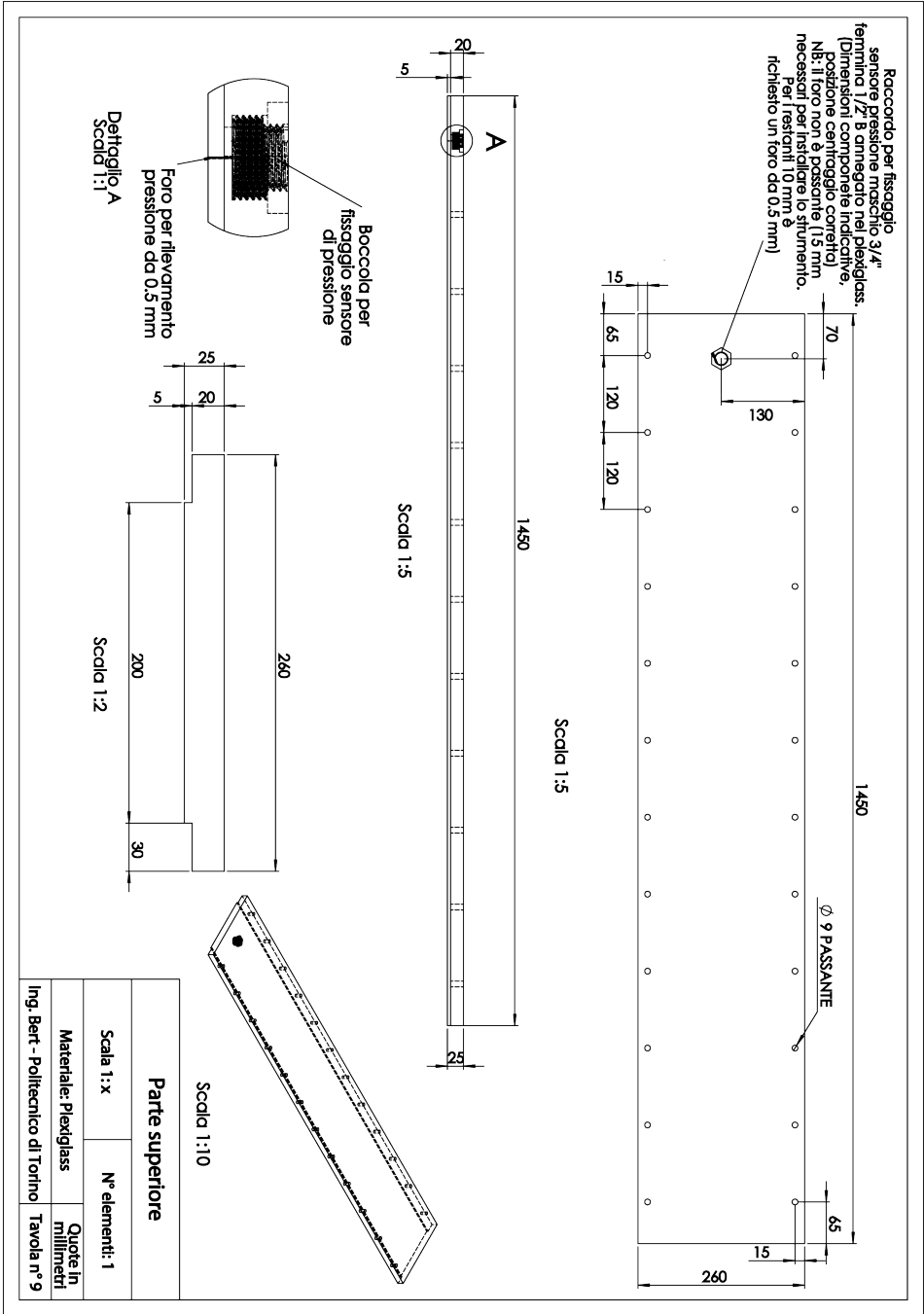


Fig. B.9 Upper part of the test section.

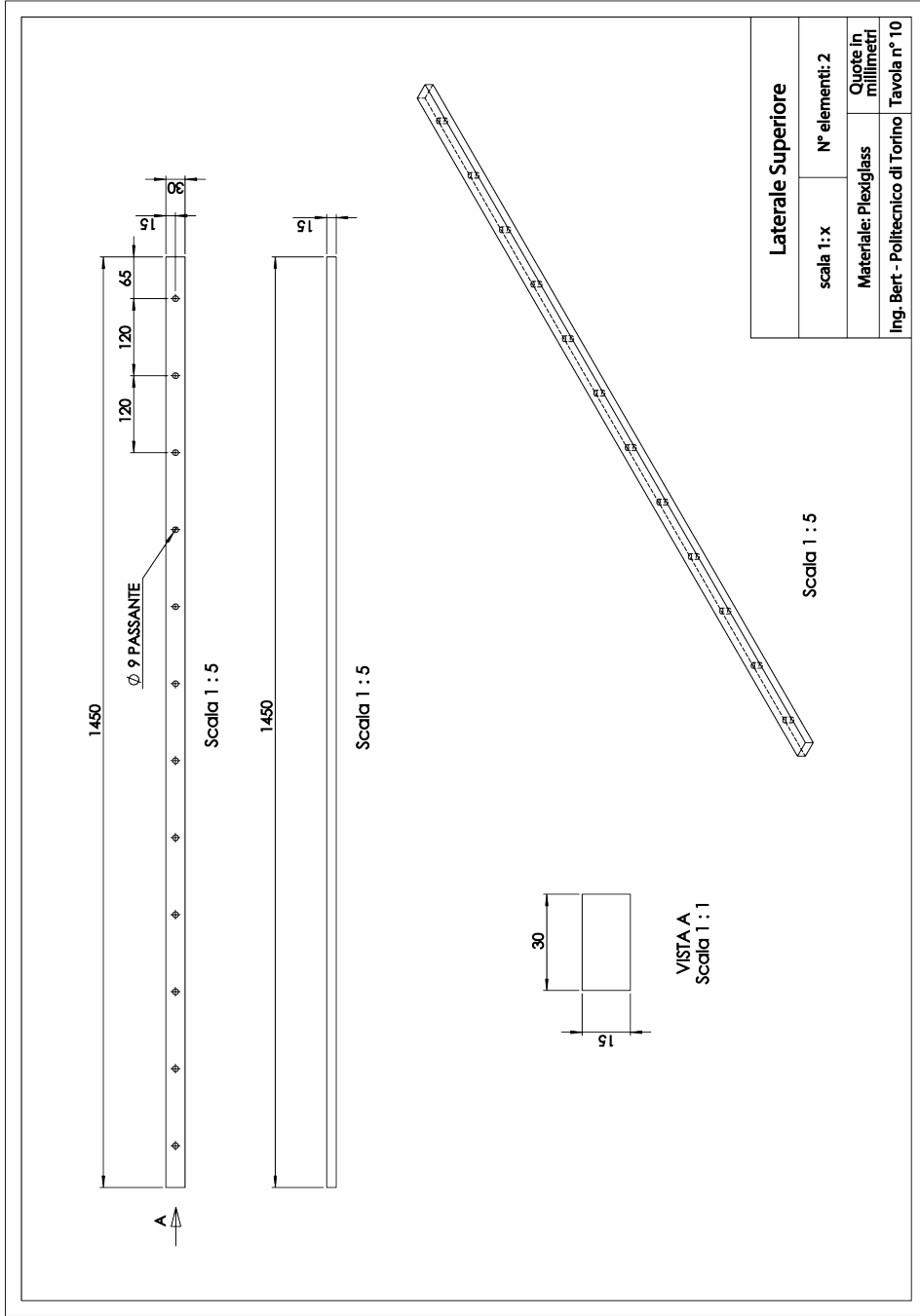


Fig. B.10 Lateral upper part of the test section.

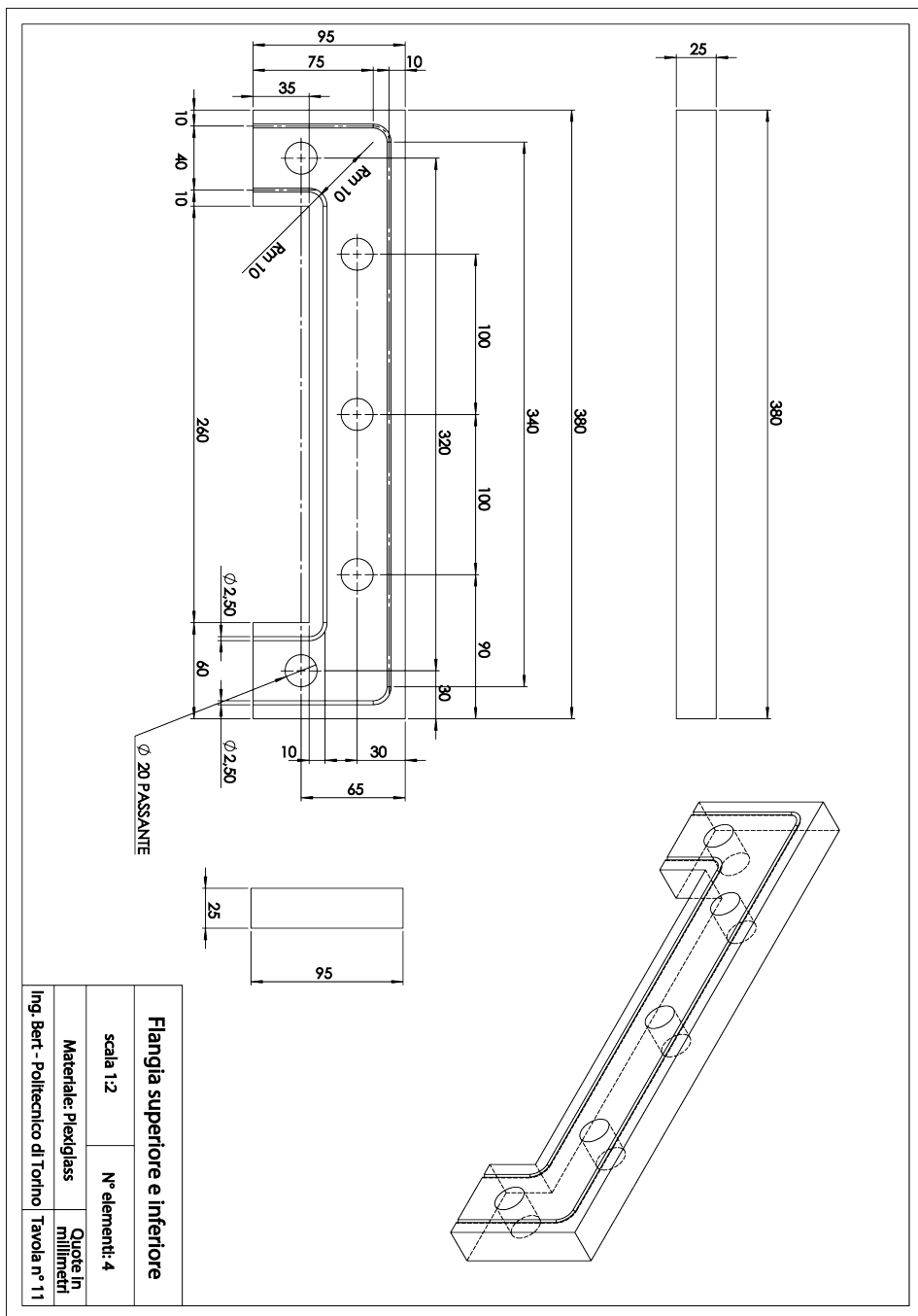


Fig. B. 11 Upper and lower* flange of the test section. *Filtration tests.

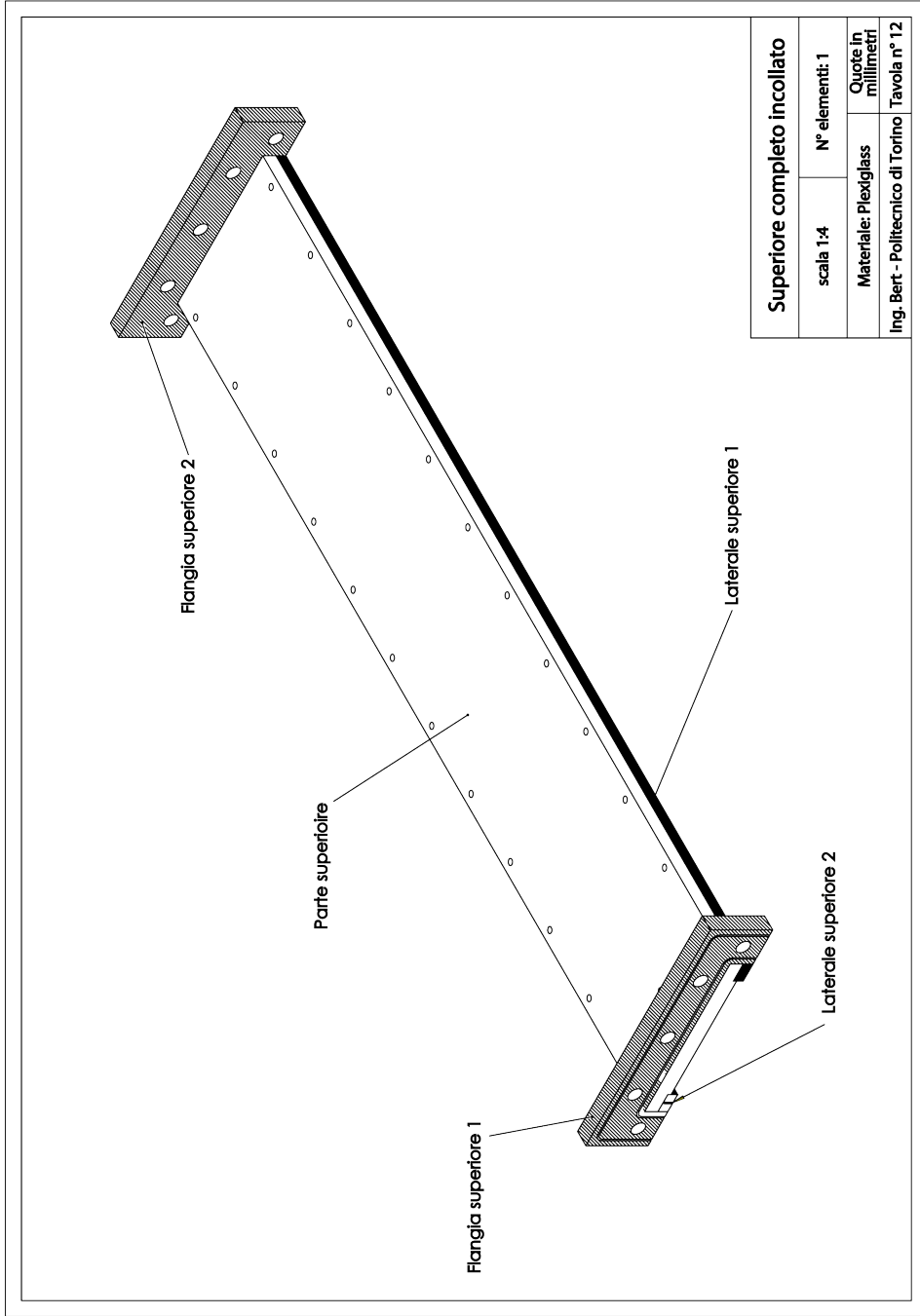


Fig. B.12 Assembly of the upper part of the test section.

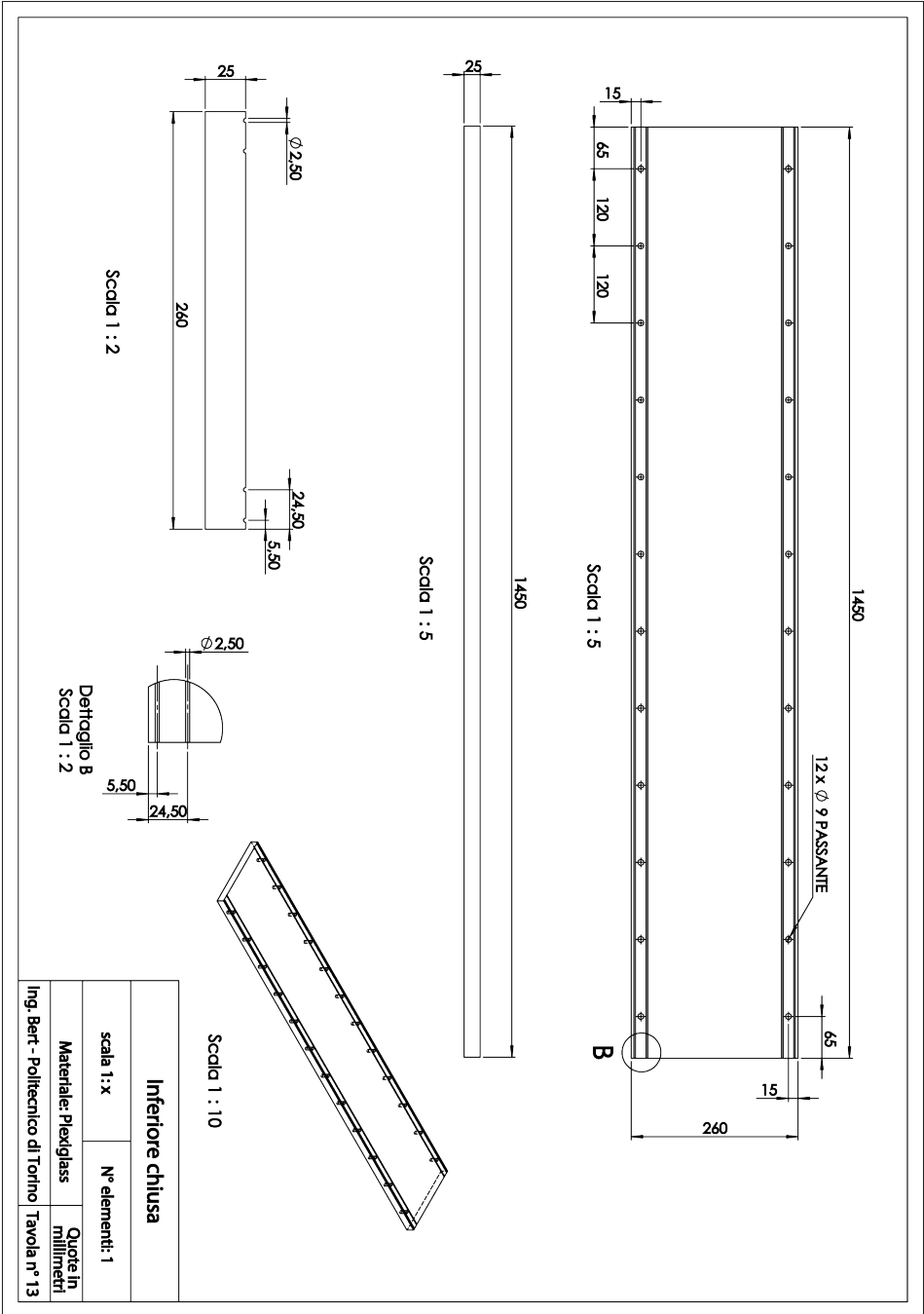


Fig. B.13 Lower part of the test section for smooth-wall impermeable tests.

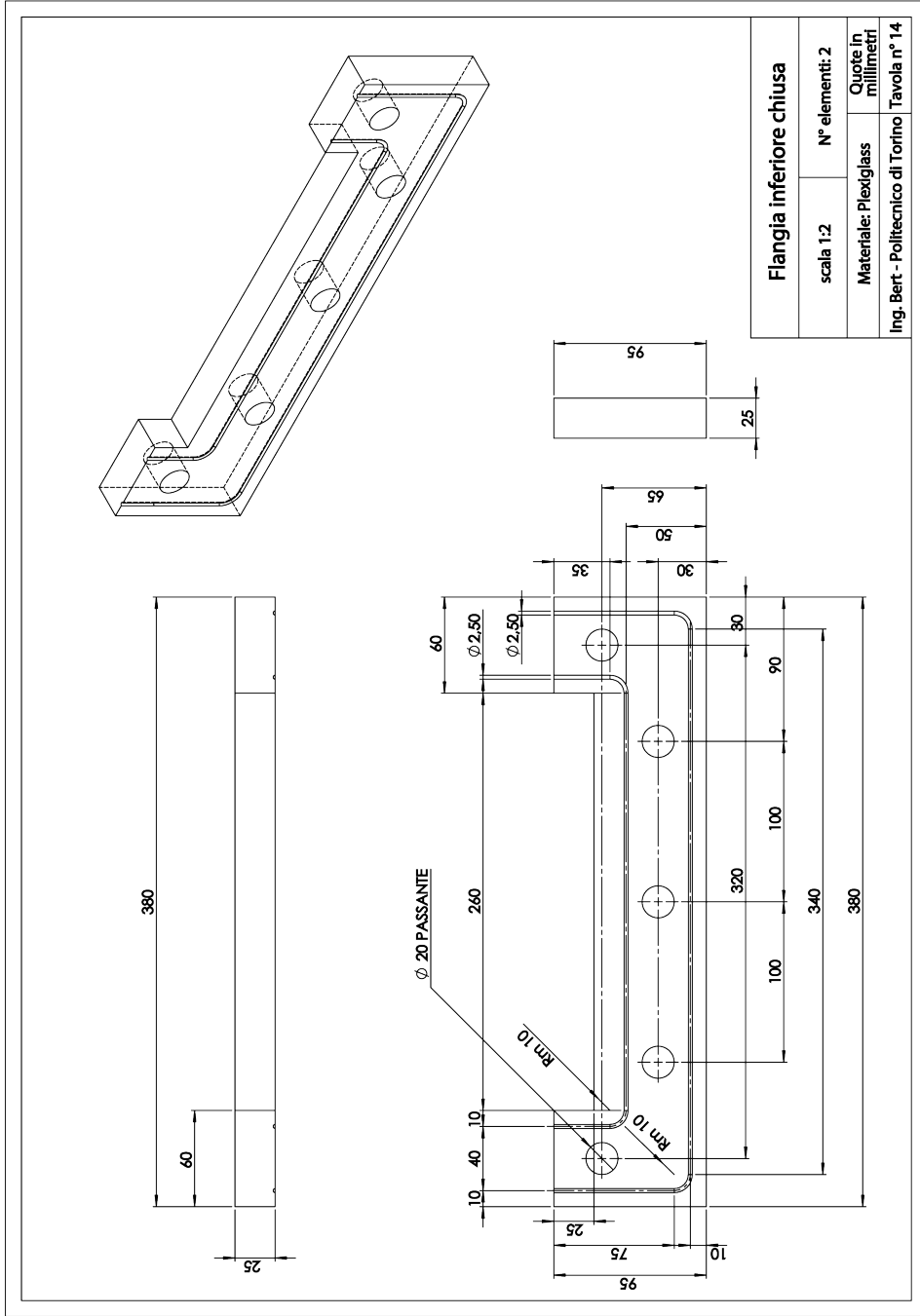


Fig. B.14 Lower flange of the test section for smooth-wall impermeable tests.

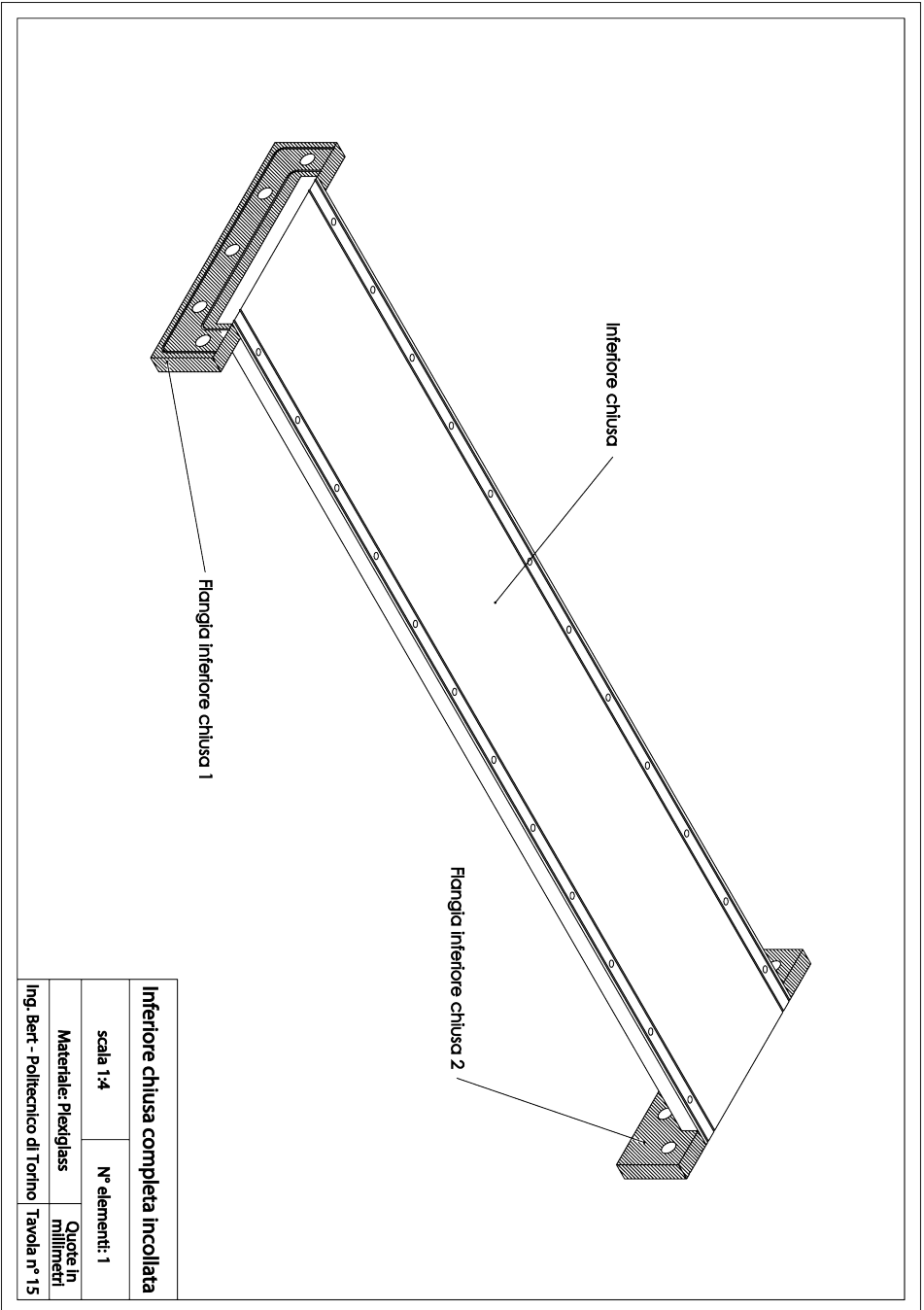


Fig. B.15 Assembly of the lower part of the test section for smooth-wall impermeable tests.

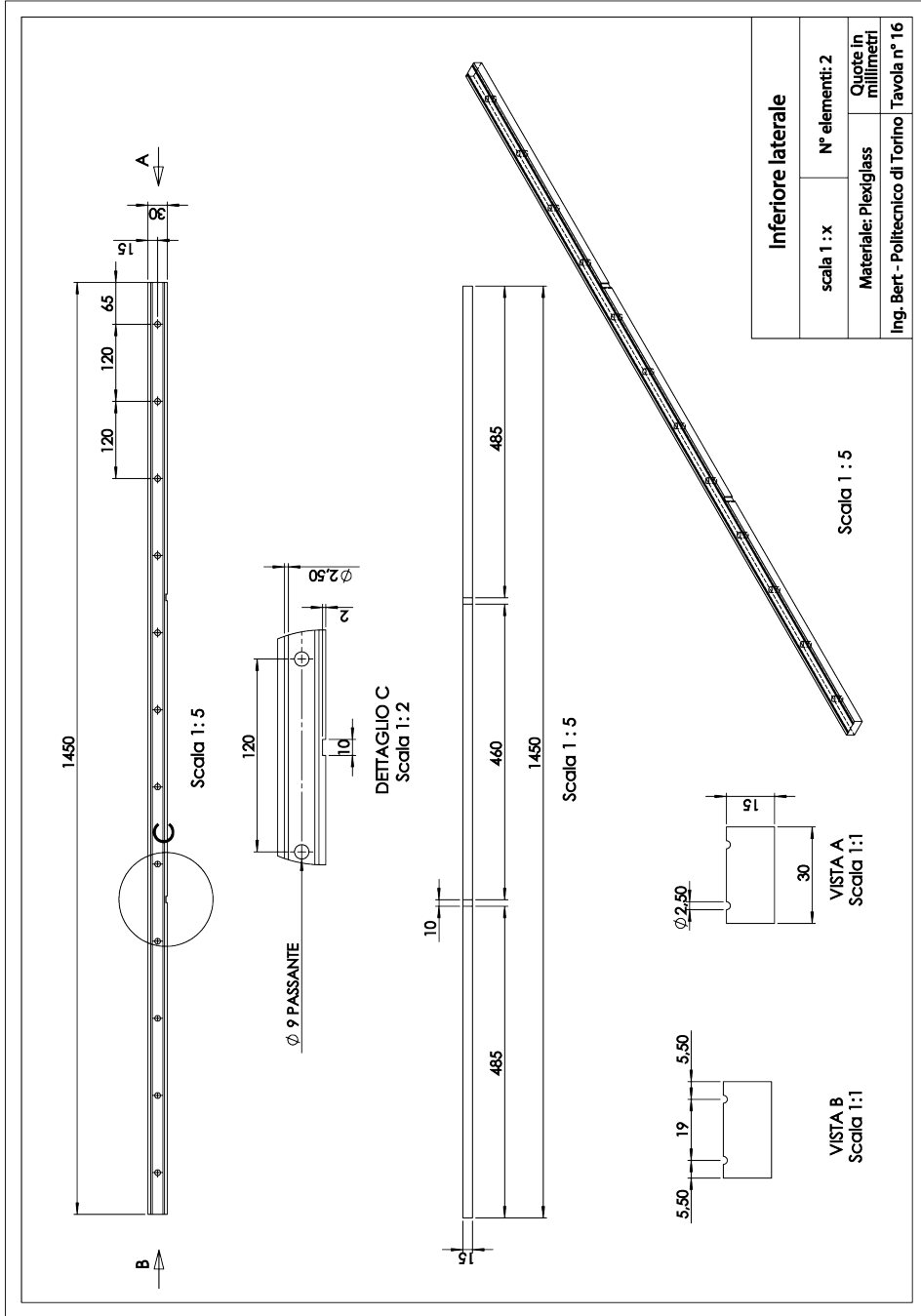


Fig. B.16 Lateral lower part of the test section.

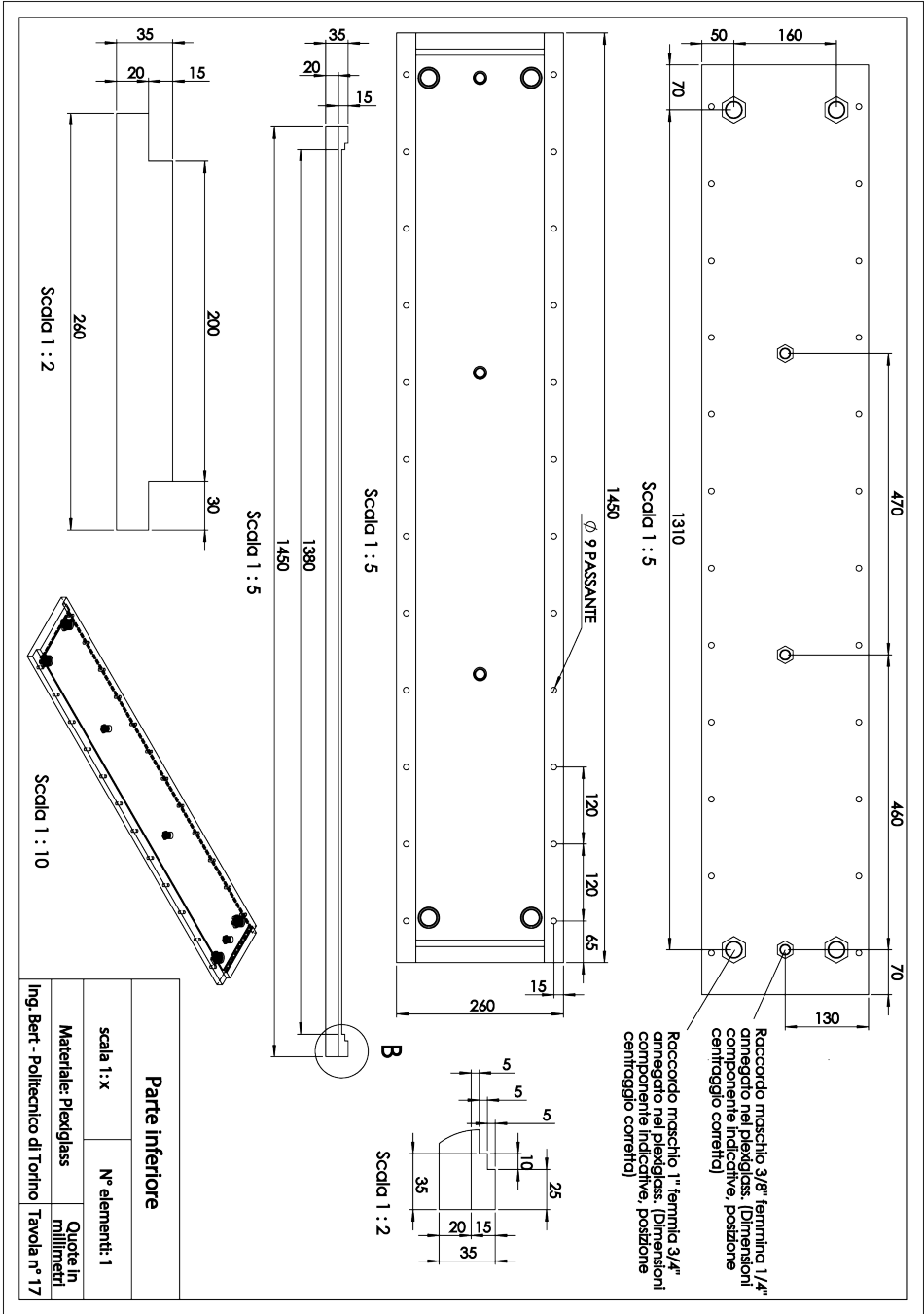


Fig. B.17 Lower part of the test section for filtration tests.

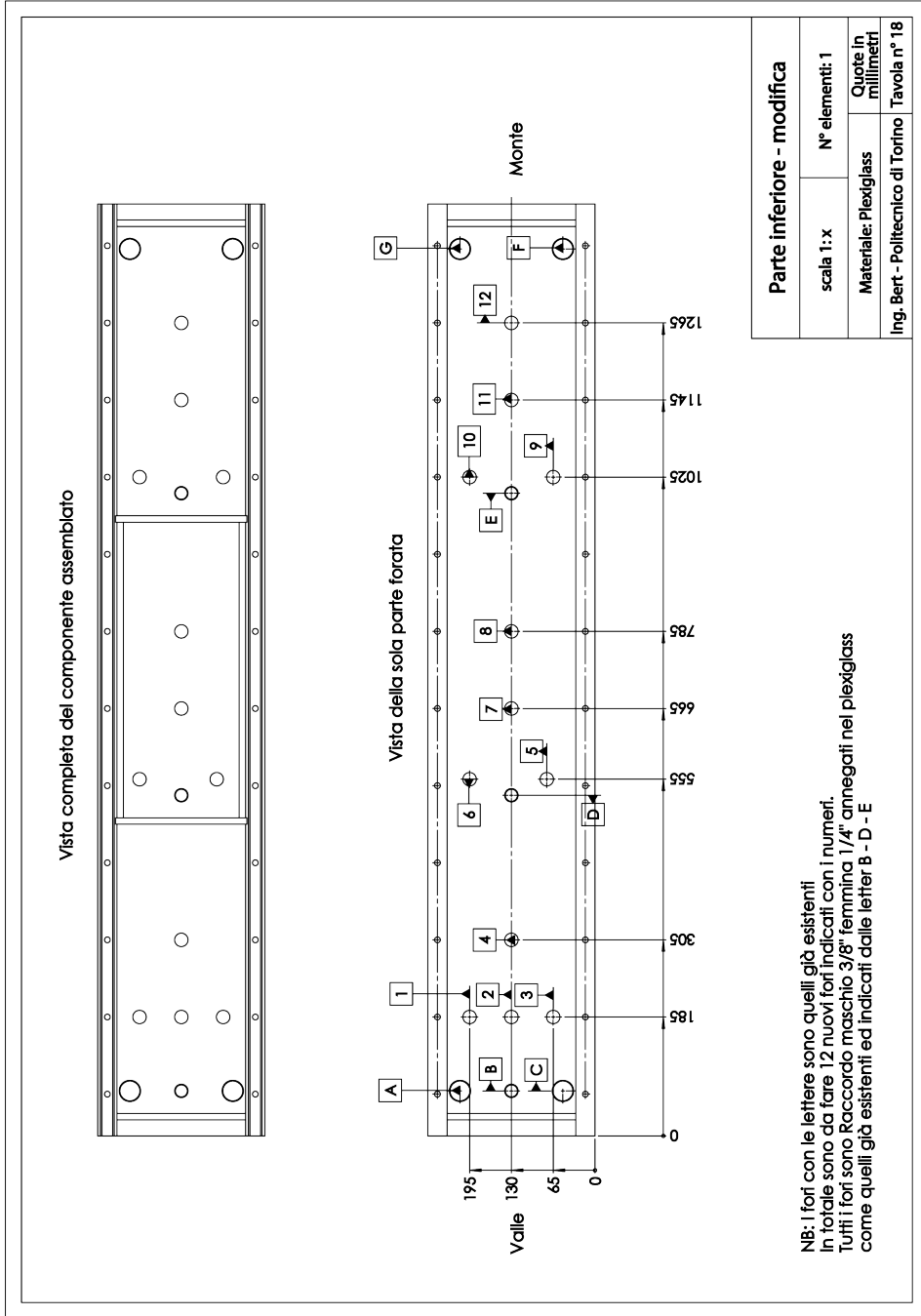


Fig. B.18 Update of the lower part of the test section for filtration tests.

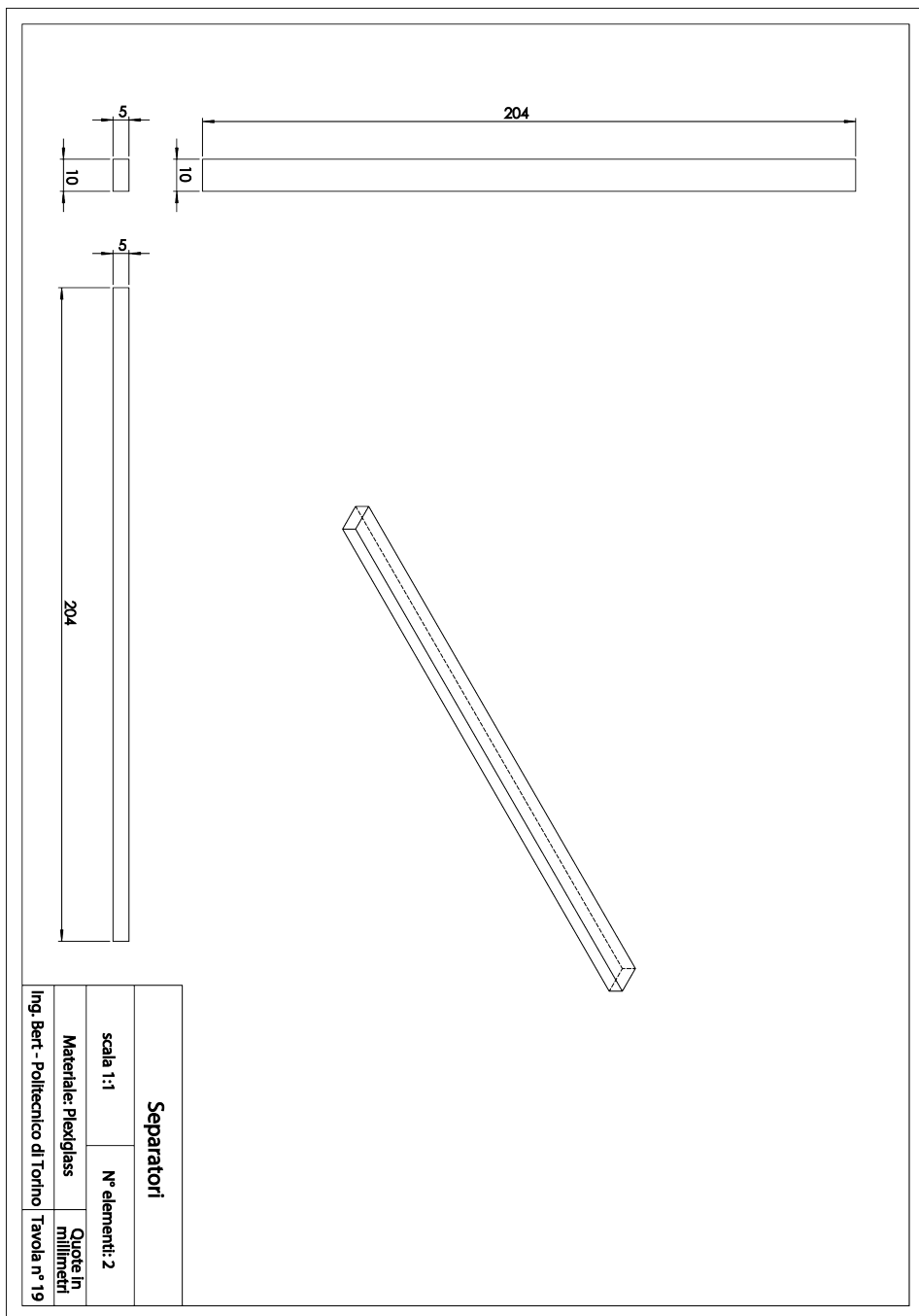


Fig. B.19 Internal dividers of the lower part of the test section.

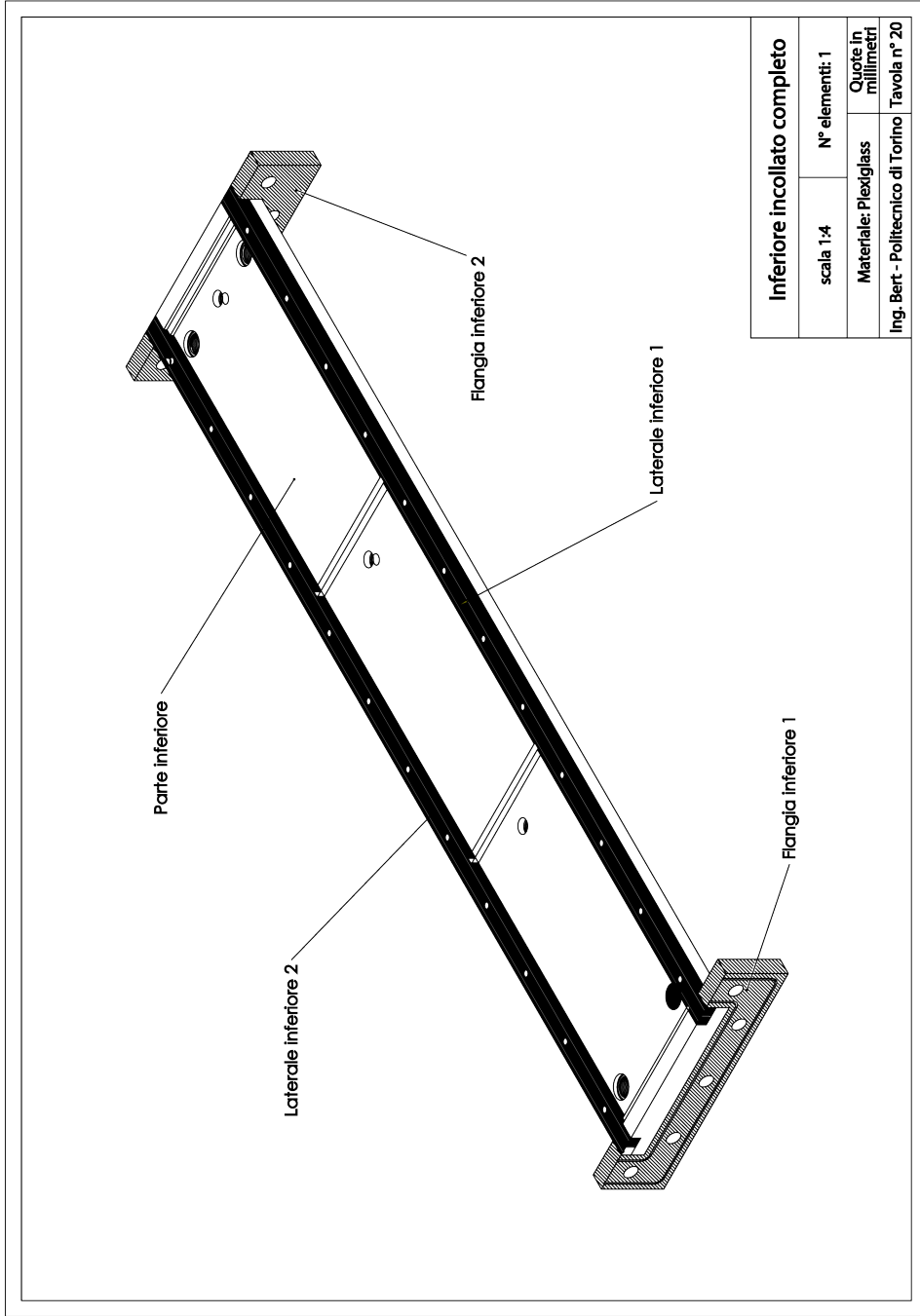


Fig. B.20 Assembly of the lower part of the test section for filtration tests.

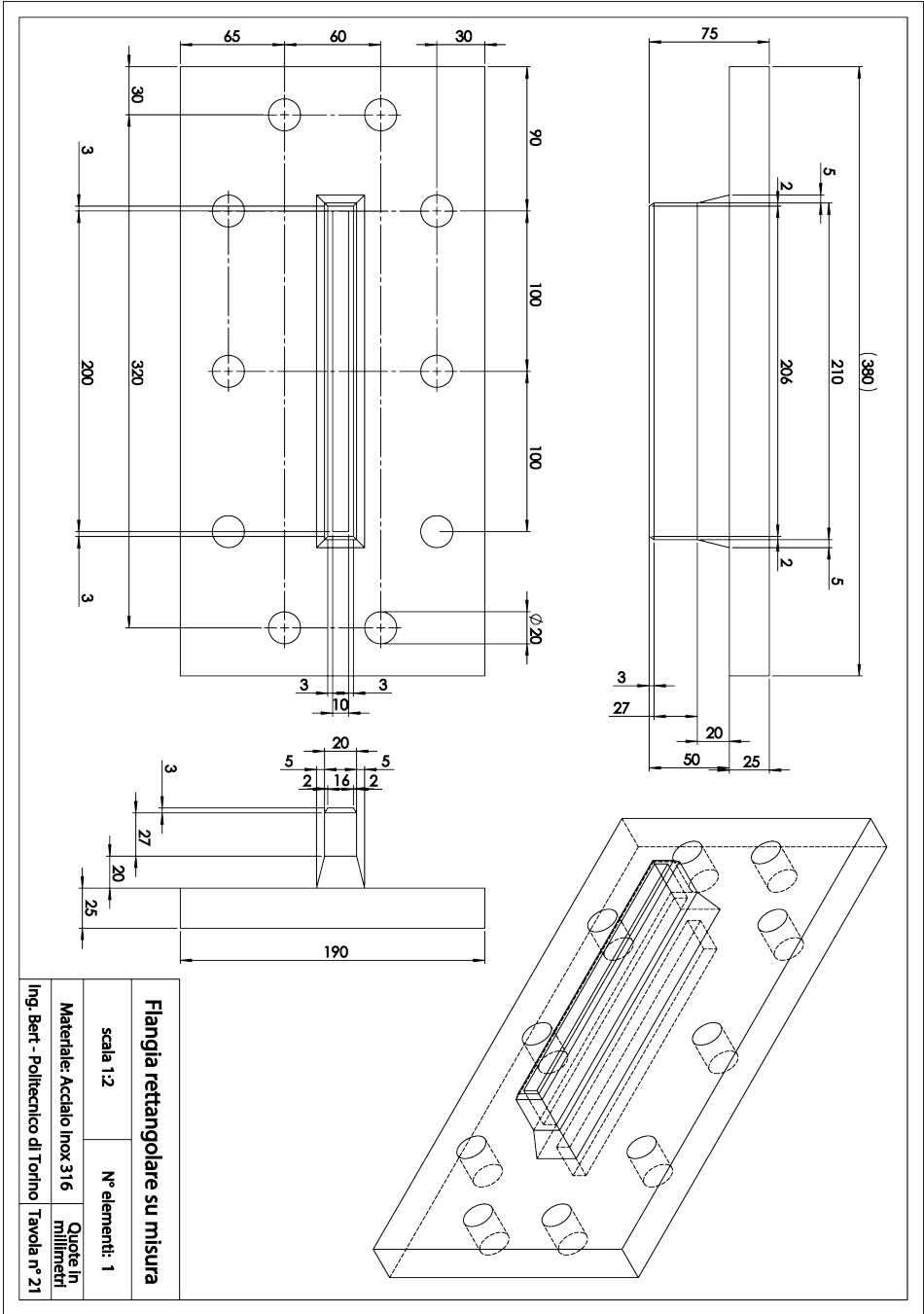


Fig. B.21 Rectangular flange for connection with the post test section.

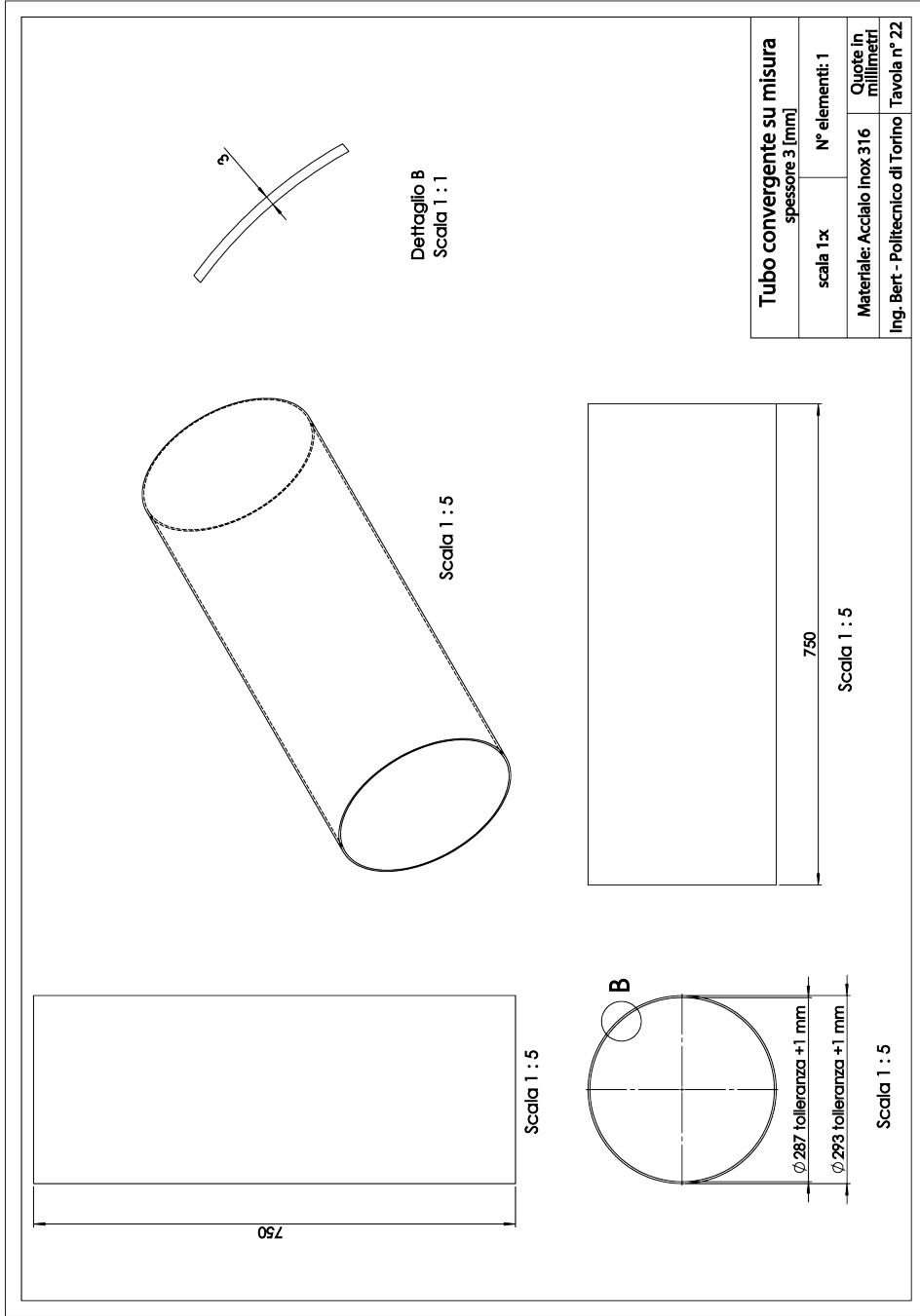


Fig. B.22 Flow-dynamics convergent pipe.

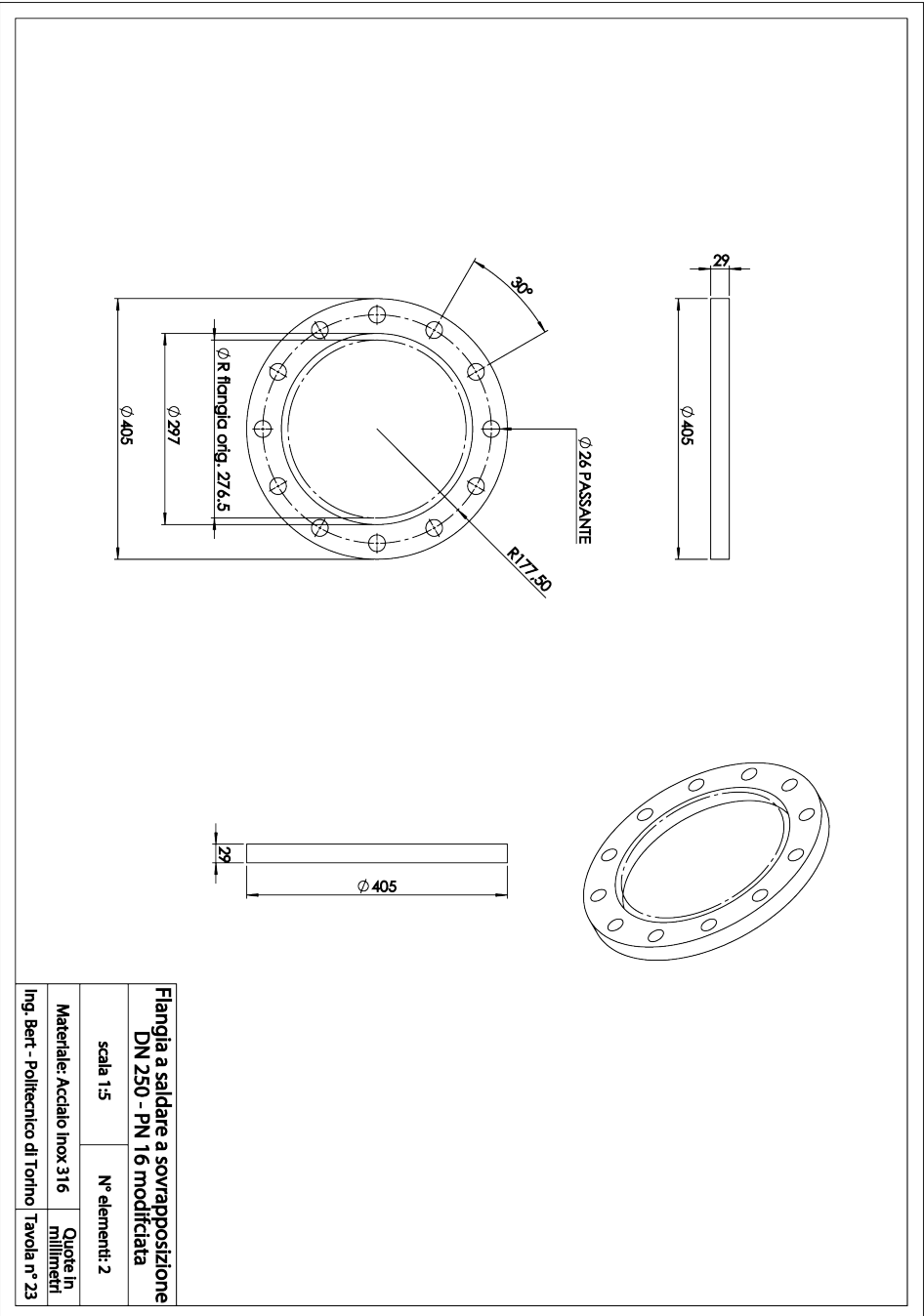


Fig. B.23 Flange for the flow-dynamics convergent pipe.

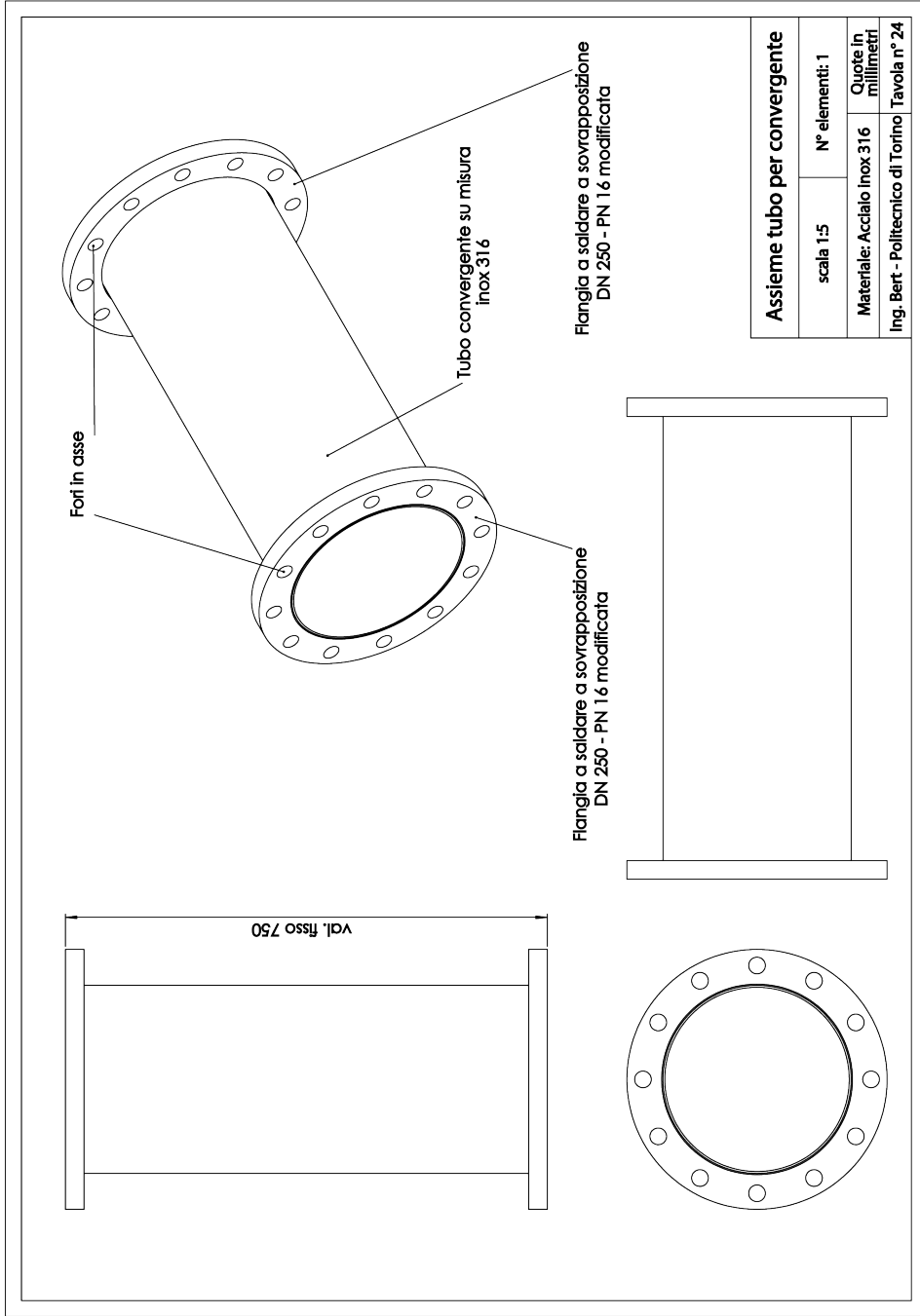


Fig. B.24 Assembly for the flow-dynamics convergent pipe..

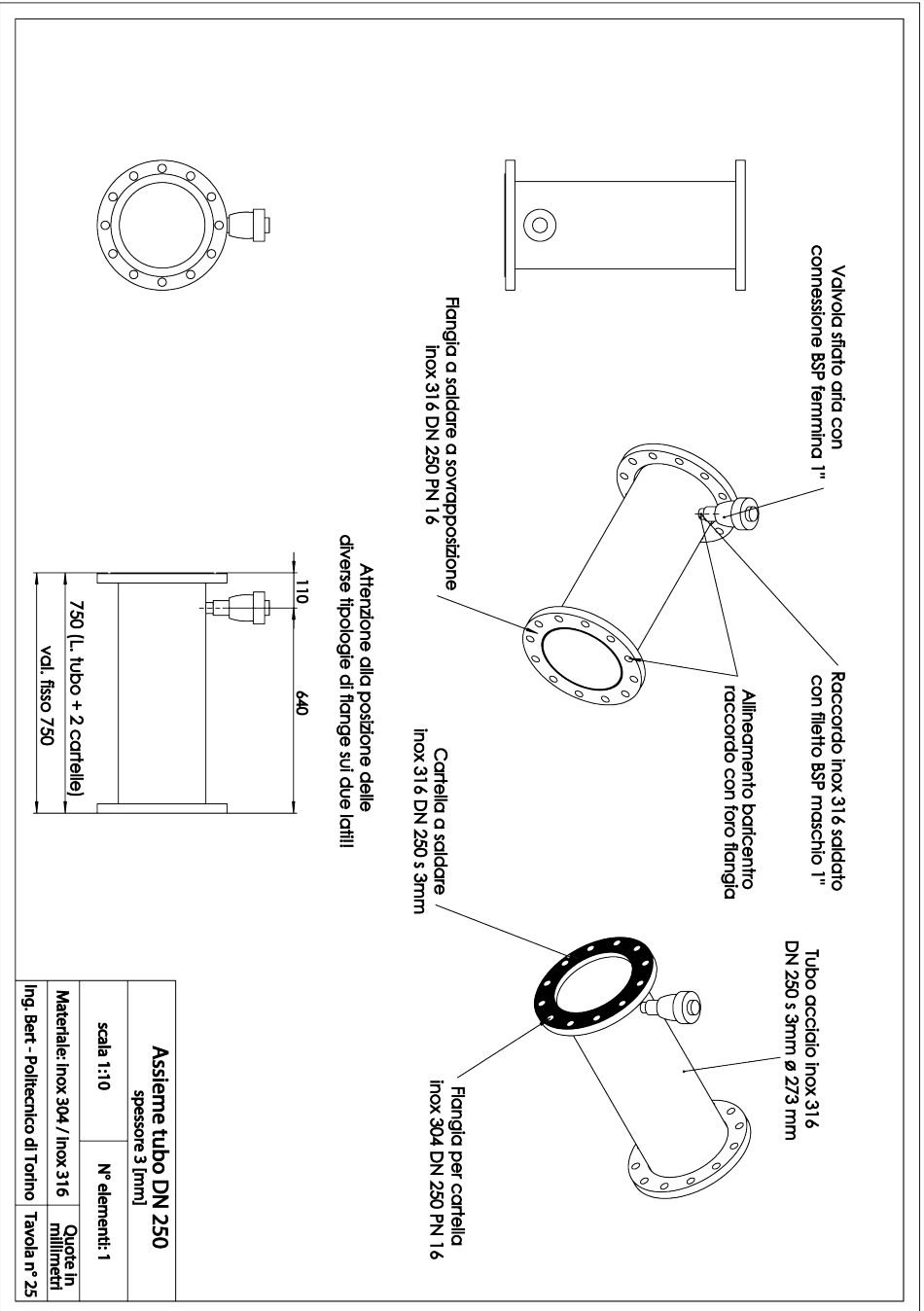


Fig. B.25 Straight pipe DN 250.

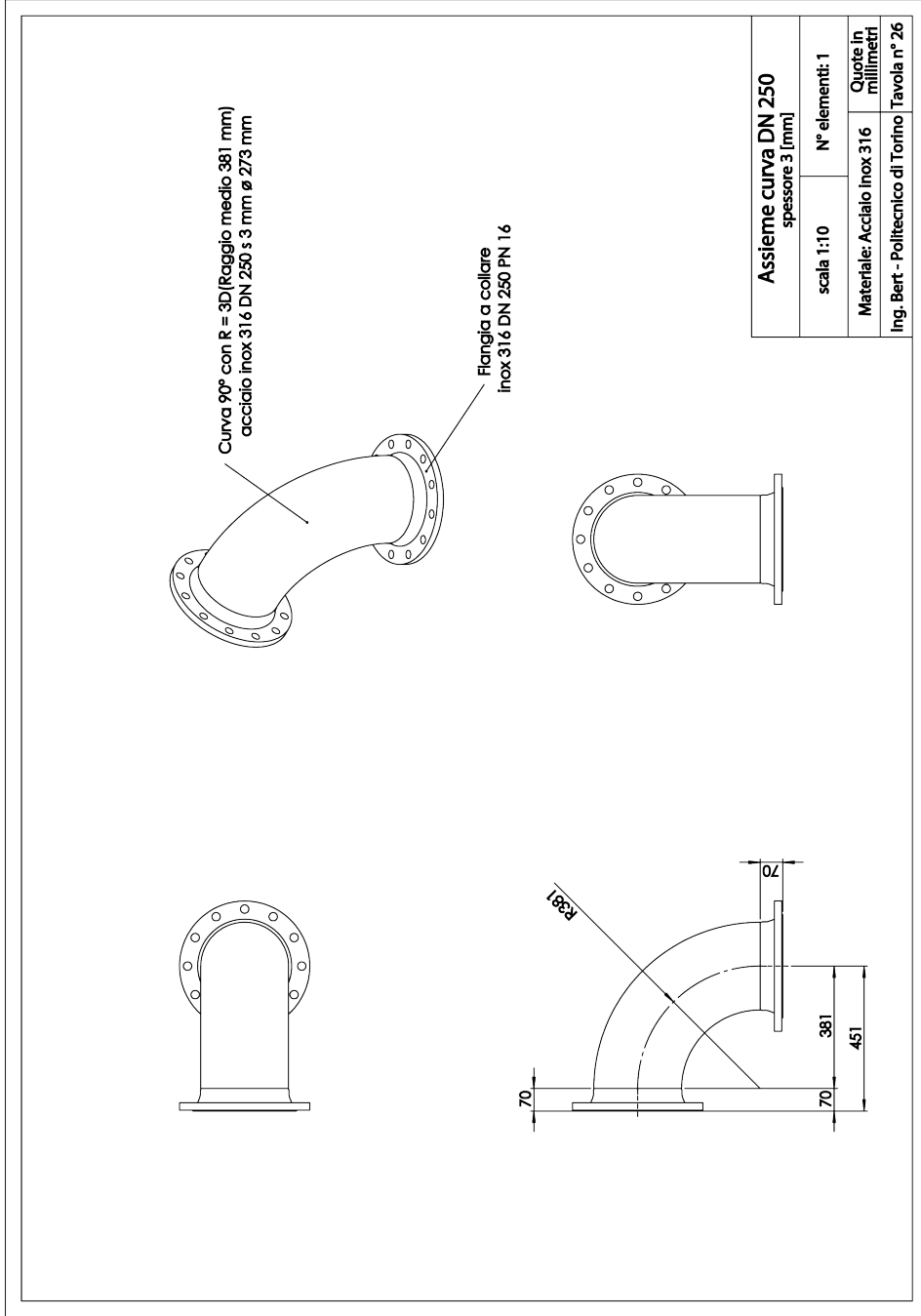


Fig. B.26 DN 250 tube with 90° bend.

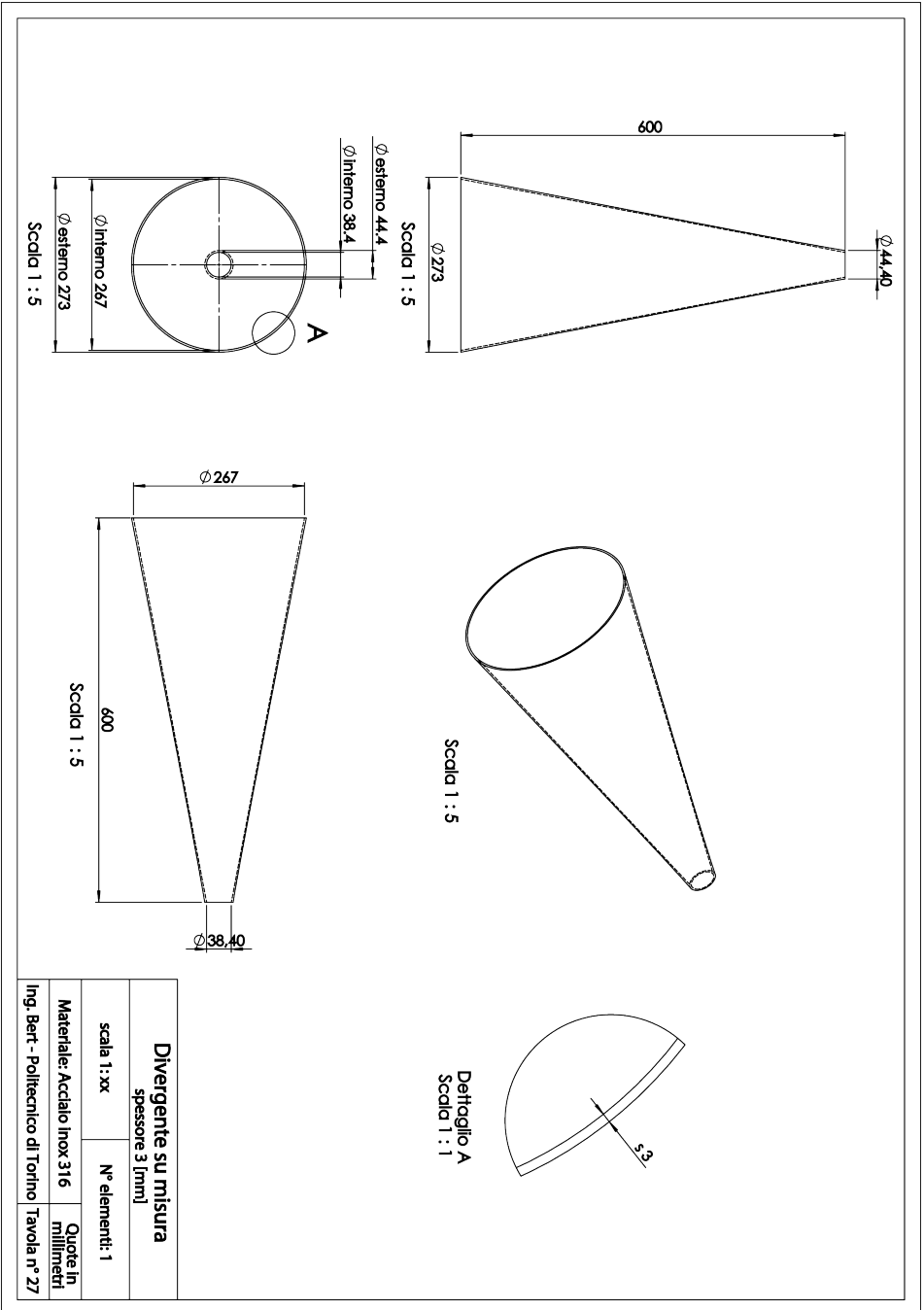


Fig. B.27 Hand made divergent.

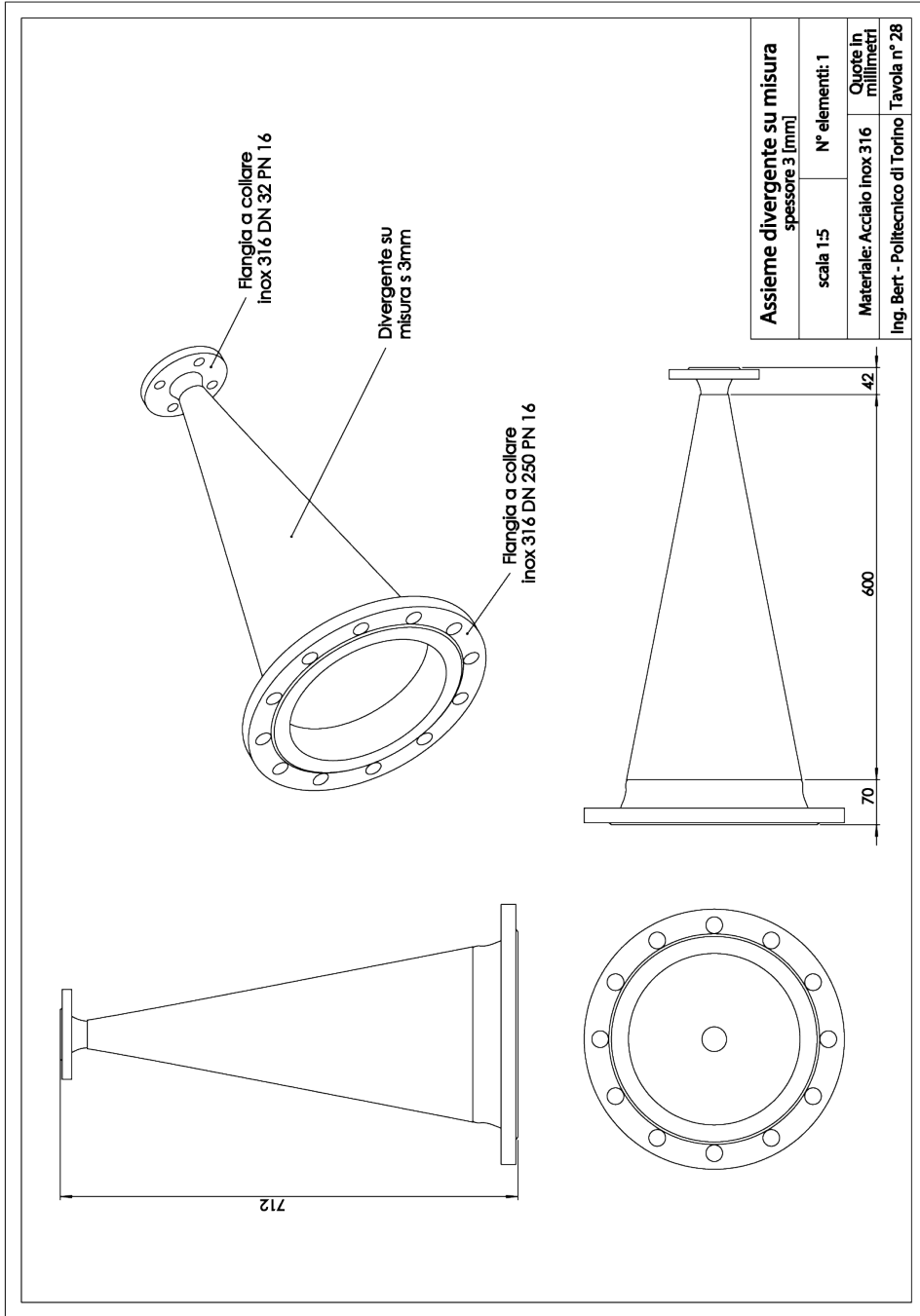


Fig. B.28 Assembly of the hand made divergent.

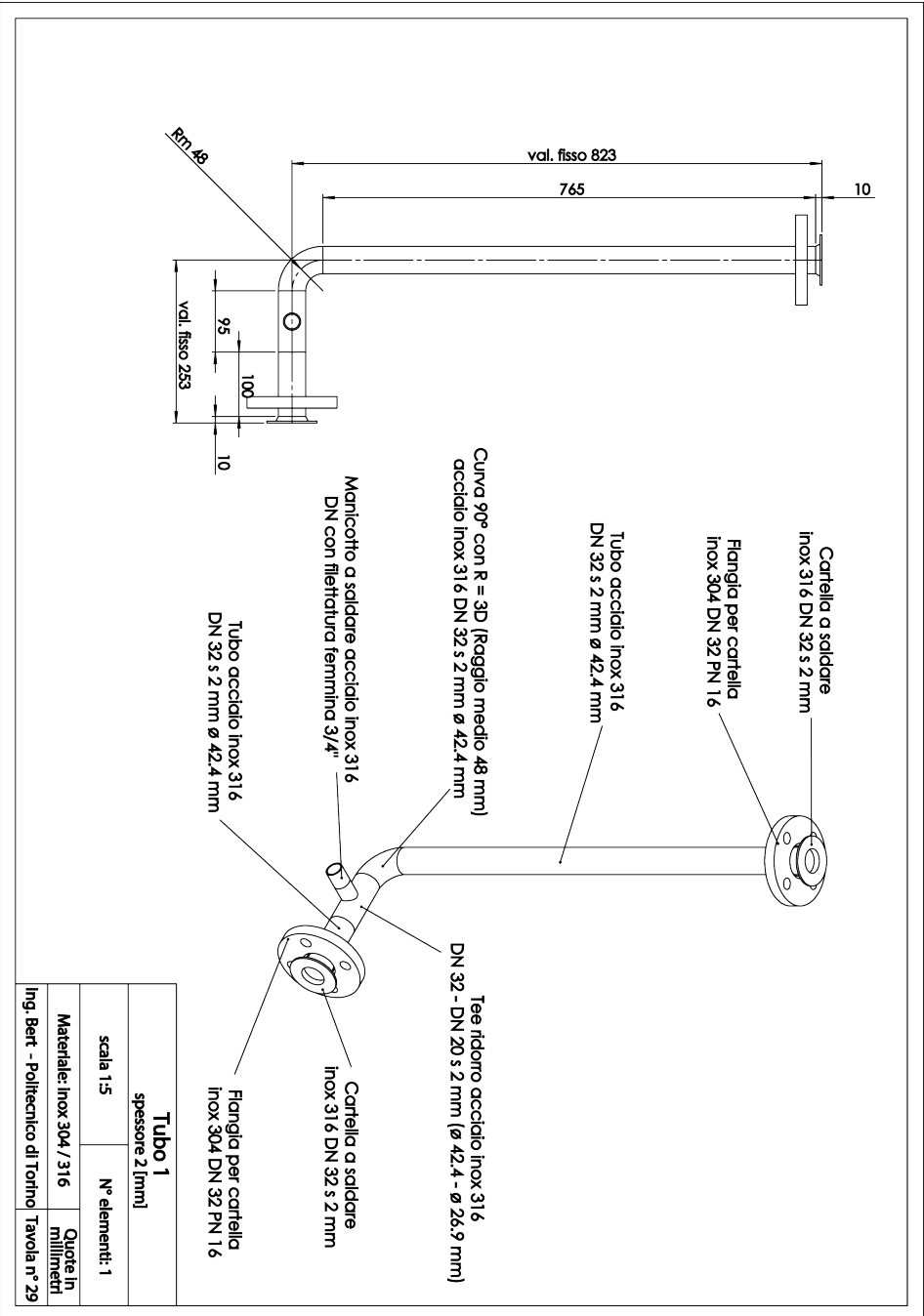


Fig. B.29 Pipe 1 of the main line DN 32.

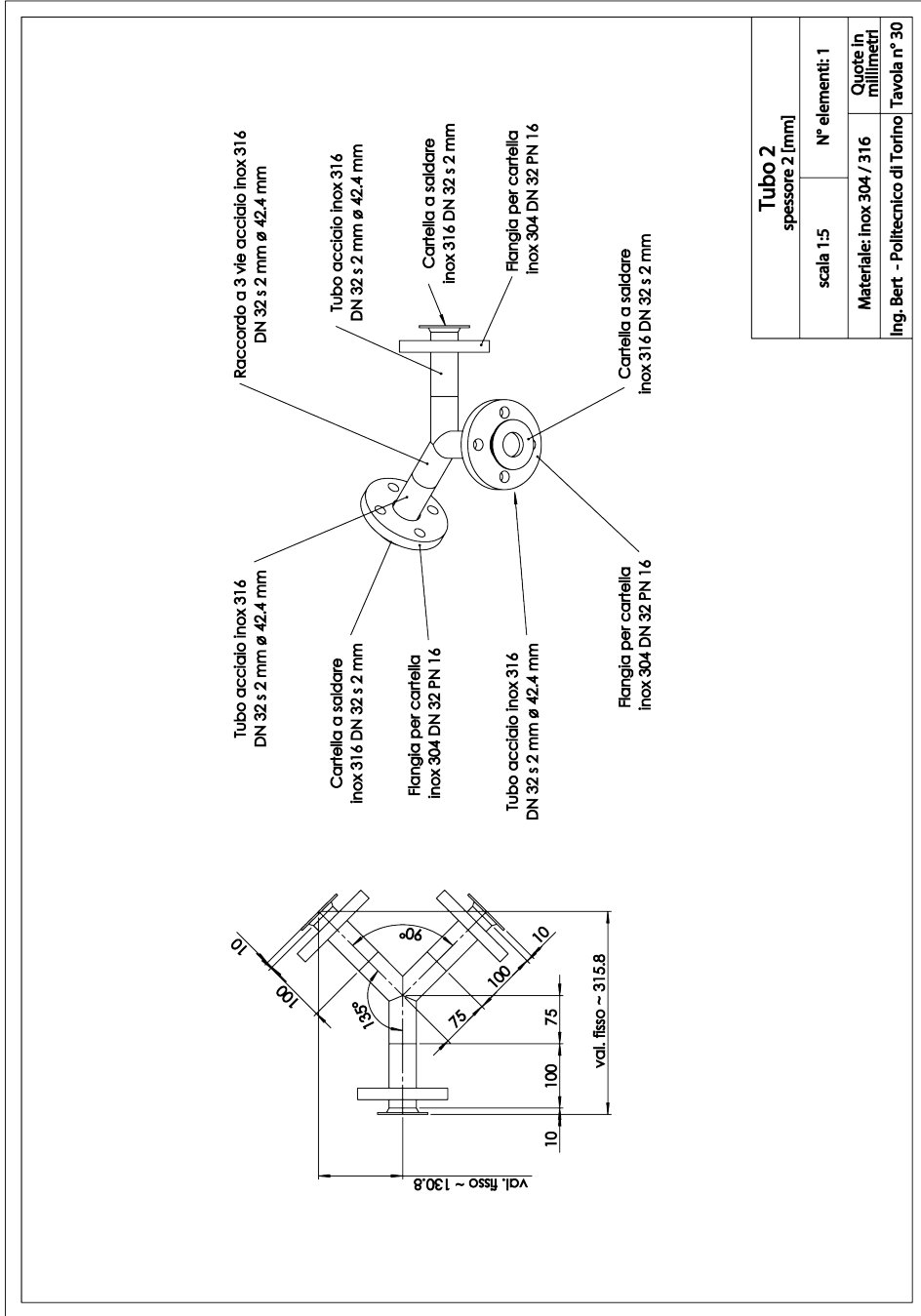


Fig. B.30 Pipe 2 of the main line DN 32.

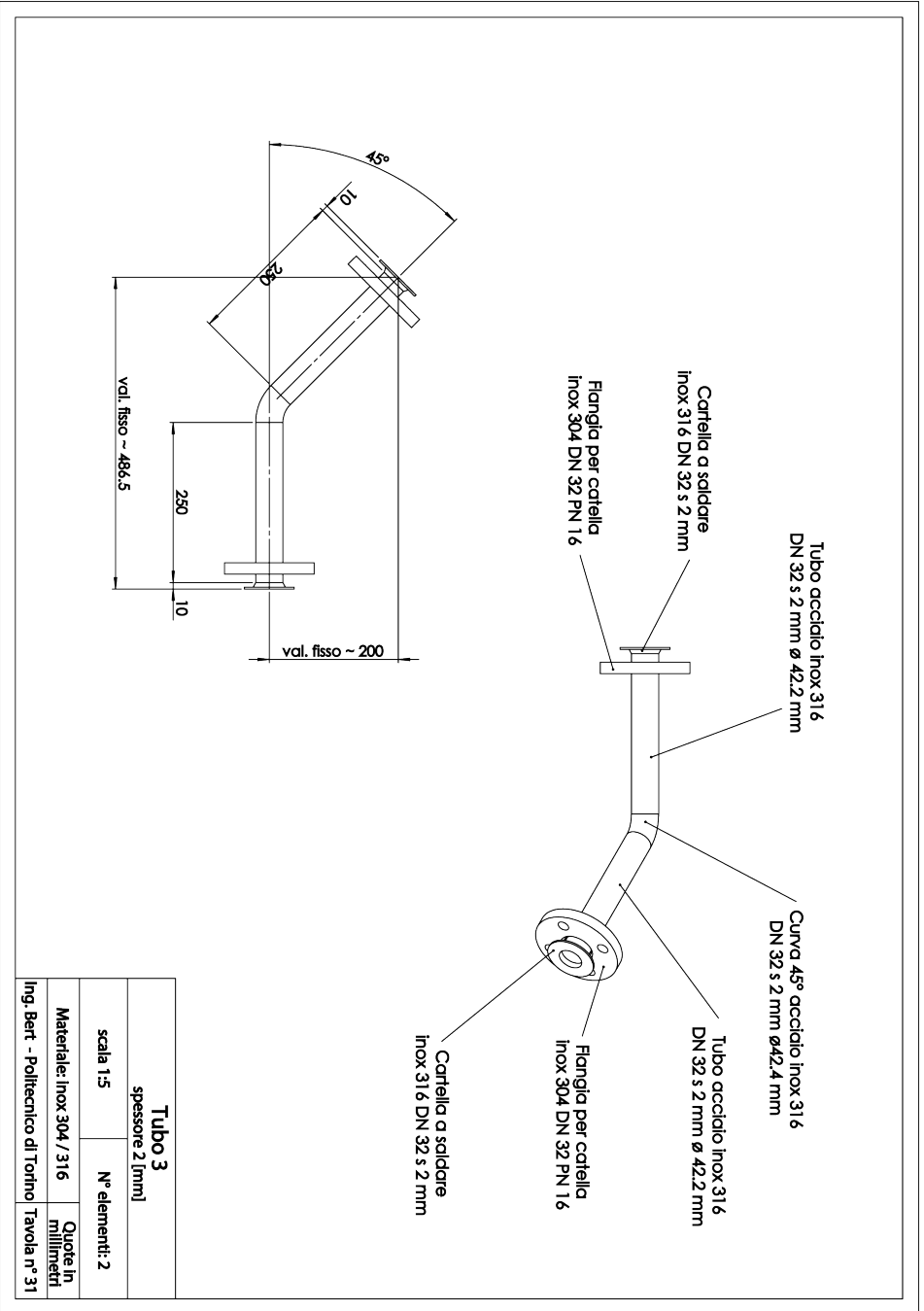


Fig. B.31 Pipe 3 of the main line DN 32.

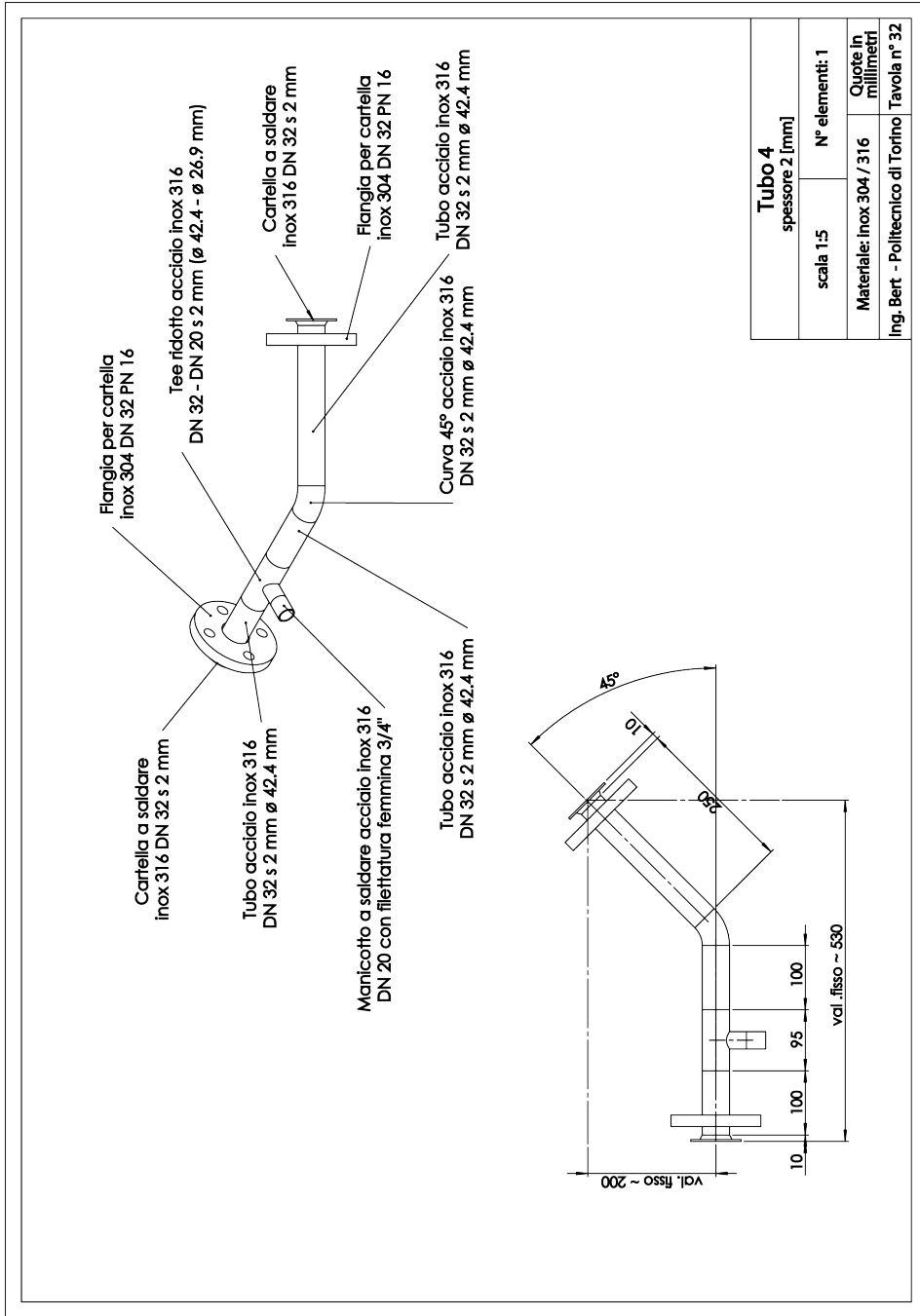


Fig. B.32 Pipe 4 of the main line DN 32.

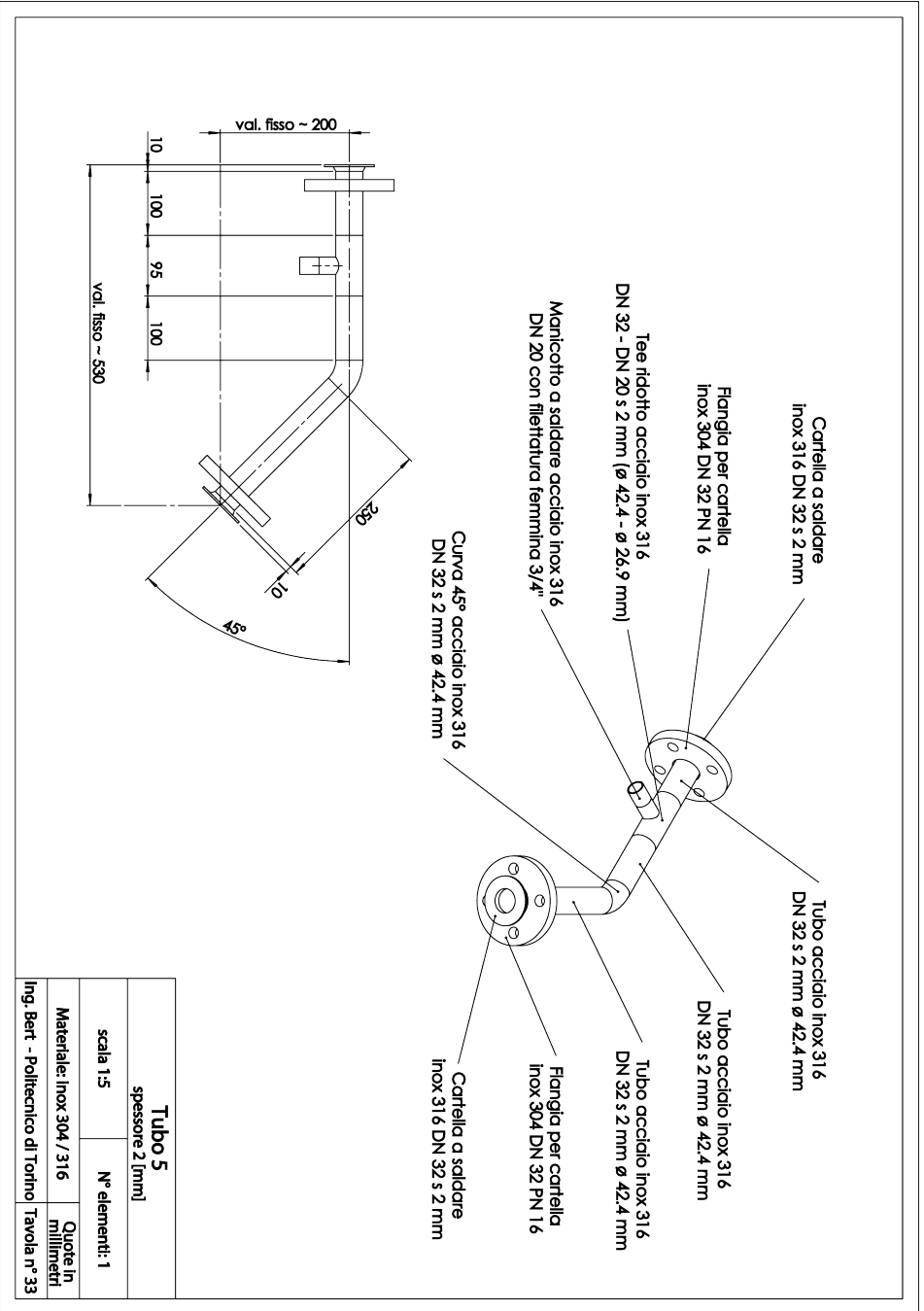


Fig. B.33 Pipe 5 of the main line DN 32.

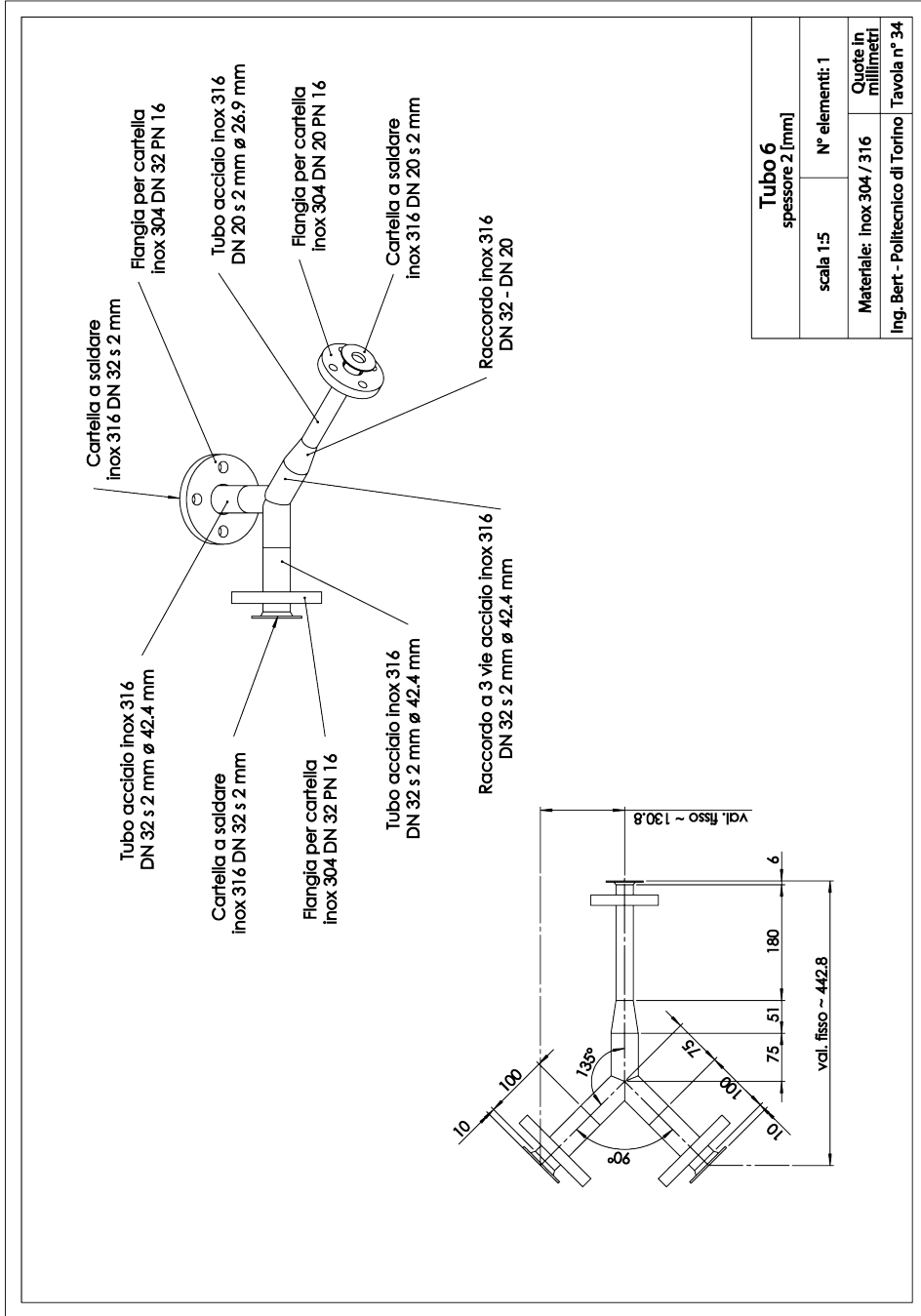


Fig. B.34 Pipe 6 of the main line DN 32 to DN 25.

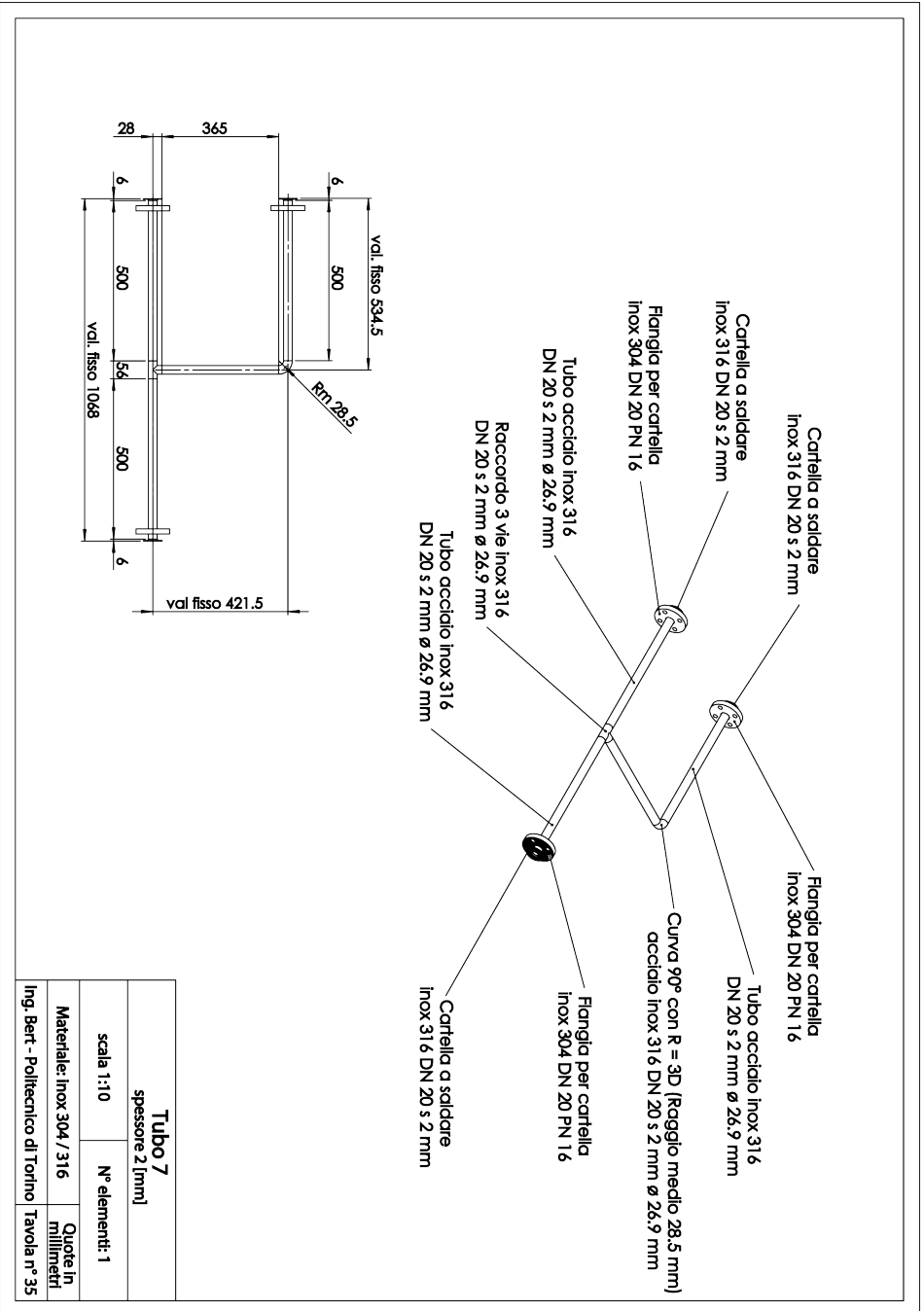


Fig. B.35 Pipe 7 of the main line and by-pass line DN 25.

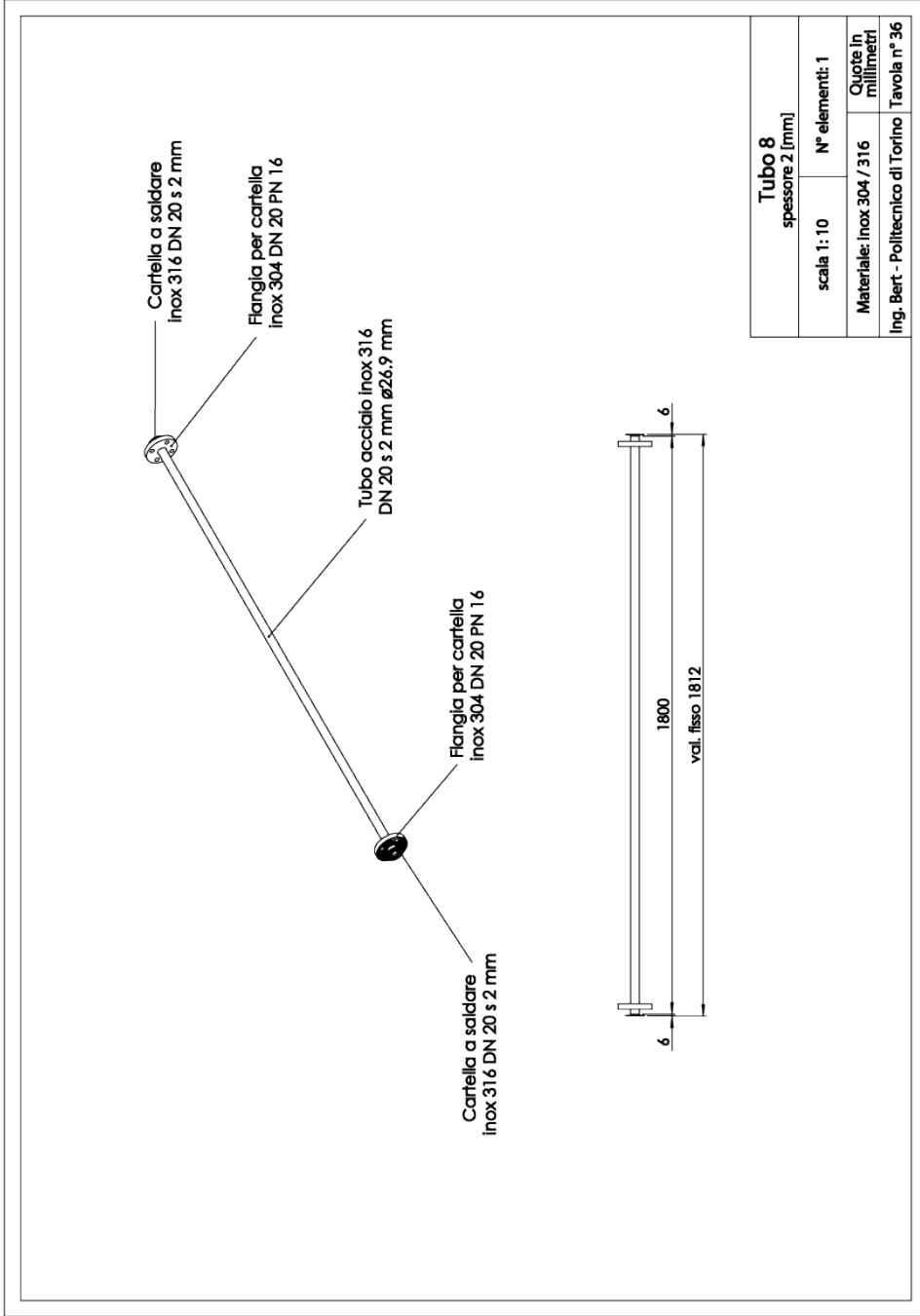


Fig. B.36 Pipe 8 of the main line DN 25.

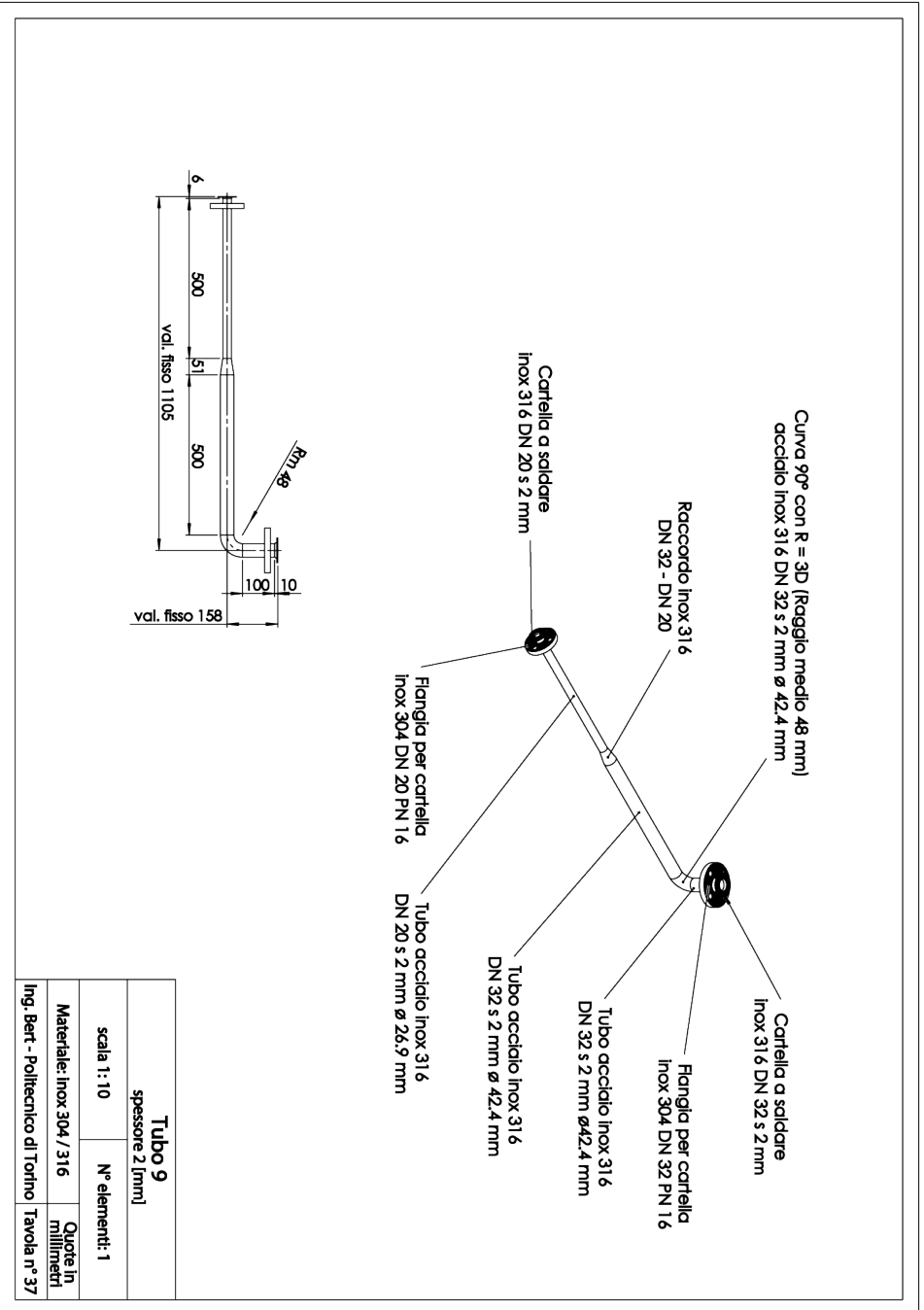


Fig. B.37 Pipe 9 of the main line DN 25 to DN 32.

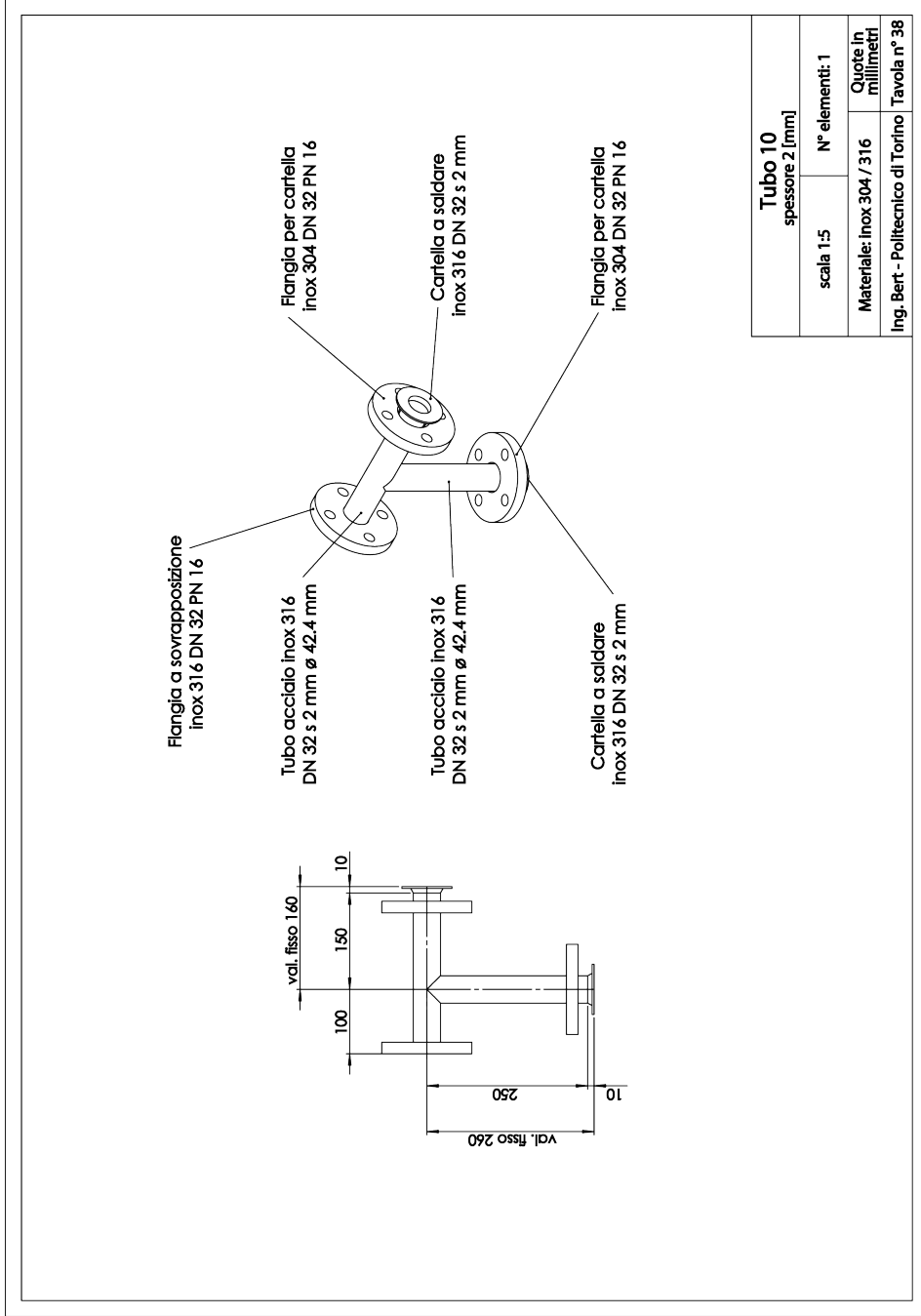


Fig. B.38 Pipe 10 of the main line DN 32.

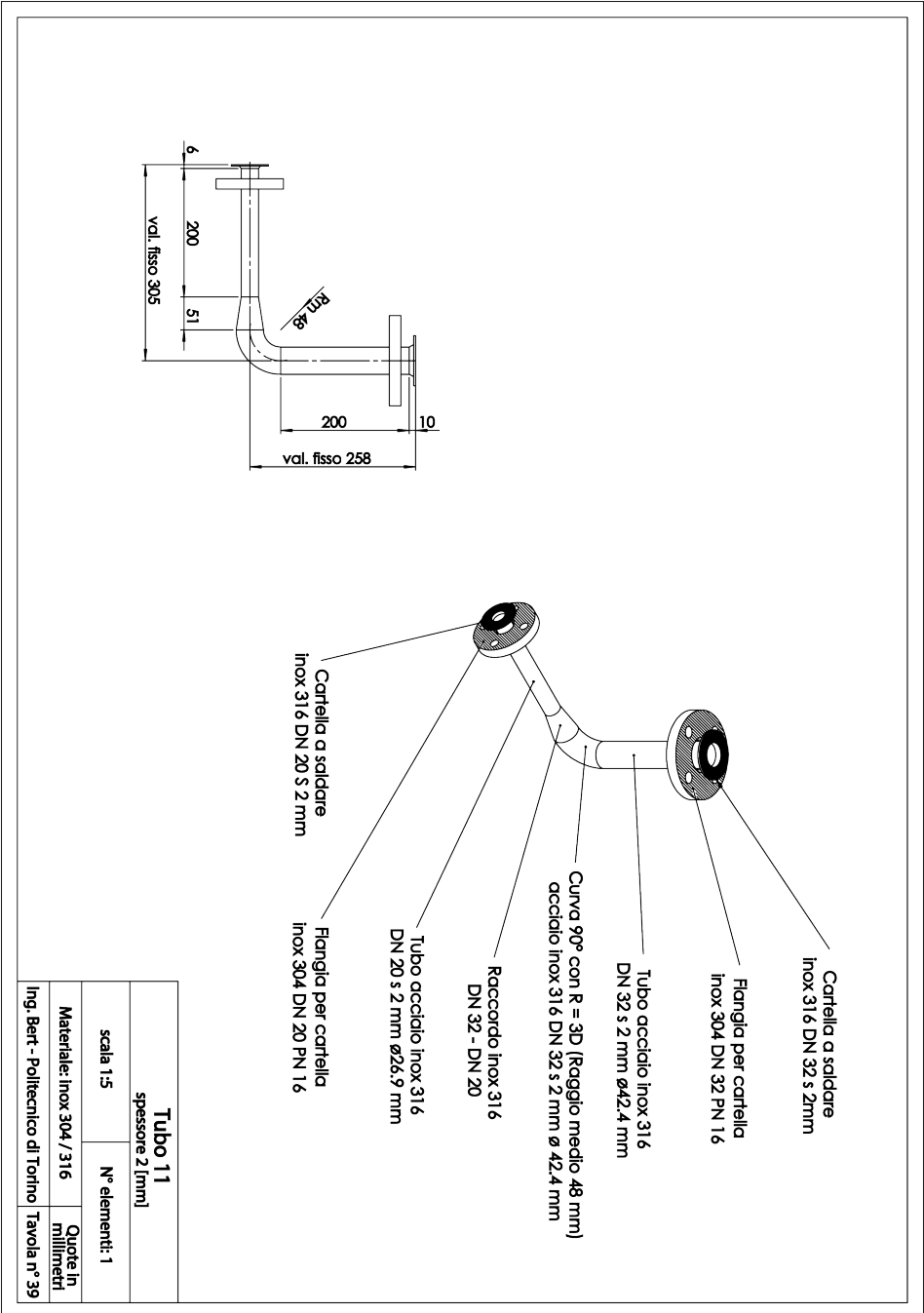


Fig. B.39 Pipe 11 of the main line DN 32.

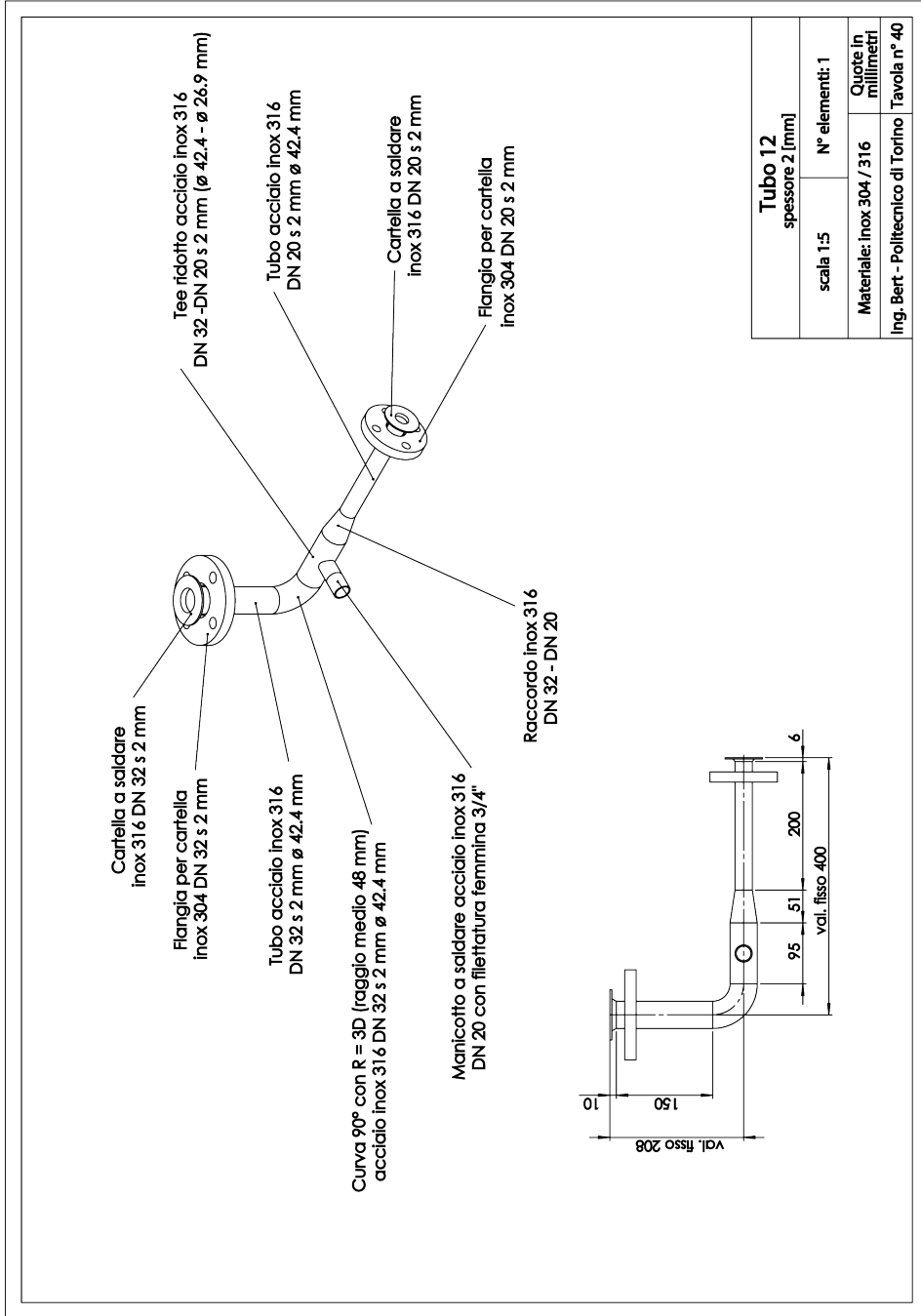


Fig. B.40 Pipe 12 of the main line DN 32.

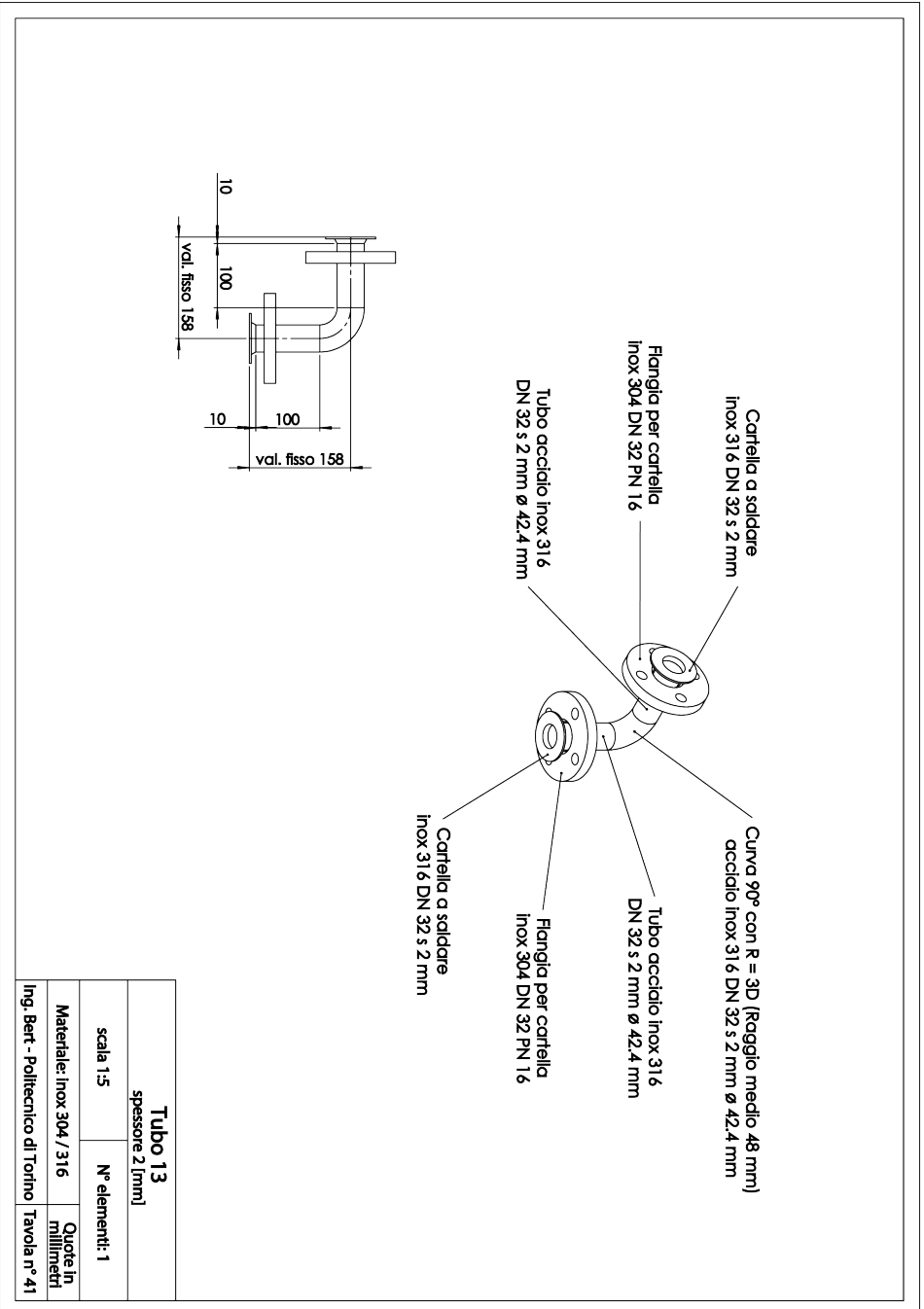


Fig. B.41 Pipe 13 of the main line DN 32.

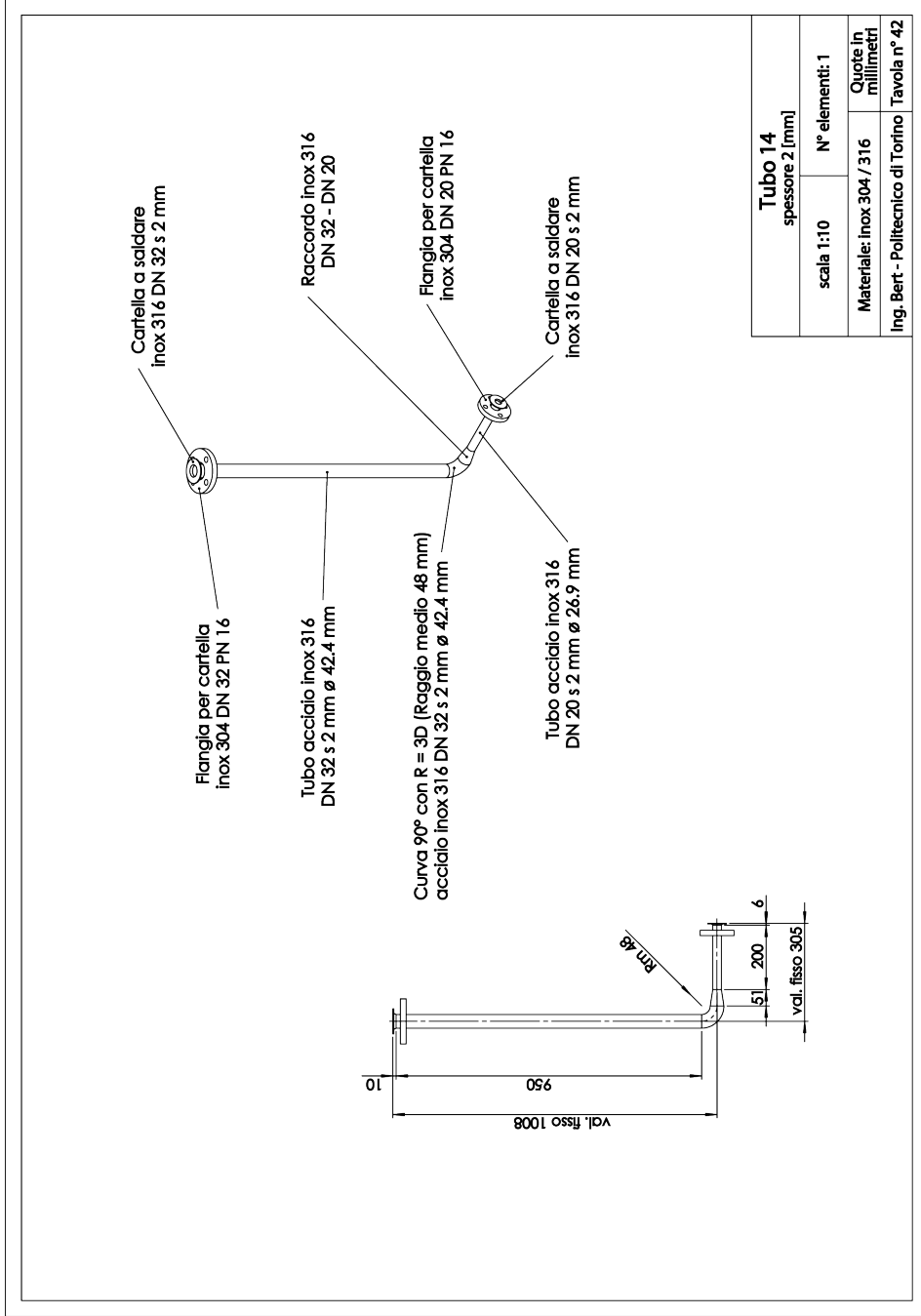


Fig. B.42 Pipe 1 of the by-pass line DN 25 to DN 32.

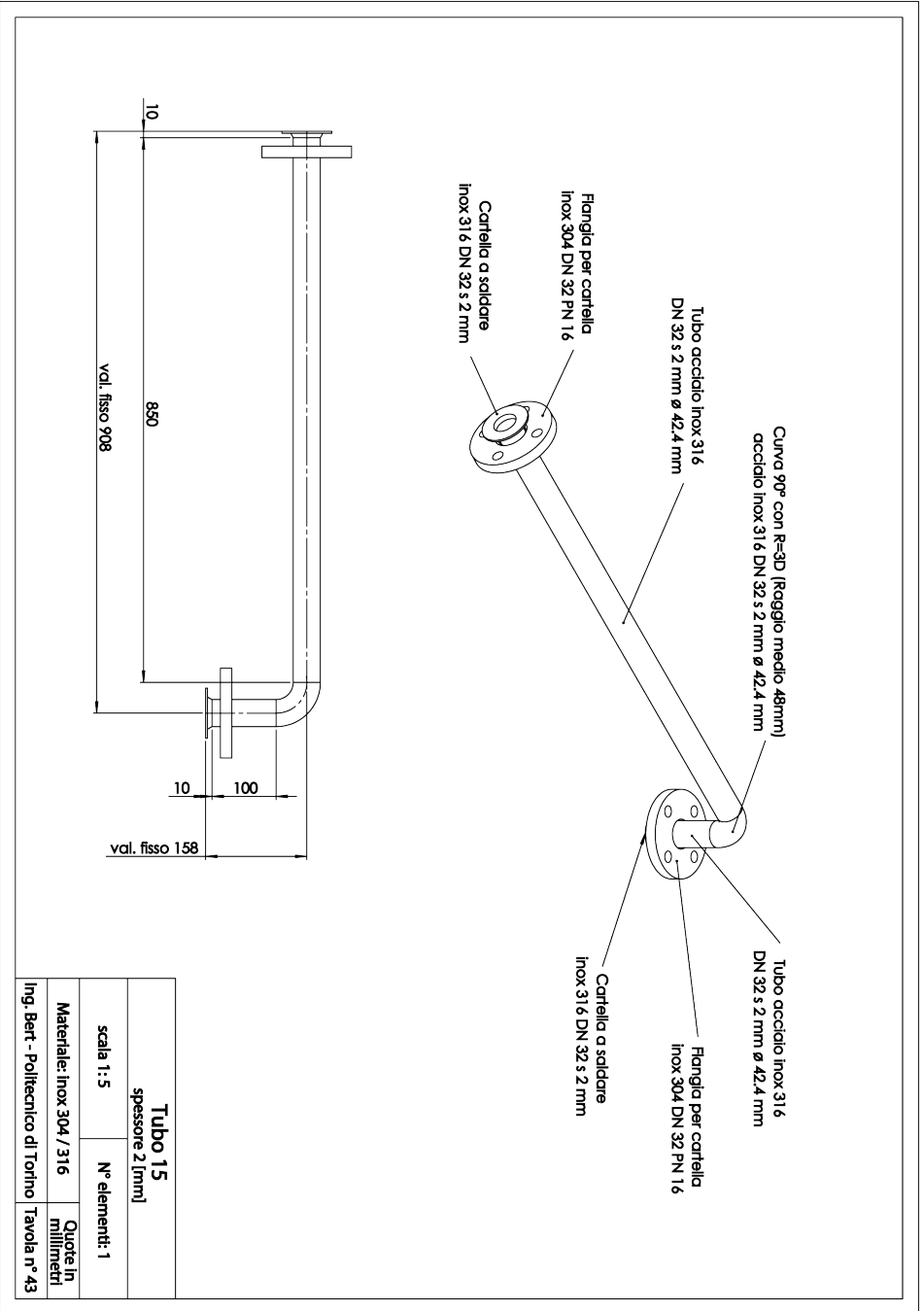


Fig. B.43 Pipe 2 of the by-pass line DN 32.

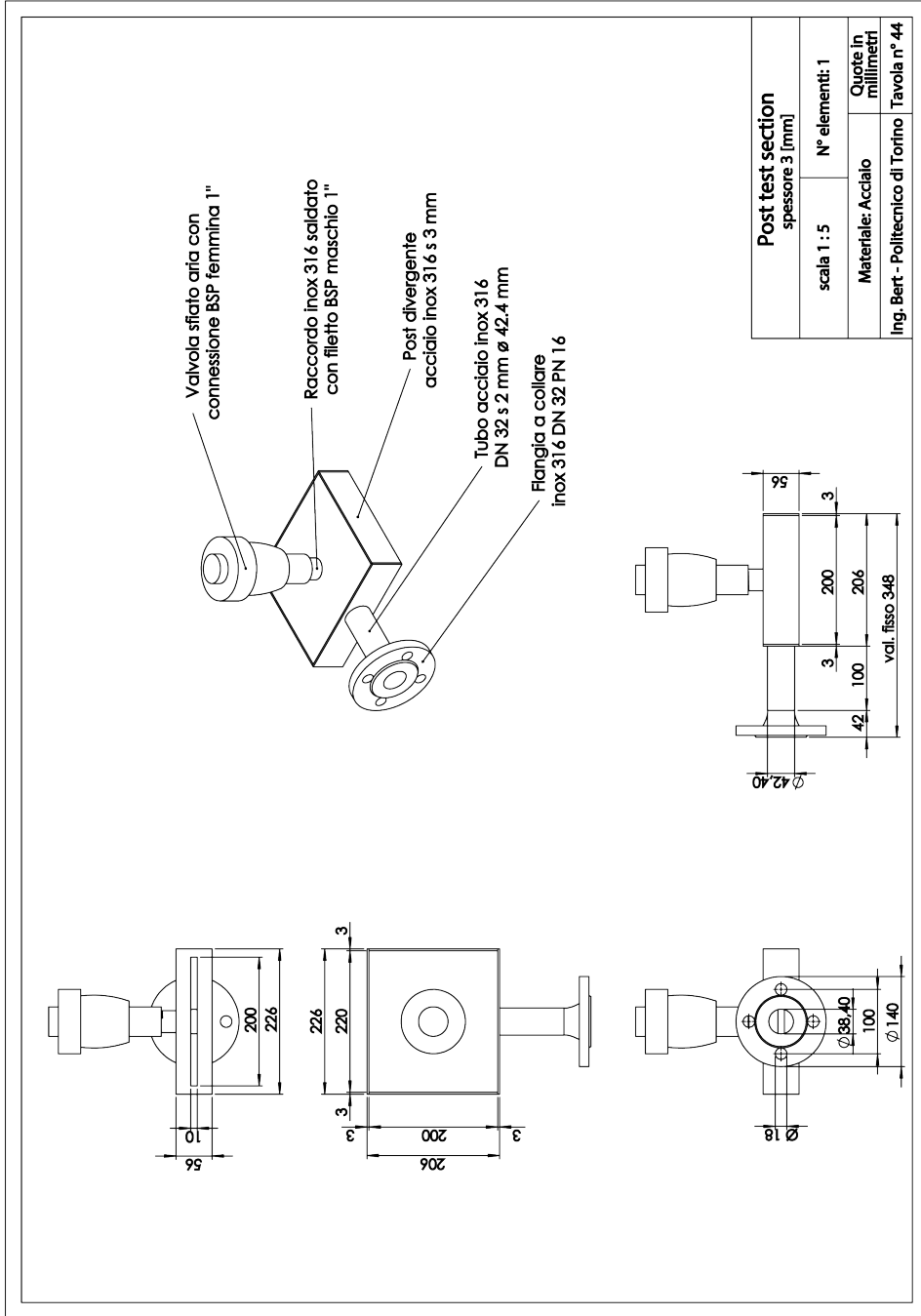


Fig. B.44 Post test section.

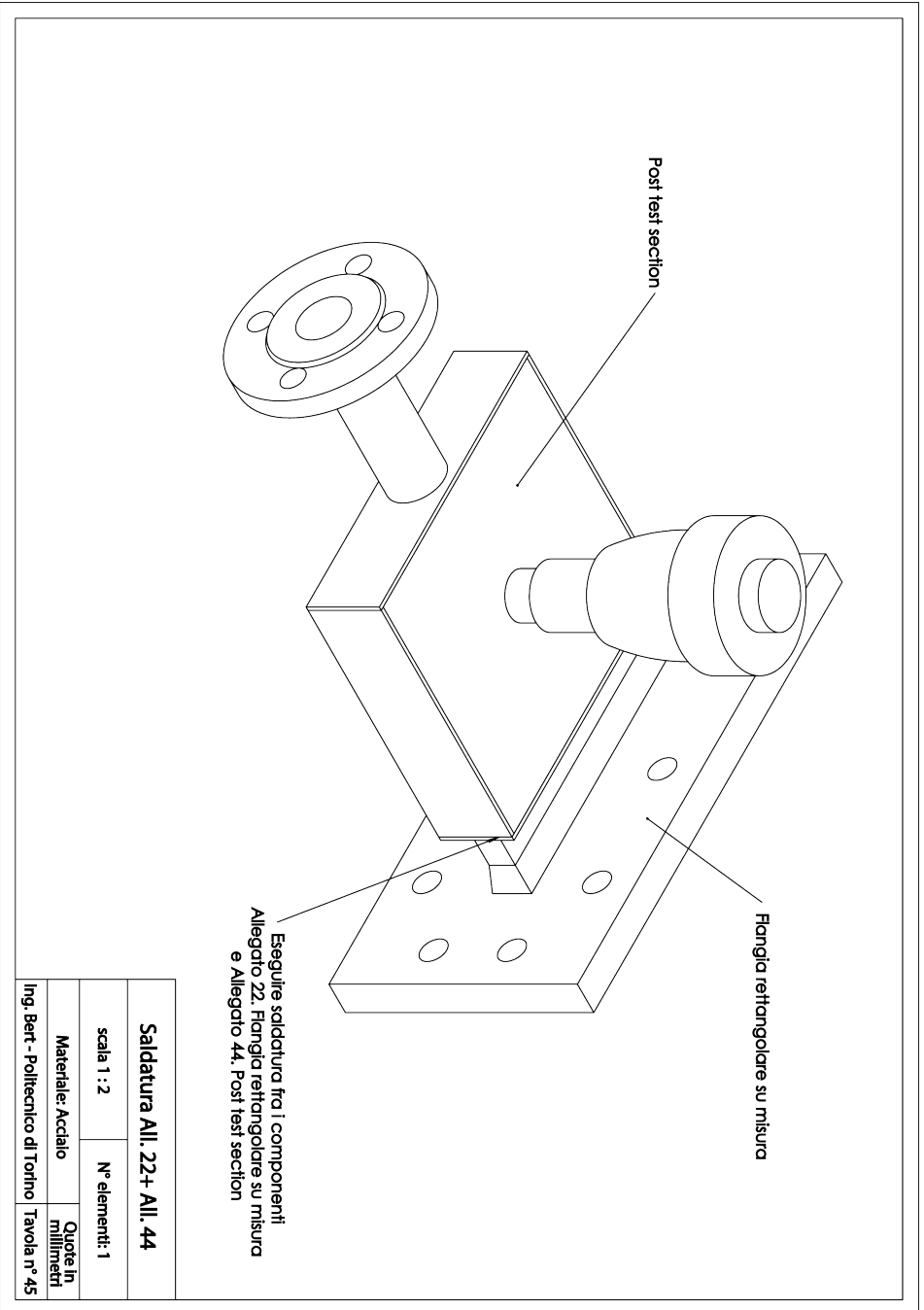
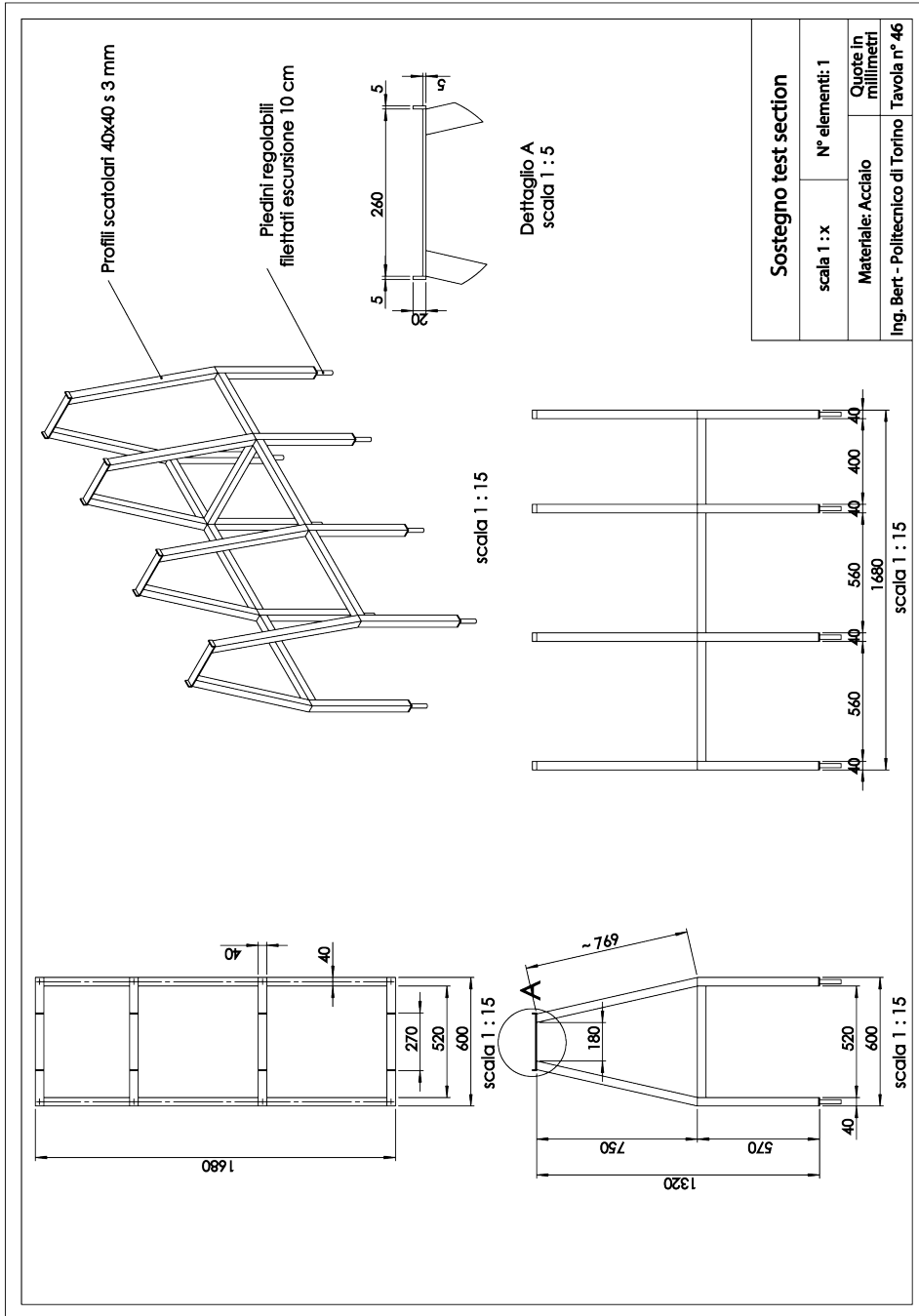


Fig. B.45 Welding of the post test section.



caption Supports of the test section.

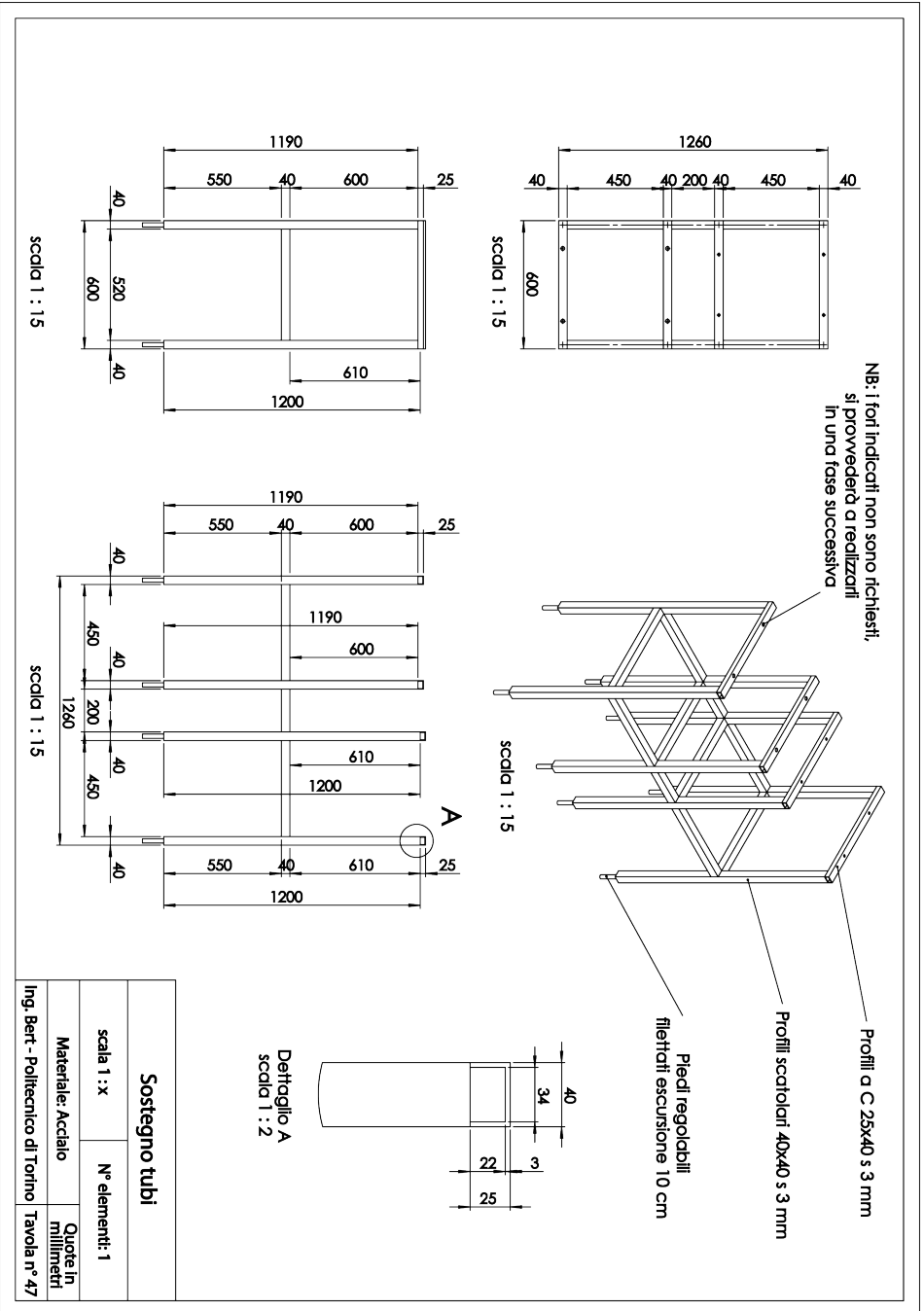


Fig. B.46 Supports of the main flow-dynamic convergent, Straight pipe DN 250 and DN 250 tube with 90° bend.

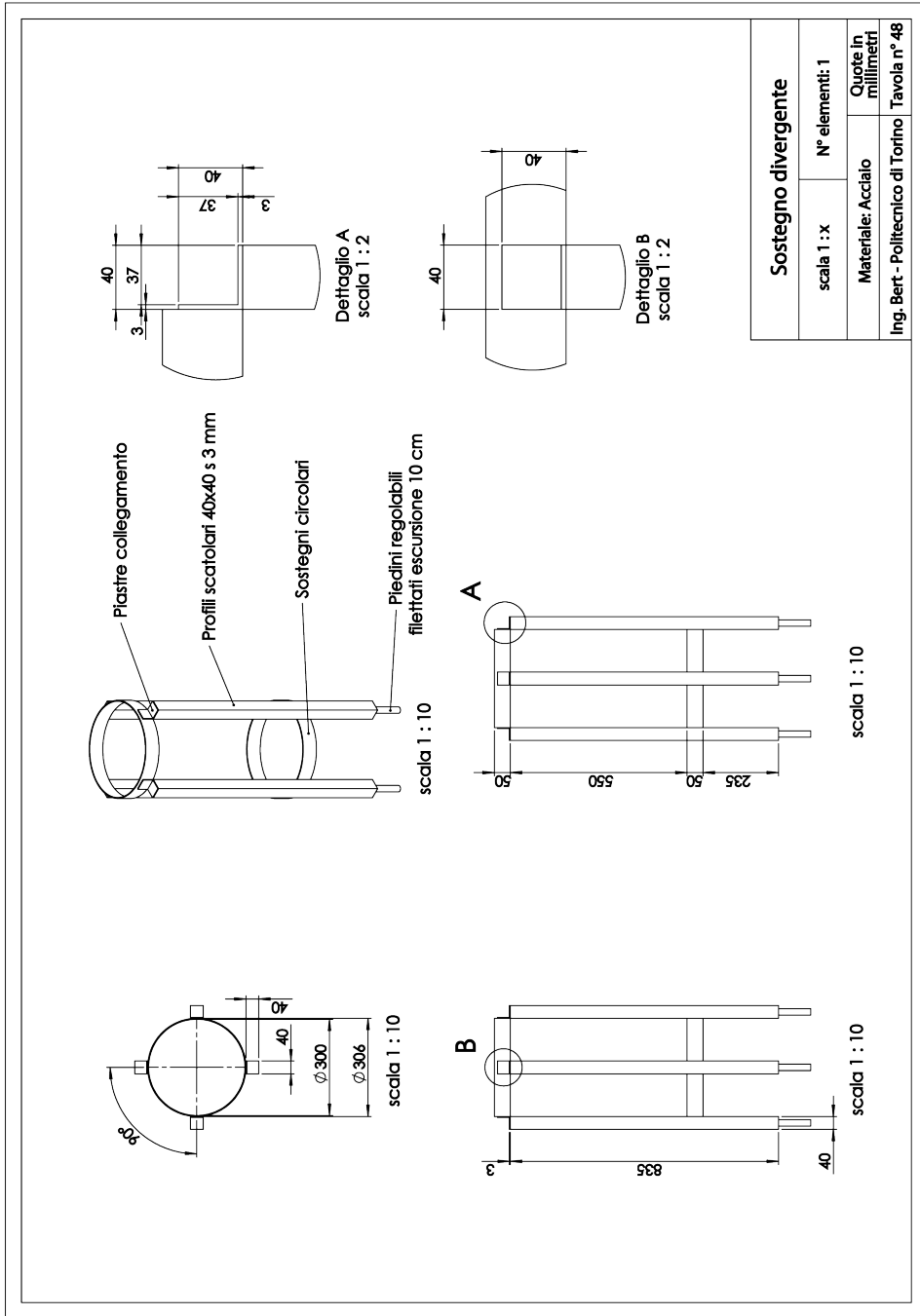


Fig. B.47 Supports of the hand made divergent

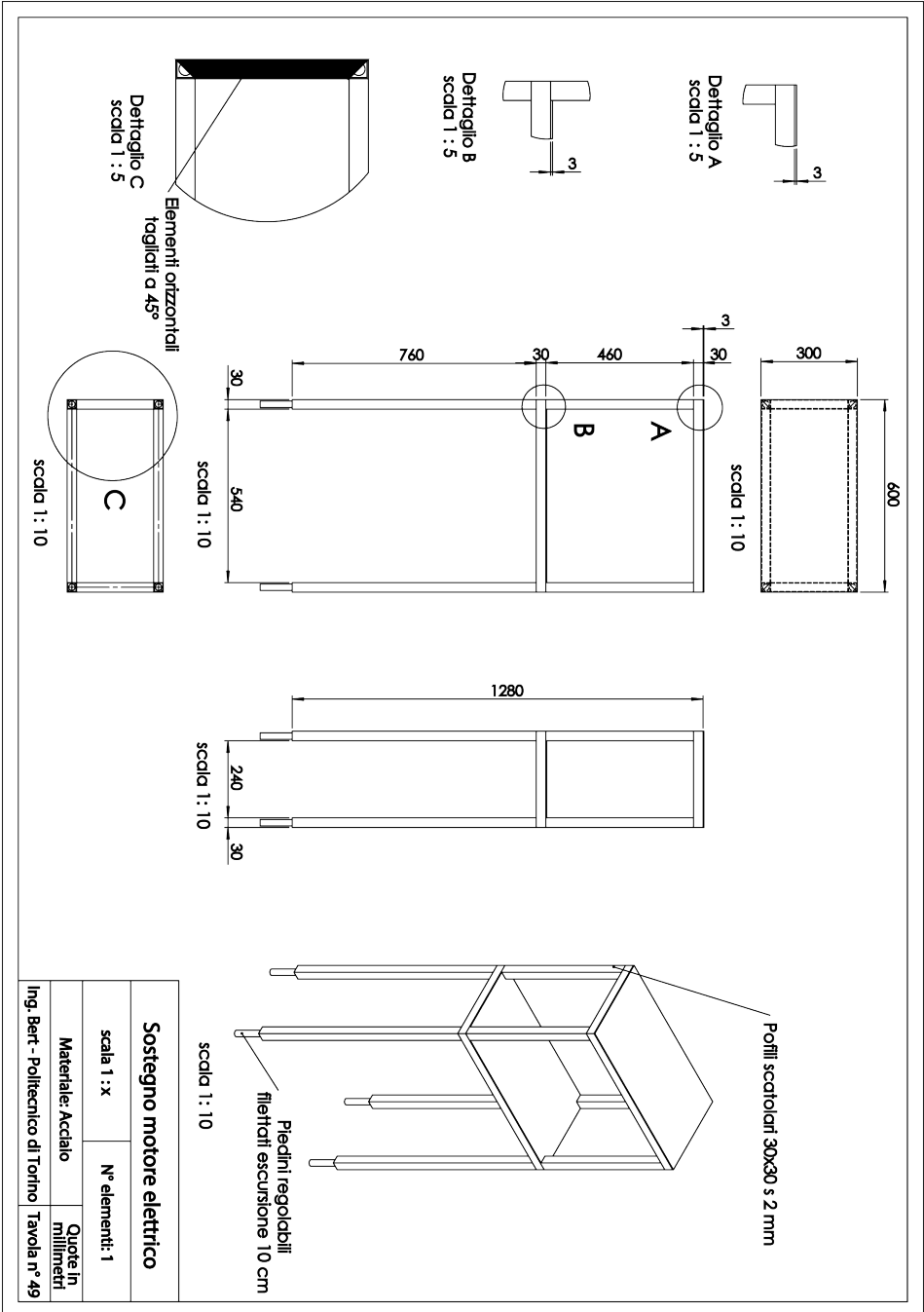


Fig. B.48 Supports of the electric engine